

POLITECNICO DI TORINO

SCUOLA INTERPOLITECNICA DI DOTTORATO

Doctoral Program in Biomedical Engineering

Final Dissertation

**IRON OXIDE NANOCONSTRUCTS FOR THE ABLATION
THERAPY IN DISEASED TISSUES: SYSTEMIC
ANALYSIS AND RATIONAL DESIGN**



Antonio Cervadoro

Tutors
Prof. Paolo Decuzzi
Prof. Gianluca Ciardelli

Co-ordinator of the Research Doctorate Course
Prof. Cristina Bignardi

February 27th, 2014

© COPYRIGHT

by

Antonio Cervadoro

2014

ALL RIGHTS RESERVED

**IRON OXIDE NANOCONSTRUCTS FOR THE ABLATION
THERAPY IN DISEASED TISSUES: SYSTEMIC
ANALYSIS AND RATIONAL DESIGN**

Antonio Cervadoro

Doctoral Program in Biomedicine Engineering

SCUOLA INTERPOLITECNICA DI DOTTORATO

Area Ingegneria Biomedica e Biomeccanica (BEE)

Tutors:

Prof. Paolo Decuzzi,
Houston Methodist Research Institute, Houston, Texas

Prof. Gianluca Ciardelli,
Politecnico di Torino, Turin, Italy

Referees:

Prof. Florence Gazeau,
Université Paris Diderot, Paris, France

Prof. Audrius Brazdeikis,
University of Houston, Houston, Texas

ACKNOWLEDGMENTS

Scrivere i ringraziamenti è doveroso.

Perchè alla fine di un periodo così lungo, di cui appena ricordi l'inizio, dopo tanta fatica, ma anche divertimento, soprattutto passione, ti vedi diverso. E non è certo solo merito tuo.

Perchè quando arrivi alla fine di un percorso sei così preso dal traguardo da dimenticare il percorso stesso; ed allora scrivere queste due righe ti costringe a guardare indietro per renderti conto di quale e quanta strada hai fatto.

Perchè mentre questa pila di carta rimarrà a prender polvere in uno scantinato insieme a migliaia di altre, prendere il tempo di scrivere questi sentimenti li farà affiorare e fissare nella mente e nel cuore, dove ha senso stiano.

Una lista di nomi sarebbe tanto infinita quanto incompleta, vista e considerata la mia pessima memoria. Per cui cercherò di farli tutti, senza farne nessuno.

Il primo pensiero va ovviamente ai miei genitori, primi “responsabili” di tutto questo; se dovete lamentarvi con qualcuno, fatelo con loro. Quindi mia sorella e mio fratello, e tutta la mia famiglia. E bada bene intendo sia quella che, per fortuna, mi è capitata, sia quella che mi son scelto nel tempo, ovvero i buoni vecchi amici. Tutti da sempre fonte di supporto infinito ed incondizionato. Supporto e rimprovero, che poi ci vuole anche quello per potersi migliorare. Una menzione particolare a mio nonno, che non ha mai lasciato il mio fianco, ed a due cugini lontani, esempio di come è possibile far grandi cose senza prendersi troppo sul serio, e godendosi la vita.

Se son riuscito a completare questo percorso è merito però di chi mi ha fatto da mentore; soprattutto di chi in questi ultimi anni ha avuto l'incredibile pazienza di guidarmi, insegnarmi e sopportarmi. Condividendo spontaneamente con me conoscenza, visione e passione, mi ha costantemente illuminato la via.

Invece, la forza di andare avanti anno dopo anno è derivata da tutti gli amici che ho trovato in terra straniera. Chi fin dall'inizio mi ha accolto ed accettato; chi mi ha fatto entrare nella sua vita e l'ha condivisa ogni giorno; chi ha condiviso con me le follie del laboratorio; chi ha voluto condividere con me i suoi modi di vivere e la sua cultura, così differente dalla mia. Solo grazie a voi mi son sentito a casa; solo grazie a voi ne è valsa pena.

E ringrazio anche chi non ha creduto in me, chi non se l'aspettava, chi non me l'augurava. E' grazie a loro che ho potuto vedere chiaramente la differenza.

Ma a dirla tutta, forse quello che sento non è il bisogno di dire un semplice grazie. No, questo non è per ringraziarvi di quello che è stato fin'ora; piuttosto è per dedicarvi quello che sono diventato ora, e tutto quello che farò d'ora in poi. Non ho altro modo, in fondo, per ritornare tutto quello che da voi ho ricevuto.

TABLE OF CONTENTS

Table of Contents	ix
List of Illustrations.....	xi
List of tables	xii
1. INTRODUCTION.....	1
1.1. Nanomedicine and thermal therapies	1
<i>1.1.1. Outline.....</i>	<i>8</i>
2. THEORETICAL MODEL OF HEAT GENERATION AND TRANSPORT	9
2.1. Magnetic loss power in radiofrequency regime	10
<i>2.1.1. Magnetic equilibrium susceptibility.....</i>	<i>12</i>
<i>2.1.2. Neel and Brown relaxation times.....</i>	<i>13</i>
2.2. Heat transport modeling	16
<i>2.2.1. Application of first law of thermodynamics.....</i>	<i>16</i>
<i>2.2.2. Heat transport and sample tube geometry</i>	<i>18</i>
<i>2.2.3. Determining the temperature-time relationship.....</i>	<i>21</i>
2.3. Definition of specific absorption rate	25
<i>2.3.1. SAR_f and SAR_{NP}</i>	<i>25</i>
2.4. Finite element modeling of the temperature field.....	27
2.5. Discussion on SAR limitation as evaluating parameter	32
3. DESIGN MAPS FOR LOCAL HYPERTHERMIA AND ABLATION THERAPY...43	
3.1. SPIOs: characterization and processing.....	45
3.2. Apparata for magnetic hyperthermia and ablation therapy	51
<i>3.2.1. High frequency field apparatus (>10 MHz)</i>	<i>51</i>
<i>3.2.2. Low frequency field apparatus (≤ 1 MHz).....</i>	<i>54</i>

3.2.3.	<i>High power system apparatus (≤ 1 MHz and up to 40 kA m^{-1})</i>	56
3.2.4.	<i>Homogeneity of the magnetic field</i>	58
3.3.	Results	60
3.3.1.	<i>SAR experimental setup</i>	60
3.3.2.	<i>Correct computing of the specific absorption rate</i>	60
3.3.3.	<i>Hyperthermic performance at high frequency field</i>	64
3.3.4.	<i>Non-specific heating at high frequency field</i>	66
3.3.5.	<i>Hyperthermic performance at low frequency field</i>	73
3.3.6.	<i>Computational modeling of the temperature field within the tissue</i>	76
3.4.	Discussion on the clinical feasibility of thermal therapies	83
4.	A NOVEL CLASS OF MAGNETIC NANOCONSTRUCTS	87
4.1.	Synthesis, physico-chemical characterization, and cell viability assessment of polymeric nanoconstructs	89
4.1.1.	<i>Particles synthesis</i>	89
4.1.2.	<i>Chemico-physical characterization</i>	101
4.1.3.	<i>Cell Culture</i>	101
4.1.4.	<i>Results</i>	109
4.2.	Magnetic dragging	117
4.2.1.	<i>Microfluidic experiments</i>	117
4.2.2.	<i>Results</i>	124
4.3.	Relaxometric properties	132
4.3.1.	<i>Relaxivity characterization</i>	132
4.3.2.	<i>Results</i>	132
4.4.	Thermal ablation properties: in-vitro and preliminary in-vivo experiments	135

4.4.1. <i>Animal studies</i>	135
4.4.2. <i>In-vitro characterization</i>	136
4.4.3. <i>Preliminary in-vivo test on small animal</i>	139
4.5. Comparison with conventional SPIOs and iron oxide nanocubes.....	144
5. CONCLUSIONS AND FUTURE WORKS	151
6. REFERENCES.....	157

LIST OF ILLUSTRATIONS

<i>Figure 1-1. Nanodevice for cancer treatment</i>	3
<i>Figure 2-1. Néel and Brown relaxation modes</i>	15
<i>Figure 2-2. Modeling of heat transport through a vial</i>	19
<i>Figure 2-3. Graphical representation of the terms A and B in Equation (2-31)</i>	24
<i>Figure 2-4. Domain of interest for the modeling of temperature field</i>	28
<i>Figure 2-5. Sensitivity analysis of the imaginary susceptibility χ''</i>	34
<i>Figure 2-6. Comparison Specific Absorption Rate (SAR) vs. corresponding Intrinsic Loss Power (ILP)</i>	38
<i>Figure 2-7. ILP dependence on saturation magnetization M_s and anisotropy constant K for $f = 500$ kHz, $H_0 = 10$ kA m⁻¹</i>	41
<i>Figure 3-1. Physico characterization of the SPIO formulations</i>	48
<i>Figure 3-2. SQUID measurements of 5, 10, and 14 nm Iron Oxides (IOs)</i>	50
<i>Figure 3-3. High frequency apparatus</i>	53
<i>Figure 3-4. Low frequency apparatus</i>	55
<i>Figure 3-5. High power apparatus</i>	57
<i>Figure 3-6. Homogeneity verification of the deployed field</i>	59
<i>Figure 3-7. Comparisons between computational SAR methods</i>	63
<i>Figure 3-8. Hyperthermic performance at high frequency field (30 MHz)</i>	65
<i>Figure 3-9. Non-specific heating at high frequency field (30 MHz)</i>	68
<i>Figure 3-10. Comparison of non-specific heating at high frequency field</i>	70
<i>Figure 3-11. Mild heating of SPIOs at high frequency field (30 MHz)</i>	72
<i>Figure 3-12. Hyperthermic performance at low frequency fields (0.2; 0.5; and 1 MHz)</i>	75
<i>Figure 3-13. Computational modeling of the temperature field within a biological tissue</i>	78

<i>Figure 3-14. Temperature increase in the modelled areas.</i>	78
<i>Figure 3-15. Design map for local hyperthermia and ablation therapy.</i>	82
<i>Figure 4-1. TEM Iron Oxides nanoparticles.</i>	92
<i>Figure 4-2. Synthesis steps in Hybrid NanoParticles (HNPs).</i>	94
<i>Figure 4-3. Discoidal Polymeric Nanoconstructs (DPNs) synthesis.</i>	97
<i>Figure 4-4. Deoxy-chitosan conjugation.</i>	99
<i>Figure 4-5. Emulsion procedure for Magnetic NanoFlakes (MNFs).</i>	100
<i>Figure 4-6. Cultured cells in adhesion.</i>	103
<i>Figure 4-7. Cells harvesting process</i>	105
<i>Figure 4-8. Cell counting.</i>	107
<i>Figure 4-9 Hybrids NanoParticles (HNPs) and Discoidal Polymeric Nanoconstructs (DPNs) structure.</i>	109
<i>Figure 4-10. Physical characterization of DPNs.</i>	111
<i>Figure 4-11. Physico-chemical properties of Magnetic NanoFlakes (MNFs).</i>	114
<i>Figure 4-12. Cytotoxicity of MNFs.</i>	116
<i>Figure 4-13. Microfluidic apparatus</i>	119
<i>Figure 4-14. Magnets used for dragging experiments.</i>	120
<i>Figure 4-15. Flow chamber channel with magnet position.</i>	122
<i>Figure 4-16. Imaging process of the flow chamber aggregates.</i>	123
<i>Figure 4-17. Dragging of J-774 macrophages loaded with Hybrids NanoParticles (HNPs) + 17 nm IOs.</i>	125
<i>Figure 4-18. In flow accumulation experiments</i>	127
<i>Figure 4-19. Remote guidance of the Magnetic NanoFlakes (MNFs)</i>	129
<i>Figure 4-20. Accumulation of MNFs at the bottom of the flow chamber during flow in physiological condition.</i>	131
<i>Figure 4-21. Relaxometry performance of free Iron Oxides (IOs) free and loaded inside Discoidal Polymeric Nanoconstructs, and Magnetic NanoFlakes (MNFs).</i>	134
<i>Figure 4-22. Magnetic properties of the Magnetic NanoFlakes (MNFs).</i>	138
<i>Figure 4-23. Tumor exposure to magnetic field.</i>	141
<i>Figure 4-24. Tumor size during preliminary hyperthermia treatment with MNFs.</i>	143
<i>Figure 4-25. Polymeric particles performances compared to literature.</i>	148

LIST OF TABLES

<i>Table 2-1. Parameters used in finite element simulations.</i>	31
<i>Table 2-2. Published SAR and calculated equivalent ILP.</i>	36



1. Introduction

1.1. Nanomedicine and thermal therapies

In 1959, with his famous talk “There’s plenty of room at the bottom” [1], Richard Feynman officially introduced the world to an upcoming scientific revolution. His prospective, on the possibility for man to manipulate matter at its basilar elements, or single atoms, was later named “Nanotechnology” by Norio Taniguchi in 1974 [2]. This name inspired countless investigations amongst scientists and unbound intrigue by novelists. Finally, they were the ’80s to see Nanotechnology emerged as a proper scientific field: in 1981 the invention of the Scanning Tunneling Microscope (for which Gerd Binnig and Heinrich Rohrer were awarded the Nobel Prize in Physics, 1986) allowed first-time visualization of single atoms; in 1985 Smalley and coworker “build” the first molecular compound not available in nature (C_{60} , the Fullerene and were awarded with the Nobel Prize in Chemistry, in 1996) [3]. In 1986 with his book “Engines of Creation” [4], Drexler provoked the imaginations of many, foreseeing the time when nanoscaled “assemblers” will be able to handle single atoms and build items of similar size. Since then, with 30 years of research and development, nanotechnology infiltrates almost every field of science and industry; from biology to building science, from electronic and environment control [5-8], and brings new promises and pushes the boundaries in each field. Still, due to its innate complexity and distance from everyday experience, the pervasive feeling is that we are just scratching on the surface.

Medicine is one of the most emblematic fields in which nanotechnology presents greatest opportunity but also vexing with difficulties. Human body is a perfect interacting system of cells, organelles, enzymes, proteins, nucleic acids and molecular signaling. On the other hand, nanomaterials are widely studied in biology because they are similar in composition (i.e. chemical, physical, structural, and topographical properties) to molecules and building blocks of many biological systems [9]. From these considerations, Nanomedicine represents a tool to interact with single components of our body [10]. The upcoming possibilities are probably matched only by the complexity of such a goal. Nowadays, the word Nanomedicine refers to application of nanoplateforms for specific roles, as drug delivery (with special regards to tumor sites) [11, 12], tissues regeneration [13], molecular detection and imaging diagnosis [14, 15], and direct treatment of illness [16-18]. Peculiarity of this field is the demand for a multi-disciplinary approach, regardless of the specific application of nanostructured devices.

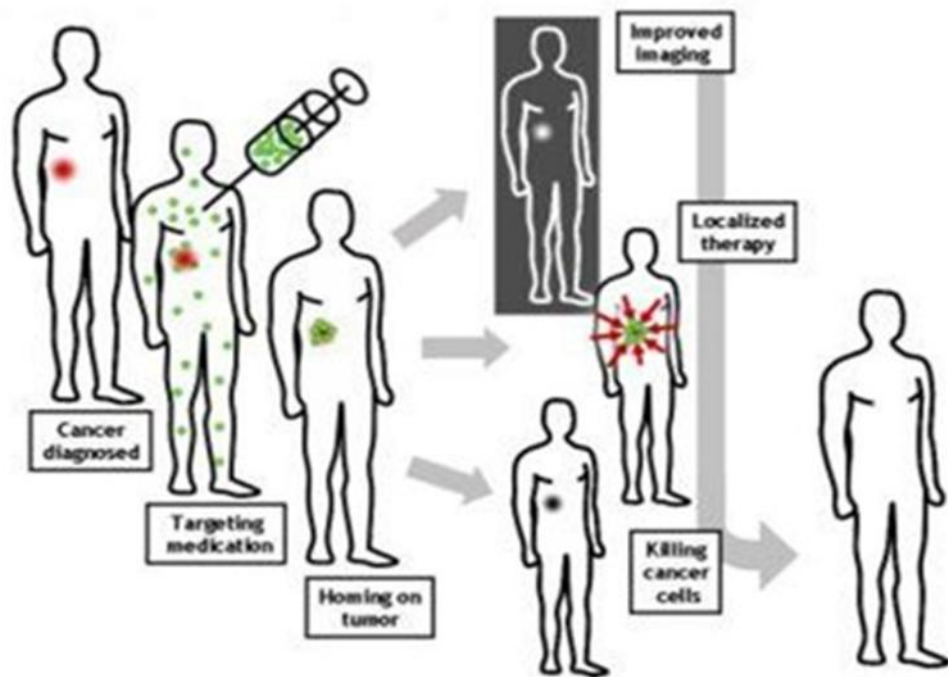


Figure 1-1. Nanodevice for cancer treatment.

An ideal nanodevice designed for the cure of cancer should be able to perform in two phases: (i) recognize and selectively target the region of interest region(s); (ii) locally deploy one or more functions finalized to the cancer treatment. (Source: S.M. Sonal, V. Prabhakar, T. Aneesh, M. Sabitha; *Int. J. Nanotech.* 2008 Vol. 2 Num. 2)

Hyperthermic treatments for malignant tissues

The use of heat to treat various ailments, and cancer in particular, has roots that run deep in the history of medicine [19]. First documented practices go back to the ancient Egyptians, over four thousand years ago; at that time, it was common practice to apply hot oil or cautery to tumors [20]. Later on, Hippocrates himself suggests that if a tumor “cannot be cut, it should be burned. If it cannot be burned, then it is incurable.” [21, 22]. It is sadly surprising to consider how current this can be still today, for several cancers.

Heat affects the architecture of cellular cytoskeleton; the molecular transport across the cell membrane; and the function of receptors, in a dose and time-dependent manner. Several causes have been attributed for the variable sensitivity of cancer cells to high temperatures. Mainly, mutated or underexpressed heat shock proteins increase cells sensitivity to heat; on the other side, in few cases a deregulation of these macro-molecules brings to an increased resistance [23, 24]. Nevertheless, tumors are known for their disorganized and compact vasculature, which is inefficient in dissipating heat; consequently, a strong, localized hyperthermia treatment has been demonstrated to be most effective against the tumors [25-29]. The appropriate balance between temperature and duration is the key for a correct balance between the desired cancer cell death and undesirable normal cell toxicity.

Several forms of hyperthermic treatments have been developed. Whole body hyperthermic therapy has been utilized by inducing an excessive overall heat production up to 42 °C for extended periods of time (few hours) [30-33]; the objective can be reached by injection of toxins to produce an hyperthermic reaction associated to unspecified immune response. Contact-based approaches see externally warming the patients by immersion in hot water or wax, or with high rate water perfusion blankets [34]. Other approaches for whole body hyperthermia uses extracorporeal circuit: the blood taken from the patient circulates into a heat exchanger and reenter the body providing high heating rate and essentially no toxicity [31, 35]. Less invasive methods employ electro-magnetic fields radiations ranging from radiofrequencies (RF), microwaves (MW), infrared (IR), visible light and even ultra-violet

frequencies; the absorption rates of the incident field is usually proportional to the square of the field strength, but the penetration depth depends on the frequency. RF spectrum ranges from 0.3 kHz up to 300 MHz, which correspond to wavelengths from 1'000 km to 1 m; for this reason, since able to penetrate the whole body without reducing power, RFs are widely used for radiation hyperthermia.

Regional hyperthermia therapy usually involves intratumoral placement of an electrode able to increase local temperature as high as 100 °C. Hyperthermia is achieved when temperature in the cell is raised a few degrees above 42 °C [36] for prolonged time. Instead, ablation therapies are specific treatments that cause total burn/elimination of targeted cells and requires temperatures of 50 °C and higher [37, 38], usually for short periods of time. Effective hyperthermic cancer therapy can be induced by either long period hyperthermia, or short duration ablation; eventually, both the treatment can be applied at the same time. Mild hyperthermia is insufficient per se to induce significant cell death and, therefore, is mostly used as an adjuvant treatment in combination with conventional radiation- and chemo-therapy [39-41]. This takes the form of an isolated limb perfusion of chemotherapy warmed to 42 – 45 °C for 1 hr or longer.

The nanotechnology approach to hyperthermic treatments uses electromagnetic fields as external source of energy, and magnetic nanoparticles as receiver and local heat transducer. The remarkable advantages include high resolution of application, and reduced invasiveness for sites deep into the body. Already approved by the American Food and Drug Administration

Agency (FDA), some gold and iron oxides (IOs) nanoparticles are actually used in clinical practice for hyperthermic therapies. Gold based nanoparticles show their high potential in combination with nIR laser [42-47]; at the submicron size range, they show particular plasmon resonance at wavelengths of lights approximately between 650 and 950 nm. As results the absorbed optical energy produce remarkable increase in temperature. Unfortunately, a big limitation is the poor penetration deep due to the high attenuation of nIR waves by the biological tissues. Differently, IOs nanomaterials are excited using RF magnetic fields, which easily penetrate the whole human body without sensible attenuation. The processes underling the heating of IOs vary depending on the particles size, and are deeply treated in **Chapter. 2**. Above all, IOs were widely investigated in medicine for their versatility in several biomedical applications as Magnetic Resonance Imaging (MRI), and bone regeneration.

To date, countless investigators devoted their efforts towards thermal treatments mediated by nanoparticles. The last decade saw many meaningful developments in all the aspects related to the scope, till the point that it took its steps from being a simple subsection of a more general field. Even if direct translatability requires further investigations on long term toxicology, recurring tumors, and metastasis, successful animal trials have been published reporting tumor full regression [48, 49]. Still, despite all these improvements, an efficient solution seems still far to be achieved.

In this view, one of the main issues can be found in the lack of a most general, quantitative model to compare the different results achieved upon the

most different experimental conditions (field generator power, *in-vitro* setups, and *in-vivo* tumor models). This can indeed undermine a correct understanding of the results in the community and generate confusion. As a consequence, guidelines for the design of efficient hyperthermia and ablation treatments are still missing; risks related to this absence are loss of focus on what is actually still needed to achieve efficient treatments, and diminished efficiency in the researchers efforts.

Also, all that “room at the bottom” is still far to be totally employed. Especially IOs particles offer huge opportunities for the construction of a multifunctional device, also operating as MRI imaging contrast agent [50-52] and drug delivery system [53], synergistically. These opportunities enlist within the many options already at reach today, but still waiting to be properly exploited.

Therefore, the goal of this thesis work is the development of rationally designed nanotechnology for hyperthermic application. This goal is pursued by fulfilling three aims: *i*) the definition of the requirements for an efficient hyperthermia; consequently, *ii*) the definition of guidelines (design maps) for the hyperthermic treatment of tumors with superparamagnetic nanoparticles; finally *iii*) the enlargement of the optimal design of IOs nanodevices to perform at their full potential, merging hyperthermic performances with not heat-related capabilities.

1.1.1. Outline

This dissertation is organized in a total of 5 Chapters, each of them closed with discussions on the results achieved. **Chapter. 1** and **Chapter. 5** are, respectively the introduction and conclusion of this work, plus proposed future works based on our findings.

Chapter. 2 presents the theoretical underpinnings of this work. The accepted theory [54] on power losses in superparamagnetic nanoparticles is run through from its basis; similar process is done for deduction of specific absorption rate (*SAR*). Considerations on parameters affecting this index and its validity as comparative model are discussed. Also, the mathematical model is further expanded to include temperature diffusion *in-vivo*.

Chapter. 3 deals with systematic analyses of the key factors for rational design of an efficient thermal therapy, as an attempt to generate a proper comparative model and design guidelines. *In-vitro* experiments and *in-silico* simulations are reported and their results discussed.

Chapter. 4 expounds on optimal design of systems based on superparamagnetic iron oxide (SPIO) particles, merging heating proprieties with other typical features of SPIOs never reported for the same system. It is developed the synthesis of a novel nanoconstruct, performing comparably with the best results in literature in heating, T_2 relaxation time, and magnetic dragging.

2. Theoretical model of heat generation and transport

Electric heating involves absorption of energy from a body exposed to an electro-magnetic field. A magnetic field is able to excite a magnetic particle which in turn develops a magnetization field. If the incident field is alternated, the induced magnetization follows the external field. An alternating magnetic field (AMF) ranging from $3 \cdot 10^2$ - $3 \cdot 10^8$ Hz (radiofrequencies) is particularly convenient for medical applications because it freely penetrates the human body and reaches the deepest sites. For biomedical applications, different heating mechanisms are involved depending on nanoparticle (NP) size. For example, heating of NPs smaller than ~ 100 nm is associated with Neel/Brownian relaxation, or hysteresis loss [54]; whereas Joule heating is the dominant effect for larger iron oxides (IOs). Hysteresis is generated by alternating magnetization of a multi-domain body, and hysteresis loss dominates for nanoparticles with a larger magnetic core (20 – 100 nm) [55]. Structural imperfections and impurities in the particle structure introduce irregularities which accumulate in singular points for the inner magnetic field within the volume. These discontinuities resolve forming magnetic boundaries between regions (Weiss domains) with different dipoles [56]. These generate coercivity and the total magnetization of the particles does not grow linearly with the external field; As a result, in alternating fields the reversal magnetization is also delayed, forming a loop in the magnetization *versus* applied field graph.

Superparamagnetism arises for particles small enough to not possess magnetic domain. Their inner dipole hence freely rotates within the applied field. In this chapter, the accepted theory [54] on power losses in superparamagnetic nanoparticles is reviewed starting from the first law of thermodynamics. From the same principle, with specific application to *in-vitro* experiments later described (**Chapter. 4**); the definition of specific absorption rate (*SAR*) is deducted. Still, the boundary conditions are such that the results are still valid for general purpose. The mathematical model is further expounded on to include temperature diffusion *in-vivo*, following Pennes' equations and their revision [57, 58]. This model is used to generate a simulation code whose results are reported in **Chapter 3**. Finally, considerations on *SAR*'s validity as comparative model are also discussed along with analysis of several parameters that influence it and, in the prospective of a proper design for both particles structure and field generator.

2.1. Magnetic loss power in radiofrequency regime

A superparamagnetic NP exposed to a radiofrequency (RF) alternate magnetic field (AMF) is subject to heating due to power dissipated from dipole relaxation. The mathematical model depicting the heat produced has been well defined by Rosensweig [54], who calculated the dissipated power per unit volume P of a colloidal suspension of NPs. Starting from the first law of thermodynamics applied to a constant density system:

$$dU = \delta W + \delta Q \quad [\text{J m}^{-3}] \quad (2-1)$$

Considering an adiabatic process (i.e. $\delta Q = 0$), the only contribution to the internal energy is provided by the magnetic work done on the particle:

$$dU = \delta W = \vec{H} \cdot d\vec{B} \quad [\text{J m}^{-3}] \quad (2-2)$$

here \vec{H} and \vec{B} are the magnetic field and its induction inside the particle, respectively. The fields are collinear to each other, thus the relationship is reduced to the simple product of their magnitude. The induction B is given by

$$B = \mu_0 (H + M) = \mu_0 (1 + \chi) H \quad [\text{T}] \quad (2-3)$$

$$M = \chi H \quad [\text{A m}^{-1}]$$

where magnetization M of particles is related to its magnetic susceptibility χ ; μ_0 is the magnetic permeability in the vacuum. Integration by parts leads to:

$$\Delta W = -\mu_0 \oint M dH \quad [\text{J m}^{-3}] \quad (2-4)$$

We can reduce the magnetization in an *in-phase* and an *out-of-phase* component into:

$$H(t) = H_0 \cos \omega t = \text{Re}[H_0 e^{i\omega t}] \quad [\text{A m}^{-1}] \quad (2-5)$$

$$M(t) = \text{Re}[\chi H_0 e^{i\omega t}] = H_0 (\chi' \cos \omega t + \chi'' \sin \omega t)$$

and the integral becomes:

$$\Delta W = \mu_0 \chi'' H_0^2 \int_0^{2\pi/\omega} \sin^2 \omega t dt = \mu_0 \chi'' H_0^2 \pi = \Delta U \quad [\text{J m}^{-3}] \quad (2-6)$$

This relationship shows that the only remaining factor responsible for energy variation in particle volume is the out-of-phase component of magnetic susceptibility, which take the name of “loss factor”. This loss factor relates the power dissipation to the intrinsic particle magnetic properties and therefore is

associated with its specific magnetization and relaxation times. Following the lead of Shliomis [59], Rosensweig reports the relaxation equations for static fluid subject to AMFs as:

$$\frac{\partial M(t)}{\partial t} = \frac{(M_0(t) - M(t))}{\tau} \quad [\text{A m}^{-1} \text{ s}^{-1}] \quad (2-7)$$

$$\chi'' = \chi_0 \frac{2\pi f\tau}{1 + (2\pi f\tau)^2} \quad [\text{a.u.}] \quad (2-8)$$

χ_0 is a constant more accurately defined in the following.

The final power lost per unit of volume is obtained multiplying for the field frequency f :

$$P = f \Delta U = f\mu_0 \chi'' H_0^2 \pi = f\mu_0 H_0^2 \pi \chi_0 \frac{2\pi f\tau}{1 + (2\pi f\tau)^2} \quad [\text{W m}^{-3}] \quad (2-9)$$

2.1.1. Magnetic equilibrium susceptibility

χ_0 actually also depends on the incident field. A conservative estimation approximates its value to the “chord” susceptibility associated with a Langevin function:

$$\chi_0 = \chi_i \frac{M}{M_s} = \chi_i L(\xi) = \chi_i \frac{3}{\xi} \left(\coth \xi - \frac{1}{\xi} \right) \quad [\text{a.u.}]$$

$$\xi = \mu_0 M_D V_M H / k_B T \quad [\text{a.u.}] \quad (2-10)$$

$$M_s = \phi M_D \quad [\text{A m}^{-1}]$$

$$\phi = V_M / V_f \quad [\text{a.u.}]$$

where: M_D and V_M are the domain magnetization and the magnetic volume of a suspended NP, respectively; k_B is the Boltzmann's constant; T the temperature. ϕ defines the volume fraction of the particles dispersed in the solution with total volume V_f , and is an fundamental scaling factor for the proper design of hyperthermia treatment; further discussion about is remanded to section 2.3.1 and 3.3.6 M_S is the magnetization saturation of the whole colloidal suspension. χ_i is derived as the initial susceptibility directly from the Langevin equation as:

$$\chi_i = (\partial M / \partial H)_i = \mu_0 \phi M_D^2 V_M / 3 k_B T \quad [\text{a.u.}] \quad (2-11)$$

Recently, Jánosfalvi et Al. [60] proposed that this approximation is reliable only for the typical low field ranges used for hyperthermia treatments. Based on their calculation, the chord susceptibility results in a negligible underestimation of the effective power losses for $H_0 < 30 \text{ kA m}^{-1}$. Here the difference is calculated to be ~8 %, and it reach the 20% for $H_0 = 100 \text{ kA m}^{-1}$.

2.1.2. Neel and Brown relaxation times

A particle exposed to AMFs rotates in line with applied field; the time required to complete this movement is called relaxation time. Two possible rotations can occur for a free particle without restrictions: (i) Neél relaxation of the inner dipole of the particle [61] and (ii) Brown relaxation of the whole particle inside the immersed medium (**Figure 2-1**). The effective relaxation time is dominated by the faster of the two:

$$\tau = (\tau_N^{-1} + \tau_B^{-1})^{-1} \quad [\text{s}] \quad (2-12)$$

Neél relaxation time is based on the ratio between the magnetization energy of the particle and its thermal energy. In this model, the contribution of magnetization energy is provided by a single anisotropy constant K , and a correct estimation of this value has been demonstrated to be highly effective on the objective of an efficient hyperthermia treatment [62, 63] (see paragraph 2.5).

$$\tau_N = \frac{\sqrt{\pi}}{2} \tau_0 \frac{\exp(KV_M / k_B T)}{\sqrt{KV_M / k_B T}} \quad [\text{s}] \quad (2-13)$$

τ_0 is an average relaxation time, $\sim 10^{-9}$ sec for IOs.

Brown relaxation occurs for particles in a wet environment. It takes into account whole particle rotation and the friction from medium viscosity η . The time elapsed between each leap is defined by the ratio between the viscosity and the thermal energy multiplied by hydrodynamic volume of the particle, V_H :

$$\tau_B = \frac{3\eta V_H}{k_B T} \quad [\text{s}] \quad (2-14)$$

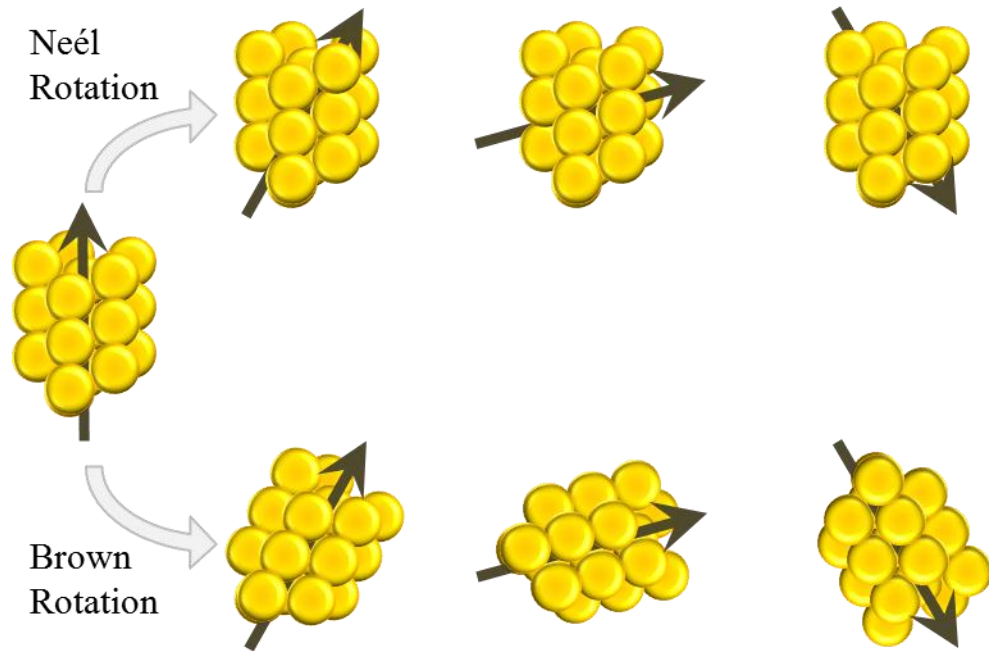


Figure 2-1. Neél and Brown relaxation modes.

The inner dipole of a superparamagnetic particle following an external magnetic field is subjected to two rotation modes. During Neél relaxation, the particle actual body remains still and the dipole rotates according to the external field. Instead, the Brown relaxation includes also the particles body alongside with the magnetic dipole.

2.2. Heat transport modeling

Application of **Equation (2-9)** for experimental quantifications of particles performances requires a further step in modeling of heat exchanges between the colloidal fluid and its surrounding. The experimental setups are shown in detail in section 3.3.1. Briefly, a solution of nanoparticles (typically magnetite, Fe_3O_4) with known iron concentration is positioned at the geometrical center of a magnetic coil; a typical volume of $\sim 600 \mu\text{l}$ of solution is stored in a tube and placed on a foam holder, which provides a first thermal insulation. The coil is hooked to an alternating current in RF regime and develops an AMF with tunable strength up to 10 kA m^{-1} ; at the same time, a constant flow of refrigerated water within the coil keeps its temperature constant $\sim 19.8 \text{ }^\circ\text{C}$ and functions as heat sink. The system is represented in **Figure 2-2**.

2.2.1. Application of first law of thermodynamics

For the system mentioned above it is convenient to apply the first law of thermodynamics in its formulation for fluids in flow, this time for non-adiabatic conditions:

$$\frac{\delta Q}{dt} - \frac{\delta W}{dt} = \iint_{c.s.} u \rho_f (\vec{v} \cdot \vec{n}) dS + \frac{\partial}{\partial t} \iiint_{c.v.} u \rho_f dV \quad [\text{W}] \quad (2-15)$$

which imposes energy conservation between the instantaneous heat $\frac{\delta Q}{dt}$ added

to the volume unit and its instantaneous work $\frac{\delta W}{dt}$ done on the environment.

The terms on the right are the net rate of energy transport out of the control volume (with fluid velocity \vec{v}) across its surface S , and the rate of accumulation of total energy within the control volume V . The sole contribution to the total energy is the specific internal energy u of the fluid since potential energy is negligible and the kinetic energy does not apply for fluid not in motion. Similarly, the first of the right-hand terms of **Equation (2-15)** equals zero; ρ_f represents the fluid density.

The heat rate provided by the magnetic loss is independent from other heat exchanges q that may occur at the interface between the liquid and the surrounding; hence Rosensweig's results are still valid:

$$\frac{\delta Q}{dt} = -q \quad [\text{W}] \quad (2-16)$$

$$- \frac{\delta W}{dt} = PV_f$$

The pedix f denotes the whole fluid. As for the second right-hand term in **Equation (2-15)**, considering the total variation on internal energy dU , it can be written as:

$$dU = C_v dT + \left[T \left(\frac{\partial p}{\partial T} \right)_v - p \right] dV \quad [\text{J}] \quad (2-17)$$

where: C_v is the heat capacity at constant volume; p is the pressure; $\left(\frac{\partial p}{\partial T} \right)_v$ is

the partial derivative of the pressure with respect to the temperature at constant volume; dT and dV define the total variation in temperature and volume, respectively. The latter is considered $dV \approx 0$ since the fluid volume change is

assumed negligible. Rewriting the equation in specific formulations and solving, the integral results in:

$$PV_f - q = c_p \rho_f \frac{dT}{dt} V_f \quad [\text{W}] \quad (2-18)$$

with c_p being the specific heat conductivity at constant pressure.

2.2.2. Heat transport and sample tube geometry

Instantaneous heat exchanges q can be calculated based on convective and conductive thermal transfers between the heat sources in the fluid to the heat sink represented by the coil. The axial center of the vial is defined as the effective fluid temperature $T_f(t)$, and the coil at constant temperature T_a .

The cylindrical geometry is represented in **Figure 2-2**. It consists of three sections: (i) the cylindrical main body of the tube, with height L and radius r_e , surrounded by air; (ii) a first truncated cone, with height H , larger radius r_e , and smaller radius r_1 , surrounded by air; (iii) a second truncated cone having height J , larger radius r_1 , and smaller radius r_2 , inside an annulus truncated cone section of polystyrene, larger radius r_{1+x} and smaller radius r_{2+x} . For sake of simplicity, the tube walls are approximated to have infinitesimal width. The temperature of the fluid is monitored using an optical probe positioned at the center of the tube.

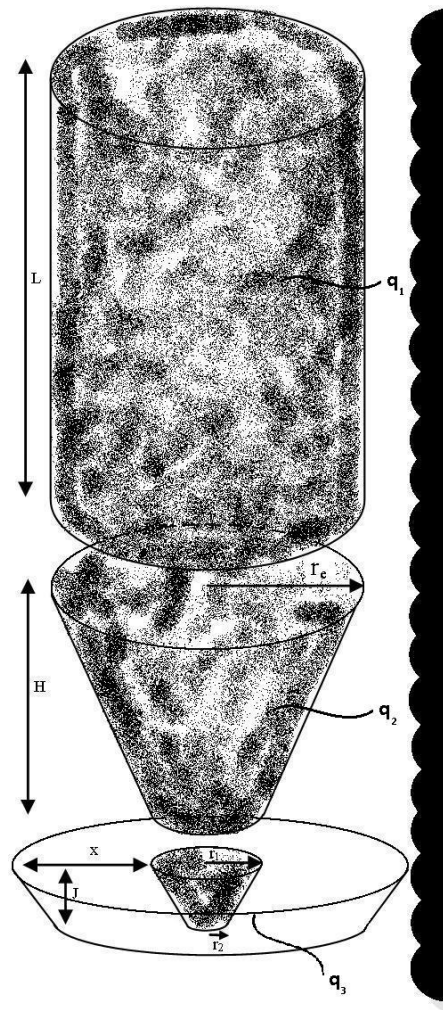


Figure 2-2. Modeling of heat transport through a vial.

The Eppendorf tube used for *in-vitro* characterization has been modeled with a 3-parts geometry. The first is a cylindrical section defined by height L and radius r_e . The second section is reverted truncated cone, height H , larger radius r_e , smaller radius r_1 . The third part is a second, smaller truncated cone, height J , larger radius r_1 , smaller radius r_2 ; this last section is surrounded by an annulus truncated cone section of polystyrene which model the tube holder; its height is defined as J , the larger radius is r_1+x and the smaller radius r_2+x . The inner of the tube contains the colloidal suspension of nanoparticles with temperature T_f . The temperature wall, approximated to have infinitesimal width has temperature T_e . Apart for the third section, the outside of the tube is considered as air up to a distance r_2+x from the center; where the presence of the magnetic coil is modeled as a heat sink with constant temperature T_a .

Total volume of the fluid is

$$V_f = \pi r_e^2 L + \frac{1}{3} \pi (J + H)(r_e^2 - r_2^2) \quad [\text{m}^3] \quad (2-19)$$

and the instantaneous heat transfers formulas applied to this geometry are

$$q = hA \Delta T = \begin{cases} h 2 \pi r_e L (T' - T'') & , (i) \\ h \pi (r_1 + r_2) \sqrt{H^2 + (r_1 - r_2)^2} (T' - T'') & , (ii) \\ h \pi (r_1 + r_2) \sqrt{J^2 + (r_1 - r_2)^2} (T' - T'') & , (iii) \end{cases} \quad [\text{W}] \quad (2-20)$$

for convection heating; where A refers to the exchanging surface, and h indicates the exchange coefficient. For conductive heating through the annulus in the third section we have:

$$\begin{aligned} q &= -kA \frac{dT}{dr} \\ \Rightarrow \int_0^x \frac{q}{A} dr &= - \int_{T''}^{T'} k dT \\ \Rightarrow \int_0^x \frac{q}{(r_1 + r_2 + 2x) \sqrt{J^2 + (r_1 - r_2)^2}} dr &= \int_{T''}^{T'} k dT \\ \Rightarrow q &= \frac{k 2 \pi \sqrt{J^2 + (r_1 - r_2)^2}}{\ln(r_1 + r_2 + 2x) - \ln(r_1 + r_2)} (T'' - T') & , (iii) \end{aligned} \quad [\text{W}] \quad (2-21)$$

Replacing the proper parameters for each section:

$$\begin{aligned} q_1 &= \begin{cases} h_a 2 \pi r_e L (T_e - T_a) \\ h_f 2 \pi r_e L (T_f - T_e) \end{cases} \\ q_2 &= \begin{cases} h_a \pi (r_e + r_1) \sqrt{H^2 + (r_e - r_1)^2} (T_e - T_a) \\ h_f \pi (r_e + r_1) \sqrt{H^2 + (r_e - r_1)^2} (T_f - T_e) \end{cases} \\ q_3 &= \begin{cases} \frac{k 2 \pi \sqrt{J^2 + (r_1 - r_2)^2}}{\ln(r_1 + r_2 + 2x) - \ln(r_1 + r_2)} (T_e - T_a) \\ h_f \pi (r_1 + r_2) \sqrt{J^2 + (r_1 - r_2)^2} (T_f - T_e) \end{cases} \end{aligned} \quad [\text{W}] \quad (2-22)$$

where h_a and h_f are heat exchange coefficients for air and fluid, respectively; k is the thermal conductivity for the polystyrene holder; and T_e is the tube temperature at the wall. The final formulation is obtained imposing heat flux continuity and summing each contribution:

$$T_f - T_a = \left\{ \begin{array}{l} q_1 \frac{1}{2\pi r_e L} \left(\frac{1}{h_a} + \frac{1}{h_f} \right) = q_1 R_1 \\ q_2 \frac{1}{\pi (r_e + r_1) \sqrt{H^2 + (r_e - r_1)^2}} \left(\frac{1}{h_a} + \frac{1}{h_f} \right) = q_2 R_2 \\ q_3 \frac{1}{\pi \sqrt{J^2 + (r_1 - r_2)^2}} \left(\frac{\ln(r_1 + r_2 + 2x) - \ln(r_1 + r_2)}{k} + \frac{1}{h_f (r_1 + r_2)} \right) = q_3 R_3 \end{array} \right. \quad [\text{K}] \quad (2-23)$$

$$q = \sum q_i = (T_f - T_a) \frac{R_2 R_3 + R_1 R_3 + R_1 R_2}{R_1 R_2 R_3} = \frac{T_f - T_a}{R} \quad [\text{W}] \quad (2-24)$$

where R indicates the thermal resistance between fluid and ambient.

2.2.3. Determining the temperature-time relationship

Equation (2-18) now becomes

$$PV_f - \frac{T_f(t) - T_a}{R} = c_p \rho_f \frac{dT_f(t)}{dt} V_f \quad [\text{W}] \quad (2-25)$$

or

$$\frac{P}{c_p \rho_f} - \frac{T_f(t) - T_a}{c_p \rho_f V_f R} = \frac{dT_f(t)}{dt} \quad [\text{K s}^{-1}] \quad (2-26)$$

P is actually temperature dependent. In the interest of this study, it is convenient to consider the nanoparticle power dissipation as constant within the typical range of temperature used in hyperthermia applications.

Defining:

$$B = P / c_p \rho_f \quad [\text{K s}^{-1}] \quad (2-27)$$

$$A = \frac{1}{c_p \rho_f R V_f} \quad [\text{s}^{-1}]$$

Equation (2-26) is rewritten as:

$$\frac{dT_f(t)}{dt} = B + T_a A - T_f(t) A \quad [\text{K s}^{-1}] \quad (2-28)$$

which solution is

$$T_f(t) = C_1 e^{-At} + \frac{B}{A} + T_a \quad [\text{K}] \quad (2-29)$$

The boundary condition is provided by the equilibrium temperature reached before turning on the AMF and thus:

$$T_f(0) = T_a \quad [\text{K}] \quad (2-30)$$

$$T_a = C_1 + \frac{B}{A} + T_a \Rightarrow C_1 = -\frac{B}{A}$$

Finally, the close formulation of temperature increase is:

$$T_f(t) = T_a + \frac{B}{A} (1 - e^{-At}) = T_a - PRV_f \left(e^{\frac{-t}{c_p \rho_f R V_f}} - 1 \right) \quad [\text{K}] \quad (2-31)$$

In this formula the roles of each component that affect the temperature curve are clear: the term B contains the source of heating and is responsible for the initial temperature increment. The factor A is defined to include the

geometrical conditions and heat exchange terms, which dampens the temperature increment towards a new equilibrium. Finally, their ratio represents the total temperature variation. These are depicted in **Figure 2-3**.

It is important to note this is a general formula. Due to the decoupling between the heat source and the heat exchange terms, it is possible to independently identify these two contributions starting from the temperature measurement of any object with a homogenous heat transport. It is worth to be noted that correct separation between these two contributions is only possible thanks to the choice of the condition in **Equation (2-30)**, which requires the experiment is conducted starting from equilibrium conditions.

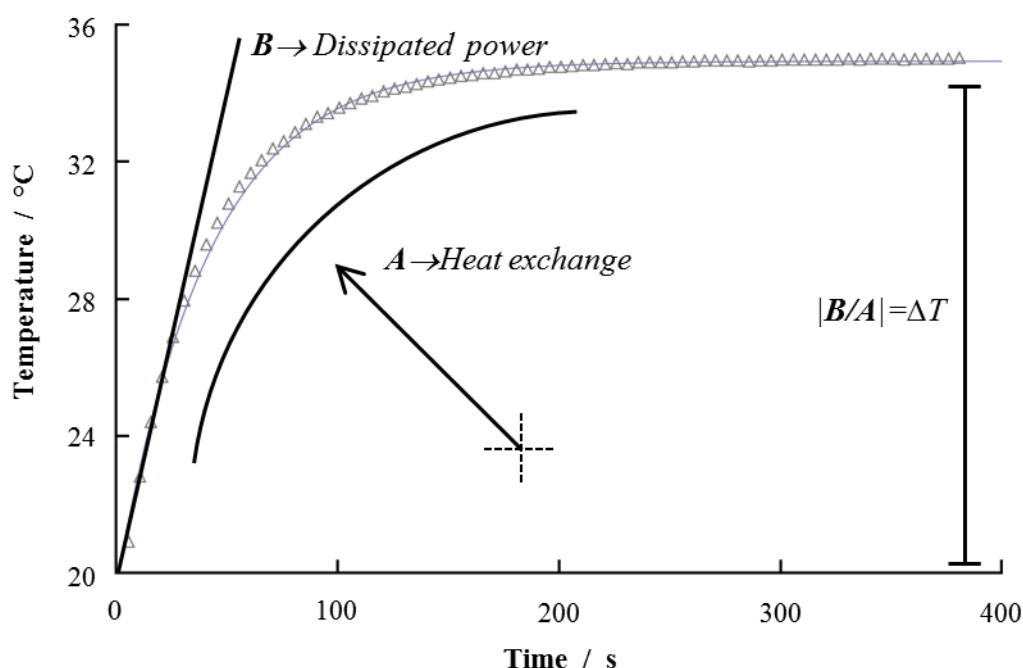


Figure 2-3. Graphical representation of the terms A and B in Equation (2-31).

It can be appreciated the decoupling of heating source, associated with B , and the heat exchanges contained in A . Also, these two factors indicate for the total temperature variation. B is connected to the particles dissipated power by the initial slope of the temperature profile and is independent from the single experiment; A is responsible for the establishment of new equilibrium and is determined by experimental conditions. Plotted triangles identify measured data points, and the solid line is the curve interpolated by **Equation (2-31)**. Temperature profile is obtained by 14 nm magnetite spherical particles, concentration of 0.23 mg ml^{-1} , excited by a $4 \text{ kA m}^{-1} - 30 \text{ MHz}$ AMF.

2.3. Definition of specific absorption rate

Outcome from *in-vitro* experiments as mentioned above are the fluid temperature excursion $T_f(t)$. From this, two main results can be obtained: the maximum rise in temperature ΔT , and the power losses. For the final goal of an efficient *in-vivo* hyperthermia, ΔT is the utmost important reference since quantifies the heat provided with the treatment. Unfortunately, ΔT strictly depends on specific experimental conditions; it takes into accounts the geometry of experimental setup, NPs employed, their concentration, and/or the blood perfusion. For this reason, it is inadequate to define the quality of the treatment but, more importantly, cannot be applied for the comparison of different methodologies. Differently, the specific absorption rate (SAR) is commonly used in literature to quantify the efficiency of a body to convert magnetic energy in heat.

2.3.1. SAR_f and SAR_{NP}

Equation (2-25) can be rewritten to highlight the work done per unit of mass:

$$PV_f - \frac{T_f(t) - T_a}{R} = c_p \rho_f \frac{dT_f(t)}{dt} V_f \quad [\text{W}] \quad (2-25)$$

$$\frac{P}{\rho_f} - \frac{T_f(t) - T_a}{RV_f \rho_f} = c_p \frac{dT_f(t)}{dt} \quad [\text{W kg}^{-1}] \quad (2-32)$$

The second term on the left hand side defines the heat transfers towards the environment. Looking at the very first moments after the magnetic field is turned on, for $t = 0$, $T_f(0) = T_a$ and there are no exchanges:

$$\frac{P}{\rho_f} = \frac{\Delta T_f}{\Delta t} \Bigg|_{t=0} c_p = SAR_f \quad [\text{W kg}^{-1}] \quad (2-33)$$

This result defines a contribution to the heating which is time-independent, identified by the initial, linear region of the exponential function in **Equation (2-31)**. Therefore, the correct computing of the NPs contribution to heating is only possible for $T_f(0) = T_a$, which justify the previous choice of **Equation (2-30)**. **Equation (2-33)** provides two methods for estimation of the whole fluid SAR_f : a computational calculation based on Rosensweig equation, and an empirical measurement based on $T_f(t)$.

Still, our objective is not the heating efficiency of the fluid, rather the quality of the NPs in solution. From **Equations (2-10)** and **(2-11)**, the power loss for volume unit of fluid P is directly proportional to the volume fraction ϕ ; hence, a similar normalization can be obtained by dividing both terms of **Equation (2-33)** by the mass fraction m_{NP}

$$m_{MNP} = \frac{\rho_{NP} V_{NP}}{\rho_f V_f} = \phi \rho_{NP} / \rho_f \quad [\text{a.u.}] \quad (2-34)$$

$$\frac{P_{NP}}{\rho_{NP}} = \frac{\Delta T_f}{\Delta t} \Bigg|_{t=0} \frac{c_p}{m_{NP}} = SAR_{NP} \quad [\text{W kg}^{-1}] \quad (2-35)$$

Where $P_{NP} = \frac{P}{\phi}$ is the loss power per unit volume of nanoparticle; similarly,

SAR_{NP} represents the definition of SAR of the magnetic nanoparticles alone.

Note that SAR_{NP} does not depend on the NPs concentration but solely on P_{NP} and their density.

SAR_{NP} is commonly referred in the literature simply as SAR . Therefore, in the following, the same notation will be adopted, if not otherwise indicated

2.4. Finite element modeling of the temperature field

In collaboration with the group of Prof. Luigi Preziosi from the Dept. of Mathematical Science at the Polytechnic of Turin, we used the Pennes' bio-heat equations [64] to quantify the temperature field within a domain of interest. The defined model describes the heat transfer phenomena in biological tissues, accounting for both healthy and neoplastic ones. The contributions in the temperature increase include: *i*) the specific heat provided by magnetic nanoparticles uniformly distributed, and *ii*) the non-specific heat due to salts dispersed in the physiological fluids. Similarly, blood perfusion of the tissue is modeled as a distributed heat sink within the computational domain. This is a square composed of two areas: a central region representing the tumor where magnetic nanoparticles could be laid uniformly (Ω_2), and an outer region representing the surrounding healthy tissue (Ω_1). The whole region is permeated by blood vessels, such that the heat exchange of the healthy tissue with these is also extended to the region Ω_2 as described in [65].

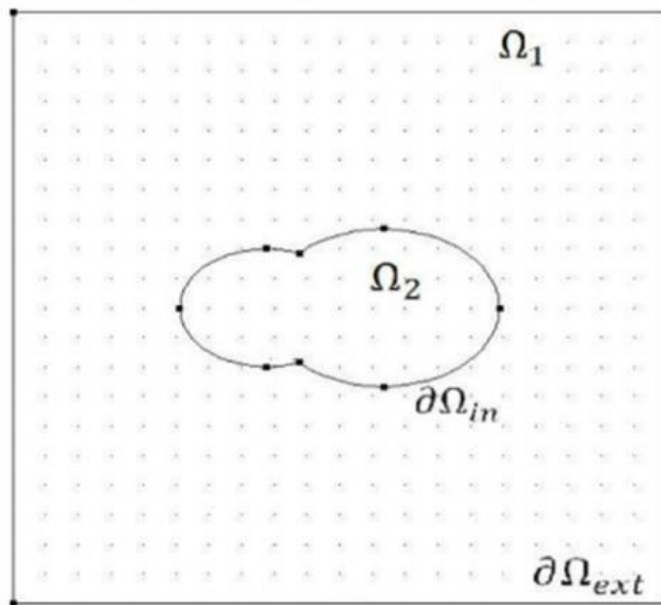


Figure 2-4. Domain of interest for the modeling of temperature field.

The region of interest is composed by a 10 mm x 10 mm square for a total of 3816 triangular elements. The outer region Ω_1 corresponds to healthy tissue; the sole heating here is generating by the non-specific contribution of salts dispersed in physiological tissues; the inner region Ω_2 corresponds to the tumor area, which contains both specific and non-specific heating sources. Temperature diffusion in the whole area is simulated for different particles concentrations and perfusion rates.

The equations describing the temperature evolution within the domain are the following

$$\rho_1 c_1 \frac{\partial T}{\partial t} = \nabla \cdot (k_1 \nabla T) - \rho_{bl} c_{bl} w_{bl,1} (T - T_{bl}) + Q_1, \text{ in } \Omega_1 \quad [\text{W mm}^{-1}] \quad (2-36)$$

$$\rho_2 c_2 \frac{\partial T}{\partial t} = \nabla \cdot (k_2 \nabla T) - \rho_{bl} c_{bl} w_{bl,2} (T - T_{bl}) + Q_2, \text{ in } \Omega_2 \quad [\text{W mm}^{-1}] \quad (2-37)$$

$$[[T]] = 0 \quad \text{on } \partial\Omega_{in} \quad [\text{K}] \quad (2-38)$$

$$(k_1 \nabla T) \cdot \vec{n} = (k_2 \nabla T) \cdot \vec{n} \quad \text{on } \partial\Omega_{in} \quad [\text{W mm}^{-2}] \quad (2-39)$$

$$(k_1 \nabla T) \cdot \vec{n} = -h_v (T - T_{bl}) \quad \text{on } \partial\Omega_{ext} \quad [\text{W mm}^{-2}] \quad (2-40)$$

$$T(t = 0) = 37 \text{ } ^\circ\text{C} \quad \text{in } \Omega_1 \cup \Omega_2 \quad [^\circ\text{C}] \quad (2-41)$$

where Q_i [W mm^{-1}] is the heat power density generated inside the region Ω_i ; k_i , ρ_i and c_i are respectively the thermal conductivity [$\text{W mm}^{-1} \text{K}^{-1}$], the density [kg mm^{-3}] and specific heat capacity [$\text{J kg}^{-1} \text{K}^{-1}$] of the domain under consideration, Ω_i , with $i = 1, 2$. All of the terms in Ω_2 are defined according to the mixture theory [66, 67] for porous continua, it follows $\rho_2 = \rho_1(1 - \phi) + \rho_{NP} \phi$, $c_2 = c_1(1 - \phi) + c_{NP} \phi$, and $k_2 = k_1(1 - \phi) + k_{NP} \phi$. The perfusion parameters $w_{bl,1}$ and $w_{bl,2}$ are the tissue perfusion rates (s^{-1}) in Ω_1 and Ω_2 respectively, which have the following explicit expression, following a modified version of the model presented in [68, 69],

$$w_{bl,1} = \begin{cases} w_{bl,1}^0 & \text{if } T \leq 41 \text{ } ^\circ\text{C} \\ w_{bl,1}^0 e^{-\int_0^t A e^{-\Delta E / (RT(\tau))} d\tau} & \text{if } T > 41 \text{ } ^\circ\text{C} \end{cases} \quad \text{in } \Omega_1 \quad [\text{s}^{-1}] \quad (2-42)$$

$$w_{bl,2} = \begin{cases} w_{bl,2}^0 & \text{if } T \leq 41 \text{ } ^\circ\text{C} \\ w_{bl,2}^0 e^{-\int_0^t A e^{-\Delta E / (RT(\tau))} d\tau} & \text{if } T > 41 \text{ } ^\circ\text{C} \end{cases} \quad \text{in } \Omega_2 \quad [\text{s}^{-1}] \quad (2-43)$$

where R is the universal gas constant; A is the frequency factor; ΔE is the activation energy; $w_{bl,1}^0$ and $w_{bl,2}^0$ are the baseline perfusion values for the tissue. **Table 2-1** lists all the numerical values used during the computations. Whilst in Ω_1 the non-specific heating given by the salts dispersed in the physiological fluids is the sole source of heat, in Ω_2 is also considered the specific contribution from the magnetic NPs. Therefore, it follows

$$Q_1 = P_{NaCl} \phi_{NaCl} = SAR_{NaCl} \rho_{NaCl} \phi_{NaCl} \quad [\text{W mm}^{-1}] \quad (2-44)$$

$$Q_2 = P_{NaCl} \phi_{NaCl} + P_{NP} \phi = SAR_{NaCl} \rho_{NaCl} \phi_{NaCl} + SAR_f \rho_f \phi = SAR_f \rho_f \phi \quad [\text{W mm}^{-1}] \quad (2-45)$$

The system of **Equation (2-36) – (2-45)** is solved using the finite element software (FEM) Comsol[®] (version 3.5a), with direct UMFPACK linear system solver. During calculations, relative and absolute tolerances are fixed to 0.01 and 0.001, respectively. The computational mesh consists of 3816 triangular elements, simulating a 2D square domain of 10 mm side.

Parameter	Description	Value	Ref.
T_{bl}	Blood temperature	$273.15 + 37 \text{ K}$	Known
ρ_{bl}	Blood density	$1.06 \cdot 10^{-6} \text{ kg mm}^{-3}$	[70]
ρ_I	Tissue density	$1.06 \cdot 10^{-6} \text{ kg mm}^{-3}$	[69]
c_{bl}	Blood specific heat capacity	$3.59 \cdot 10^3 \text{ J kg}^{-1} \text{ K}^{-1}$	[71]
c_I	Tissue specific heat capacity	$3.47 \cdot 10^3 \text{ J kg}^{-1} \text{ K}^{-1}$	[72]
k_I	Tissue thermal conductivity	$0.51 \cdot 10^{-3} \text{ W mm}^{-1} \text{ K}^{-1}$	[69]
A	Frequency factor	$1.98 \cdot 10^6 \text{ s}^{-1}$	[69, 73]
ΔE	Activation energy	$6.67 \cdot 10^5 \text{ J mol}^{-1}$	[69, 73]
R	Universal gas constant	$8.314 \text{ J mol K}^{-1}$	Known
SAR_{NaCl}	Tissue SAR	450 W kg^{-1}	From experiments
SAR	Tissue + NPs SAR	900 W kg^{-1}	From experiments
h_v	Heat exchange coefficient	$1.65 \cdot 10^{-3} \text{ W mm}^{-2} \text{ K}^{-1}$	From exp., and in the range of [74]

Table 2-1. Parameters used in finite element simulations.

2.5. Discussion on SAR limitation as evaluating parameter

Looking at **Equation (2-9)**, it can be noted that the effects on heating for an exposed particle to RF fields is composed of two main contributes. A first component is solely dependent on the applied field (H_0, f); a second component is primarily dependent on the particle properties (d, K, M_s), and only in given limits on the field. It must be here considered that, as for **Equations (2-10)** the chord susceptibility χ_0 also depends on the field strength H_0 for each given particle diameter d and saturation magnetization M_s :

$$SAR \propto H_0^2 f \chi_0(d, M_s, H_0) \Phi(d, K, f) \quad [\text{W kg}^{-1}] \quad (2-46)$$

$$\text{With } \Phi(d, K, f) = \frac{2\pi f \tau(d, K)}{1 + (2\pi f \tau(d, K))^2}.$$

In order to effectively quantify how the variation in the field strength can be reverted on the chord susceptibility, it is useful to identify its maximum sensitivity over H_0 . A sensitivity function $s_{x_i}^f = \frac{\partial f}{\partial x_i} \frac{x_i}{f}$ quantifies the variation that a study function $f(x_i, x_{ii}, x_{iii}, \dots)$ undergoes, compared to the variation of the parameter x_i of interest. A null sensitivity function indicates independence from the parameter; whereas a value of 1 indicates a variation of f in the same entity of the variation for x_i .

The close computation of $s_{H_0}^{\chi_0}$ as function of both particle diameter and saturation magnetization is not trivial, but for the scope of this work, a numerical resolution can be considered sufficient. **Figure 2-5A** plots the

values $s_{H_0}^{z_0}$ assumes for ranges of d and M_s typically found in biomedical applications. At 100 emu g^{-1} , the figure shows values identically equal to zero only for small particles ($\leq 5 \text{ nm}$) diameter; then, the sensitivity functions quickly decreases to reach a minimum of -1 for diameters larger than 20 nm and field strengths higher than 10 kA m^{-1} . Improved magnetization saturation (e.g. 200 emu g^{-1}) shifts the decreasing curve towards smaller particles ($\leq 2 \text{ nm}$); whereas for an M_s of $\sim 20 \text{ emu g}^{-1}$, $s_{H_0}^{z_0}$ is calculated to rest on zero up to 10 nm and then decreases till it reaches the value of -1 for diameter greater than 22 nm and field strengths higher than 45 kAm^{-1} .

A similar approach can be used to evaluate the dependence of the factor $\Phi = \frac{2\pi f\tau}{1 + (2\pi f\tau)^2}$ from the applied frequency. **Figure 2-5B** plots the function s_f^Φ calculated for d up to 30 nm and an anisotropy constant K ranging between 3 and 300 kJ m^{-3} ; this range covers one order of magnitude above and below the bulk value for magnetite (Fe_3O_4) and maghemite ($\gamma\text{-Fe}_2\text{O}_3$) crystals. In these ranges, the sensitivity function s_f^Φ is negligibly dependent on the frequency. Instead, its calculated values abruptly drop from 1 to -1 as soon as the nanoparticle size increases over the resonance diameter, which is characteristic for each given crystalline energy value of the material. This resonance diameter shifts from $\sim 25 \text{ nm}$ at 3 kJ m^{-3} to $\sim 6 \text{ nm}$ at 300 kJ m^{-3} .

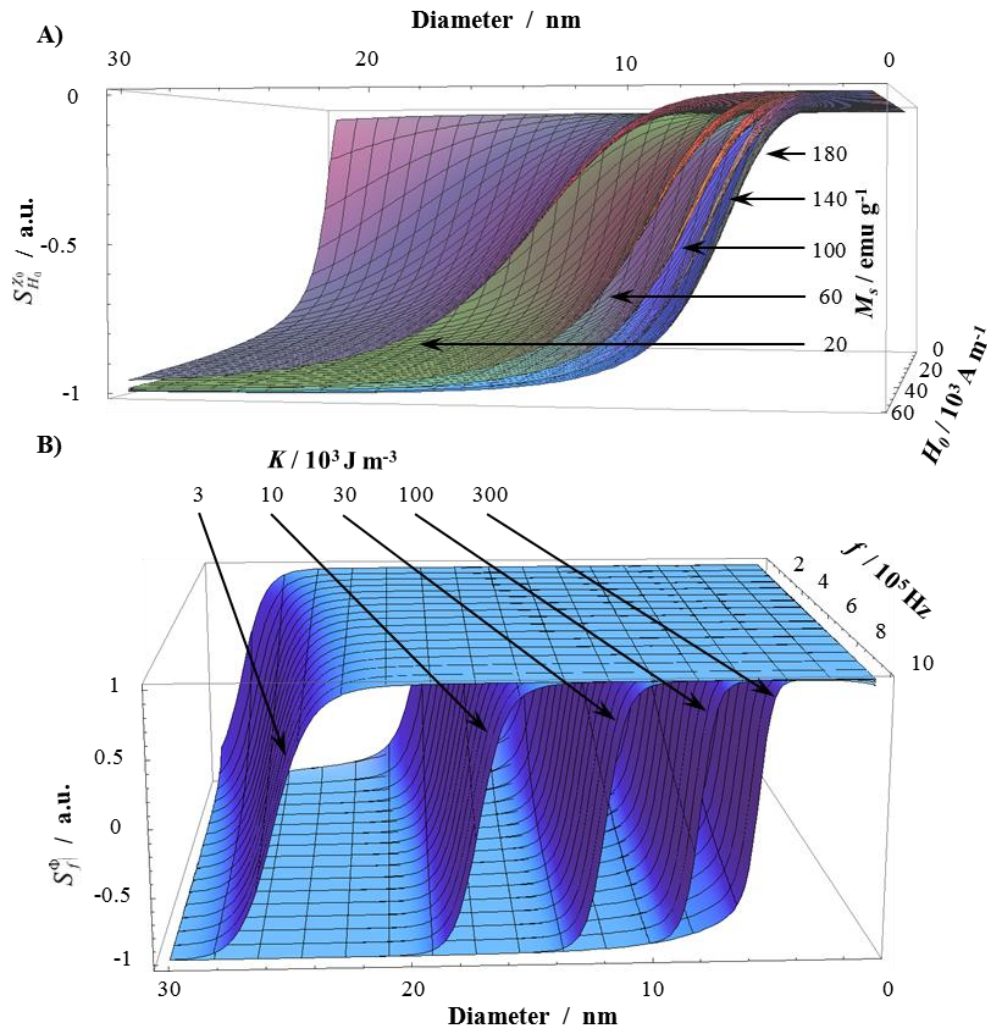


Figure 2-5. Sensitivity analysis of the imaginary susceptibility χ'' .

The imaginary susceptibility is divided in its two components χ_0 and

$\Phi = \frac{2\pi f\tau}{1 + (2\pi f\tau)^2}$. In panel (A) the sensitivity $S_{H_0}^{\chi_0}$ is calculated for field

strength H_0 ranging from 0 to 60 kA m⁻¹, particle diameter up to 30 nm, and saturation magnetization M_s varying from 20 to 180 emu g⁻¹. Panel (B) shows

the sensitivity S_f^{Φ} calculated for frequencies $f = 0.1 \div 1$ MHz, diameter $d =$

0 ÷ 60 nm, and crystalline anisotropy $K = 3\text{-}300$ kJ m⁻³. For both χ_0 and Φ the maximum sensitivity (over H_0 and f) never exceeds the value of ± 1 . This indicates, at the most, linear proportionality between the variations of the functions and these parameters, respectively. The simulations consider conditions ranges that widely include typical biomedical applications.

Based on the relationship (2-46), some authors suggested the use of a derived, more specific index [75, 76] in the attempt to have a system-independent parameter, called intrinsic loss power (*ILP*):

$$ILP = SAR / (H_0^2 f) = \frac{\mu_0 \pi}{\rho} \chi_0 \Phi \quad [(\text{m}^2 \text{s}^{-1} \text{A}^{-1})^2] \quad (2-47)$$

Such normalization would bring an intrinsic uncertainty in the effective particle efficiency, which will fall between 0.25 % and 200 % of the so calculated value. Several considerations may be taken to highly reduce this range of possibilities and calculate a more efficient index to compare the heating quality of particles characterized under different magnetic fields. Such calculations would deserve proper discussions and deep-in considerations in a separate form; for the sake of simplicity *ILP* will be considered as approximated in **Equation (2-47)** in the following work; this will not eventually undermine the drawn conclusions.

In conclusion, *ILP* could be less intuitive but, as far the heating process is related to superparamagnetic behaviors, it provides a better instrument to compare, in first approximation, results from different works and experimental system. In **Table 2-2** are reported a series of *SAR* values from literature, compared with the calculated *ILP*. Still, *SAR* remains the main index used in literature to evaluate the quality of achieved results.

#	Reference	Material	Diameter [nm]	$f \times H^2$ [A ² m ⁻² s ⁻¹]	SAR [W kg ⁻¹]	ILP [(m ² s ⁻¹ A ⁻¹) ²]
1	[77]	γ -Fe ₂ O ₃	5.3	4.3·10 ¹⁴	4.0·10 ³	9.0·10 ⁻¹²
2	[77]	γ -Fe ₂ O ₃	6.7	4.3·10 ¹⁴	1.4·10 ⁴	3.3·10 ⁻¹¹
3	[78]	γ -Fe ₂ O ₃	9	4.3·10 ¹³	1.8·10 ³	4.1·10 ⁻¹¹
4	[78]	γ -Fe ₂ O ₃	25	4.3·10 ¹³	2.5·10 ³	5.9·10 ⁻¹¹
5	[77]	γ -Fe ₂ O ₃	8	4.3·10 ¹⁴	3.7·10 ⁴	8.6·10 ⁻¹¹
6	[79]	γ -Fe ₂ O ₃	10.9	8.0·10 ¹¹	2.0·10 ²	2.5·10 ⁻¹⁰
7	[79]	γ -Fe ₂ O ₃	10.9	1.2·10 ¹²	3.8·10 ²	3.1·10 ⁻¹⁰
8	[79]	γ -Fe ₂ O ₃	10.9	1.0·10 ¹²	5.2·10 ²	5.3·10 ⁻¹⁰
9	[79]	γ -Fe ₂ O ₃	10.9	9.0·10 ¹¹	5.0·10 ²	5.5·10 ⁻¹⁰
10	[77]	γ -Fe ₂ O ₃	10.2	4.3·10 ¹⁴	2.8·10 ⁵	6.4·10 ⁻¹⁰
11	[77]	γ -Fe ₂ O ₃	16.5	4.3·10 ¹⁴	1.7·10 ⁶	3.8·10 ⁻⁹
12	[80]	Zn _{0.4} Co _{0.6} Fe ₂ O ₄ @ Zn _{0.4} Mn _{0.6} Fe ₂ O ₄	15	7.0·10 ¹⁴	3.9·10 ⁶	5.6·10 ⁻⁹
13	[80]	MnFe ₂ O ₄ @ CoFe ₂ O ₄	15	7.0·10 ¹⁴	3.0·10 ⁶	4.4·10 ⁻⁹
14	[62]	MnFe ₂ O ₄	15	7.0·10 ¹⁴	4.4·10 ⁵	6.3·10 ⁻¹⁰
15	[81]	Fe ₃ O ₄ :Fe ₂ O ₃ in 3:2 ratio	13	3.1·10 ¹²	1.6·10 ⁴	5.2·10 ⁻⁹
16	[62]	Fe ₃ O ₄	9	7.0·10 ¹⁴	1.5·10 ⁵	2.2·10 ⁻¹⁰
17	[62]	Fe ₃ O ₄	15	7.0·10 ¹⁴	3.3·10 ⁵	4.8·10 ⁻¹⁰
18	[62]	Fe ₃ O ₄	12	7.0·10 ¹⁴	3.5·10 ⁵	5.0·10 ⁻¹⁰
19	[82]	Fe ₃ O ₄	8	5.7·10 ¹³	5.3·10 ⁴	9.2·10 ⁻¹⁰
20	[82]	Fe ₃ O ₄	8	9.2·10 ¹²	1.7·10 ⁴	1.9·10 ⁻⁹
21	[75]	Fe ₃ O ₄	12.5	6.1·10 ¹²	2.2·10 ⁴	3.6·10 ⁻⁹
22	[75]	Fe ₃ O ₄	15.7	6.1·10 ¹²	2.8·10 ⁴	4.6·10 ⁻⁹
23	[62]	Fe ₂ O ₄ @CoFe ₂ O ₄	15	7.0·10 ¹⁴	2.8·10 ⁶	4.0·10 ⁻⁹
24	[62]	CoFe ₂ O ₄ @ MnFe ₂ O ₄	15	7.0·10 ¹⁴	2.3·10 ⁶	3.3·10 ⁻⁹
25	[62]	CoFe ₂ O ₄ @ Fe ₂ O ₄	15	7.0·10 ¹⁴	1.1·10 ⁶	1.6·10 ⁻⁹

26	[77]	Co-Fe ₂ O ₄	3.9	$4.3 \cdot 10^{14}$	$4.0 \cdot 10^2$	$9.3 \cdot 10^{-11}$
27	[62]	Co-Fe ₂ O ₄	9	$7.0 \cdot 10^{14}$	$1.0 \cdot 10^5$	$1.4 \cdot 10^{-10}$
28	[77]	Co-Fe ₂ O ₄	9.1	$4.3 \cdot 10^{14}$	$3.6 \cdot 10^5$	$8.4 \cdot 10^{-10}$
29	[83]	Bionized nanoferrite	28	$1.1 \cdot 10^{15}$	$2.1 \cdot 10^5$	$1.9 \cdot 10^{-10}$
30	[83]	Bionized nanoferrite	28	$1.1 \cdot 10^{15}$	$5.4 \cdot 10^5$	$4.9 \cdot 10^{-10}$

Table 2-2. Published SAR and calculated equivalent ILP.

The same values presented in **Table 2-2** are also reported in **Figure 2-6** for a more descriptive, figurative comparison. Evaluation of particle quality based on *ILP* leads, in some cases (e.g. samples 15, 23), to a totally different estimation of its thermal efficiency, if compared to the corresponding *SAR*. As matter of fact, in the overall view samples potentially underestimated are actually strongly penalized by low power fields used during the investigation. The bars in **Figure 2-6** suggest that the same nanoconstructs would behave comparable to the best performing results reported in literature, if operated in similar conditions.

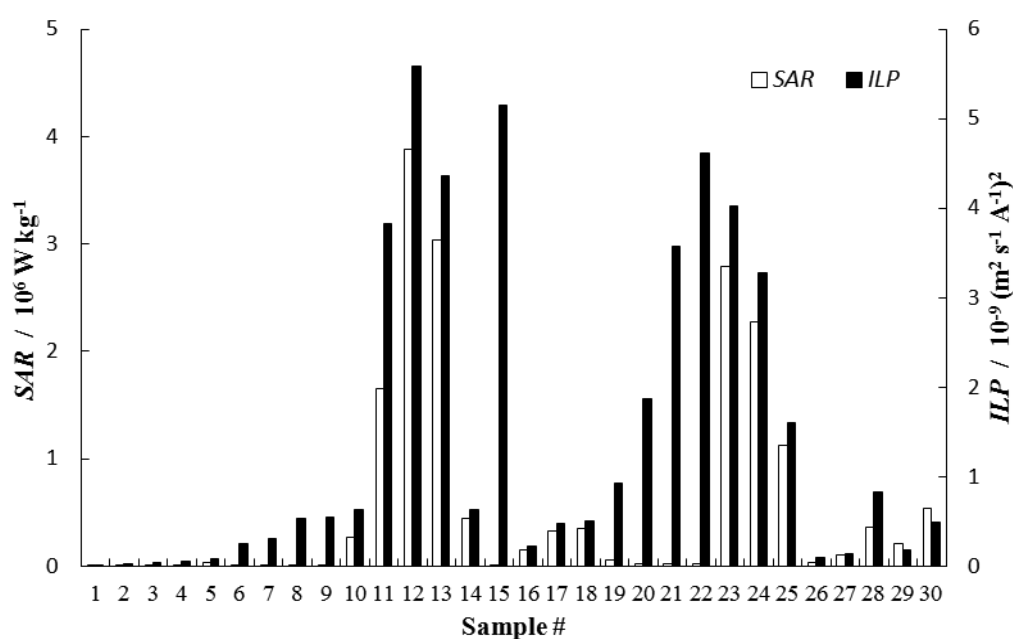


Figure 2-6. Comparison Specific Absorption Rate (*SAR*) vs. corresponding Intrinsic Loss Power (*ILP*).

Based on the linear dependency of *SAR* on the product $H_0^2 \cdot f$, the corresponding *ILP* is calculated and compared for different results in literature. The *ILP* provide and index to quantitatively evaluate the heating potential of a nanoparticle formulation independently from the incident magnetic field.

This decoupling between particle capabilities and field power is most convenient because it allows for separated designs of the applied field and the nanoparticle formulations. As for the applied field, since it is disconnected by the heating efficiency of the particles, it can be devoted to separate needs, as patient safety or integration with different applications; both these aspects are further discussed in **Chapter. 3** and **Chapter. 4**, respectively. As for the design of a most suited nanoconstruct, they should instead be taken in account the magnetic properties and the size. Again, following the work of Rosensweig, the magnetic properties of particles, are totally characterized by the anisotropy constant K , and magnetization saturation M_s ; (**Equations (2-8)**, **(2-10)**, **(2-11)**, and **(2-13)**). It can also be noted that the role of these two parameters are independent. Significant research in this direction has been published by Cheon and co-workers [62]. The contributions of the suspending media and the hydrodynamic volume of the nanoconstruct are instead accounted for in calculation of relaxation times. **Figure 2-7** reports examples of calculated ILP over a wide range of diameter, K , and M_s but fixed magnetic field. An optimal particle size for each operating frequency f can be identified that would maximize SAR , as shown in **Figure 2-7A** for $f = 500$ kHz and $H_0 = 10$ kA m⁻¹. The two contributions of Brownian and Neel relaxation are also clearly presented. This is addressed in the plots of **Figure 2-7B** and **C**, respectively and demonstrates that the maximum ILP grows as the anisotropy constant decreases and the magnetization saturation increases. Moreover, experiments have demonstrated that the heating efficiency of magnetic

nanoparticles can be enhanced by proper design of their surfaces [62, 83],
shape and composition selection [62, 63].

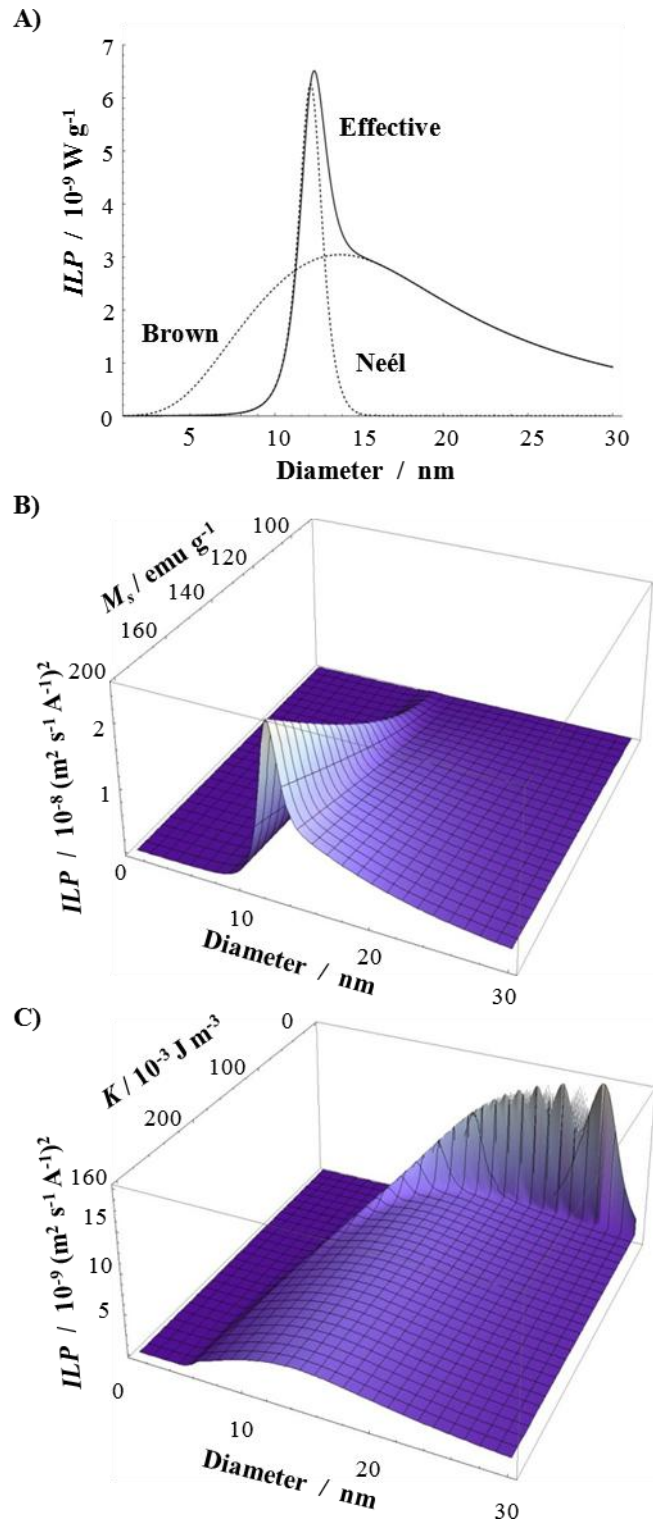


Figure 2-7. *ILP* dependence on saturation magnetization M_s and anisotropy constant K for $f = 500 \text{ kHz}$, $H_0 = 10 \text{ kA m}^{-1}$.

Simulations on *ILP* dependence on the main parameters characterizing a superparamagnetic particle: (A) Neél / Brown relaxation times, (B) M_s ; (C) K .

3. Design maps for local hyperthermia and ablation therapy

The hyperthermic treatment of a malignant tissue is based on the application of sufficiently high heat doses over time to induce cell death or cell sensitization [84, 85]. Most of the *in-vitro* studies based on nanoparticle (NP) for hyperthermic application are focused on maximizing the specific absorption rate (*SAR*), an index commonly used as sole parameter to quantify and compare the particle efficiency in converting electromagnetic energy into heat [51, 52, 76, 77, 80, 86, 87]. However, as extensively documented in section 2.5, *SAR* is not an intrinsic property of the NPs. As a result, very different *SAR* values have been published, ranging from 10^3 to 10^6 W kg⁻¹, depending on the operating conditions ($H_0 = 1 - 100$ kA m⁻¹ and $f = 100$ kHz – 50 MHz). On the other hand, *in-vivo* studies mostly investigate tumor regression over time, upon single or multiple hyperthermic treatments [88-90]. The tumor regression, similar to the *SAR*, is able to show the efficiency of a specific treatment but has little use as general comparative parameter. This creates confusion amongst the scientific community making the development of an efficient treatment more difficult.

In conclusion, the question about what indications to follow on the design of efficient thermal therapies still remains unanswered. An efficient design should require: more comprehensive indexes that correctly evaluates the nanoplatforms employed in relation to the applied field; synergistic potential

with coadjuvant treatments; unwanted effects; and can be tailored to take into considerations the eventual tumor- and/or patient-specific variability.

This third chapter deals with the systematic analyses of key factors for rational design of an efficient thermal therapy. *In-vitro* experiments and *in-silico* simulations were conducted in order to generate a proper comparative model and design guideline. The effects on the particles and tumor final temperature were estimated: for particle size, their concentration and magnetic properties; for the conditions of applied magnetic field; and for blood perfusion level. The contribution of non-specific heating over the specific iron oxide-induced heating is systematically analyzed at high- and low-frequency fields in reproducing physiologically relevant conditions. Clinically relevant strategies for improving the delivery of NPs within the tumor mass are then briefly discussed.

Although several types of magnetic NPs have been proposed, magnetite (Fe_3O_4) is the most extensively tested material in clinically relevant settings, demonstrating favorable biocompatibility and biodegradability [91, 92]. Protocols are available for large scale production of biocompatible magnetite NPs and for their surface modification. For these reasons, Fe_3O_4 nanoparticles are the sole superparamagnetic iron oxides (SPIOs) considered in this work.

3.1. SPIOs: characterization and processing

Commercially available SPIOs

Several colloidal formulations of Magnetite (Fe_3O_4) iron oxides (IOs) are commercially available. For these studies, we purchased particles with a nominal magnetic core diameter of 5, 10, and 14 nm from Sigma-Aldrich (5 and 10 nm) and Genovis AB (14 nm). A thin PEG (polyethylene glycol) layer coats these nanoparticles and provides sufficient hydrophilicity. Samples provided by the manufactures needed purification process to remove aggregates and then the iron concentration was also measured.

Sample purification

Through a cycle of sonications, centrifugation, collection of supernatant and pellet re-dilution, the sample can be efficiently divided between two colloidal solutions with two different aggregation levels. Consequential cycles performed on each produce a numbers of differently purified samples. The final procedure was defined comparing DLS measurements of about 8 samples, till the two results from each cycle returned similar values. In summary, the samples underwent sonication for 15 min and then centrifuged for about 6 minutes at 12,000 rpm ($14,000 \text{ g}^{-1}$); the supernatant is collected, sonicated for 7 more minutes, and centrifuged one more time. The resulting supernatant is collected and used during experiments.

Iron digestion and concentration measurement

The Fe concentration of every sample used is measured by ICP-OES (Inductively Coupled Plasma Optical Emission Spectrometer) analysis. This

system requires particles to be totally digested in ions before reading. Efficient digestion methods, one for hydrophobic and one for hydrophilic solvent, have been identified by comparing a positive control of known particle synthesized and provided by our collaborator at RICE University of Houston, Texas. Hydrophilic formulations of SPIOs are digested by diluting a known volume in 400 μl of HNO_3 and heated up to 140 $^\circ\text{C}$ on a hot plate till the solution is dried; then additional 400 μl of H_2O_2 is added to the vial and allowed to evaporate to dryness. The second cycle was performed by addition of in HNO_3 and lastly followed by addition of freshly prepared aqua regia. Finally, the digested sample is diluted in 5 ml of HNO_3 at 2% and processed. Hydrophobic samples are digested using a similar procedure. To avoid binding of iron oxide NPs to silicon oxides of glass vial, a 100 μl of acetonitrile was used to pre-wash the vial. Digestions and ICP measurements are always performed at least in triplicates plus a digestion control. Calibration curve is built with 0, 0.05, 0.5, 5, and 50 ppm points, by consecutive dilution of commercial available metal standards.

Electron microscopy imaging

Two magnetization systems are used for imaging at the micro- and nano-scale. (i) A scanning electron microscope (SEM) - FEI Nova Nano- SEM 230 - permits ultra-high resolution imaging (down to tens of nm) at high and low vacuum in presence of non-conducting and contaminating materials. Samples for SEM are prepared by dropping a small suspension of nanoparticle (~2 μl) onto a polished silicon wafer and then dried at room temperature. After drying, high temperature sensitive particles, as the polymeric-based

nanoparticles, are coated with 5-10 nm of platinum by electro sputtering, Cressington 208HR, before imaging. (ii) A transmission electron microscope (TEM, JEM-2100F, JEOL Ltd) also provides an insight into the inner structural composition where its resolution reach below sub-nanometric ranges. In brief, samples were prepared upon deposition onto the surface of a TEM grid (Ted Pella, Inc., Form var/Carbon 400 mesh, Copper, approx. grid hole size: 42 μ m) and left to dry for ~1 hr. Physico-chemical characterization of SPIOs including TEM micrographs of the three commercial SPIO preparations are presented in **Figure 3-1A, C, and E**. From analyses of these images and over 100 nanoparticles, the average size of SPIO cores were measured to be 5.13 ± 1.07 nm (nominal size: 5 nm); 7.18 ± 1.08 nm (nominal size: 10 nm) and 13.86 ± 1.48 nm (nominal size: 14 nm). The core size distribution is shown in the bar chart of **Figure 3-1B, D, and F**.

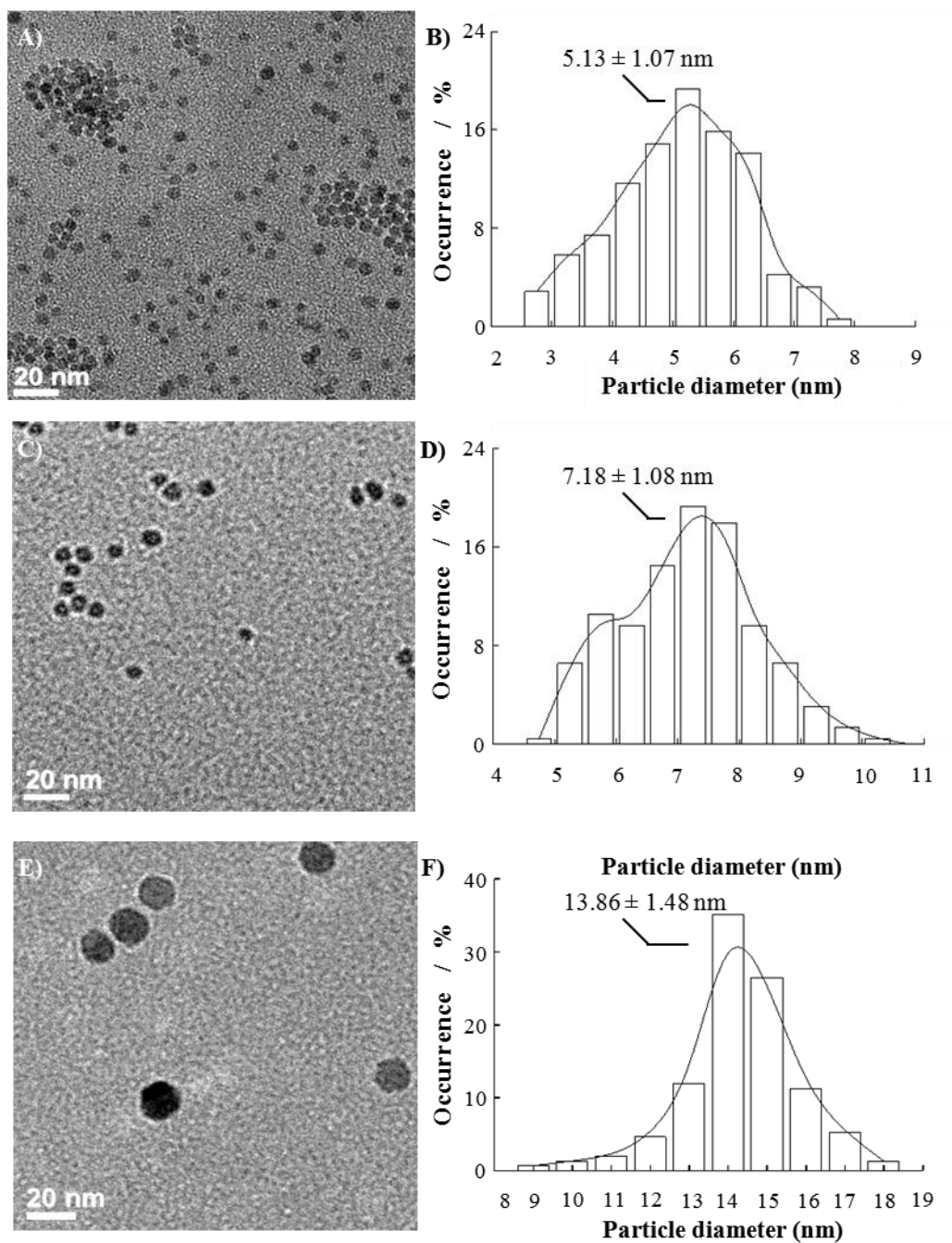


Figure 3-1. Physico characterization of the SPIO formulations.

(A, C, E) TEM images of the three SPIO formulations. Magnetic core size distribution as quantified from the TEM images reports sizes of (B) 5.13 ± 1.07 nm, (D) 7.18 ± 1.08 nm, and (F) 13.86 ± 1.48 nm

Laser scattering based characterizations

A dynamic light scattering (DLS) system - Zetasizer Nano ZS, Malvern Instruments Ltd – was used to measure hydrodynamic size of different populations in a colloidal suspension, and their polydispersity index (*PDI*); the same instrument uses electrophoretic light scattering to calculate zeta-potential of the particles in solution, their electrophoretic mobility, and the electrical susceptibility of the whole. Sample solution, possibly diluted in DI water, was poured in disposable capillary cells provided by the same manufactures. Triplicate of 16-runs measurements were averaged for each characterization. For zeta-potential measurements, 3 minutes of delay were observed between repetitions, due to residual excitation effects.

Magnetization characterization

The magnetic properties of nanoparticles were investigated thanks to a superconducting quantum interference device (SQUID) – MPMS-XL by Quantum Design Inc. DC magnetic measurement was performed at 300K in 0 - 50 Oe field. Magnetization and hysteresis curve were collected in the -5 T to 5 T range starting at zero field at 300K. The sample was prepared by dropping at least 300 μ l of nanocrystal suspensions at 3000 ppm Fe in an NMR tube. The NMR tube was sealed under vacuum and placed into a plastic straw for measurements. Data in **Figure 3-2** show no appreciable hysteresis (see insets), confirming the superparamagnetic behavior of the nanoparticles. For the 5 and 14 nm SPIOs, large magnetic saturations were measured with $M_s \sim 65$ and 82 emu g^{-1} , respectively; whilst far less performing were the 7 nm particles with an $M_s \sim 10 \text{ emu g}^{-1}$.

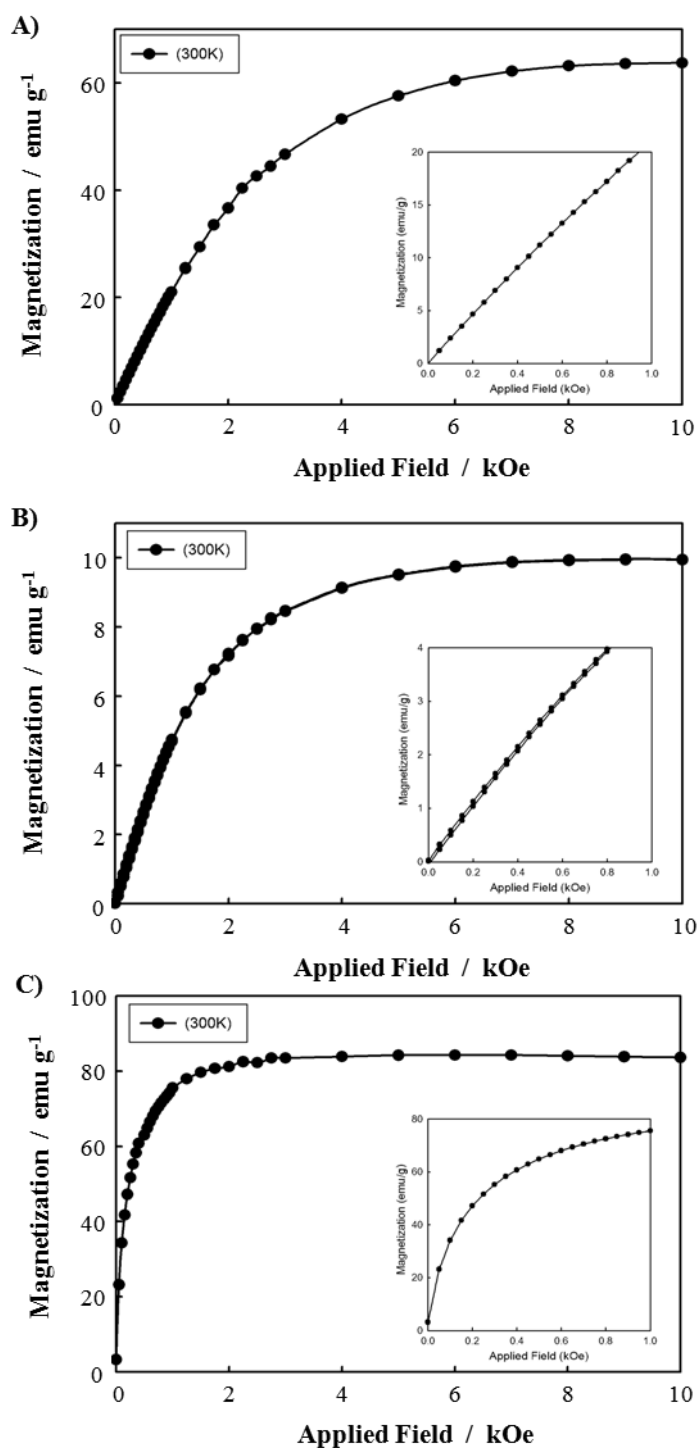


Figure 3-2. SQUID measurements of 5, 10, and 14 nm Iron Oxides (IOs).

SQUID measurements confirm superparamagnetic behavior for the particles employed in the study. Reported saturation magnetizations are: **(A)** 62 emu g⁻¹ for 5 nm particles; **(B)** 10 emu g⁻¹ for 10 nm particles; and **(C)** 82 emu g⁻¹ for the 14 nm particles

3.2. Apparata for magnetic hyperthermia and ablation therapy

A total of three apparata were used during electro heating experiments, able to generate alternated magnetic fields (AMFs) at *i*) high frequency, *ii*) low frequency, and *iii*) high power. The former was developed in the laboratory of Prof. Jarek Wosik, in collaboration with the Texas Center for Superconductivity, in Houston. The last two systems were assembled within the laboratory of Prof. Audrius Brazdeikis, at the same facility. It follows a basic description of these apparata.

3.2.1. High frequency field apparatus (>10 MHz)

This system was built to generate AMF fields in the MHz range, between 10 and 55 MHz, and with field strength up to 4 kA m^{-1} . A frequency synthesizer along with an amplifier is used to drive input power into a LCR resonator. Here, an exciting ring and a resonator coil become critically coupled at an impedance matching of $50 \text{ } \Omega$. An RF magnetic field is established inside the coil at the resonant frequency. The field so generated in the solenoid of the resonator is measured using a small loop sensor. The resonant circuit shows a Q-factor of ~ 110 , allowing a relatively low input power towards a significant amplification of the signal. This particular setup considers for temperature stabilization issues, significantly lowering the needs for cooling systems since most of the energy is dissipated in the resonator and not in the whole system. The resonator solenoid is made of six turns copper

tube (3 mm outer diameter) wound into a coil; this possesses a diameter of 15 mm, a length of 21 mm and a distance per turn of 0.1 mm. Due to the importance of a thermally isolated system, a single crystal sapphire (length 22 mm, width 12 mm, and height 45 mm) water-cooled is housed inside the solenoid and works as a heat sink. This design allows for *in-vitro* tests in a cylindrical quartz tube (inner diameter 2.5 mm, outer diameter 3 mm, height 20 mm) that hosts 180 μ l of sample and is mounted in a cylindrical hole drilled in a sapphire plate within the solenoid. A fiber optic GaAs temperature sensor (T1, Neoptix, Inc.) connected to a multichannel signal conditioner (Reflex, Neoptix, Inc.) measures sample temperature every 1 s using. The position of the sensor end is controlled by micrometer positioner to be at the geometrical center of the fluid. The system is illustrated in **Figure 3-3**.

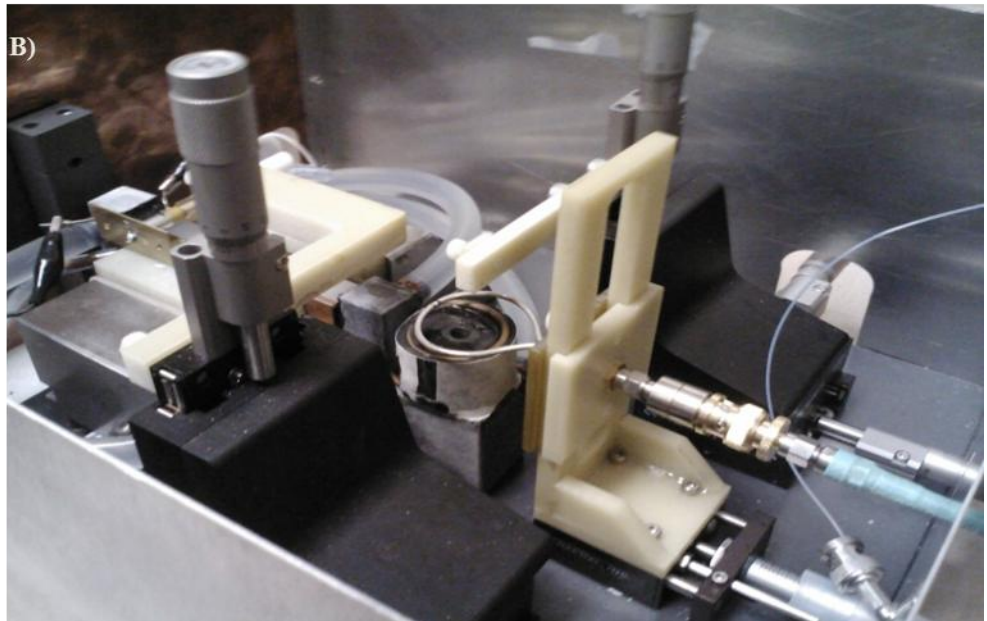
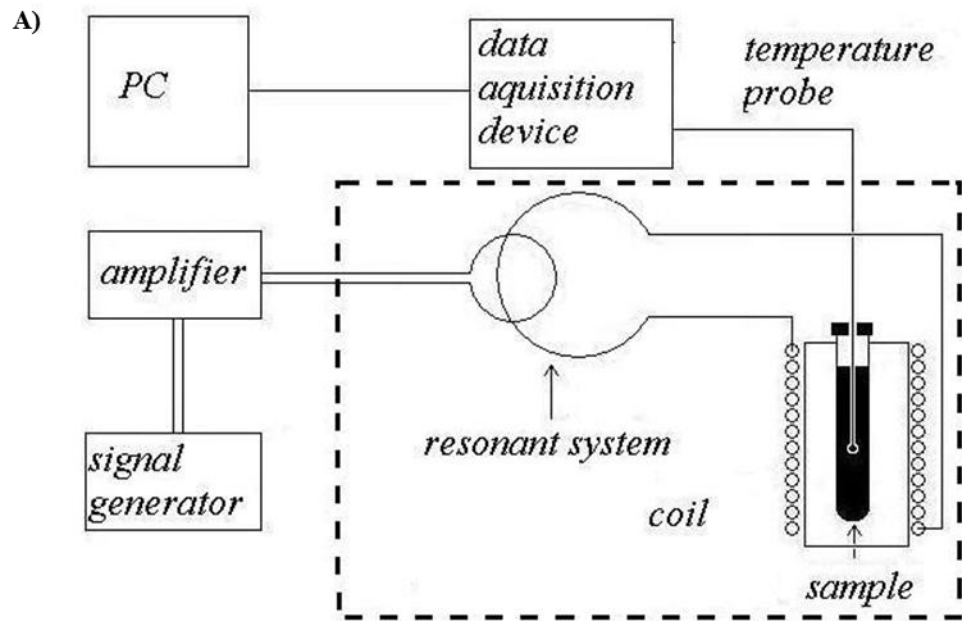


Figure 3-3. High frequency apparatus.

(A) Sketch of the high frequency apparatus circuit, consisting in a frequency synthesizer and an amplifier which feed a LCR resonator. The sample temperature is recorded thanks to an optic probe. (B) The exciting ring is critically coupled at with the resonator coil at an impedance matching of 50Ω ; the deployed magnetic field has frequency between 10 and 55 MHz, and field strength up to 4 kA m^{-1}

3.2.2. Low frequency field apparatus (≤ 1 MHz)

The second apparatus, in **Figure 3-4**, is able to produce AMFs in a discrete range of frequencies between 100 kHz and 1 MHz; the strength of the field can be up to 10 kA m^{-1} . The field coil is an element in a resonant RLC circuit with capacitance varying between 7 and 200 nF, and inductance varying in the range 4.5 - 9.1 μH , depending on the frequency. The coil quality Q-factor is about 250. High quality RF capacitors and high purity copper coil are used in the system to minimize heat dissipation and enhance Q. The resonant frequency of the system can be changed by replacing the capacitor and/or coil. The field coil temperature is stabilized at 20 ± 0.1 °C by a thermoelectric water cooler/heater (ThermoCube 400, Solid State Cooling Systems Inc.). This setup is designed to host *in-vitro* test with cells. In this case, temperature is monitored by a nIR thermocamera (A325, FLIR System, Inc.) placed above the coil. For heating tests of fluids, it possible to insert a cylindrical Plexiglas connected to a separate thermoelectric water cooler/heater (T251P-2, ThermoTec, Inc.), which maintains an equilibrium temperature of the inner holder at 19.8 ± 0.1 °C. In this case, a glass cylindrical tube (inner diameter 5 mm and length 35 mm) holds ~600 μl of sample solution and is precisely mounted at the center of the field coil; temperature is measured with the same probe described above.

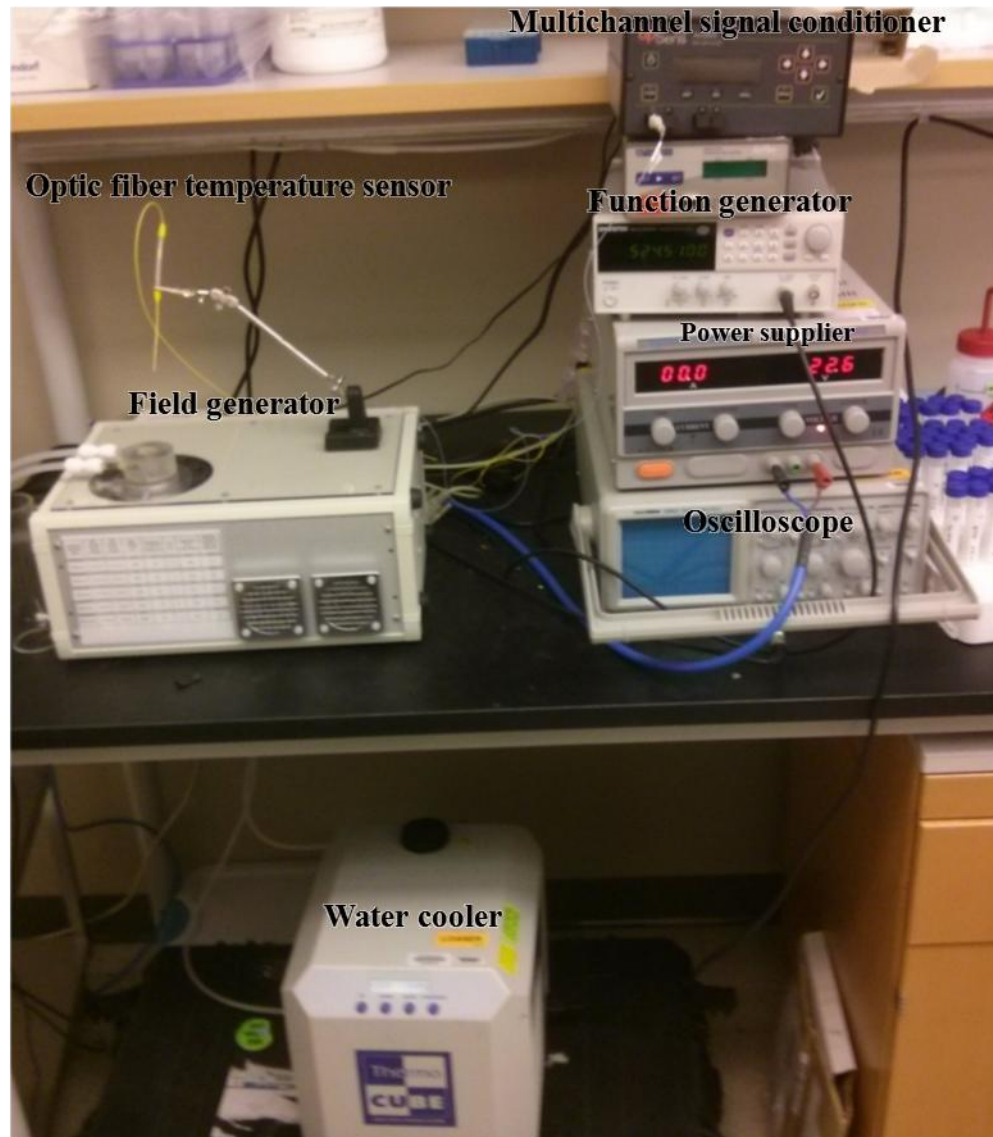


Figure 3-4. Low frequency apparatus.

The field generator receives input from the function generator and the power supplier. The temperature of the circuit and the surrounding area of the sample are controlled with a thermoelectric water cooler/heater ($T = 18\text{ }^{\circ}\text{C}$). An oscilloscope is used to monitor the field generated field. Sample temperature is recorded by and optic probe immersed to its center. The field generated is able to produce AMFs in a discrete range of frequencies between 100 kHz and 1 MHz; the strength of the field can be up to 10 kA m^{-1} .

3.2.3. High power system apparatus (≤ 1 MHz and up to 40 kA m^{-1})

The high power system (**Figure 3-5**) consists in an upgraded low frequency apparatus. The magnetic coil can deploy fields up to 50 kA m^{-1} at a resonance frequency of ~ 300 kHz. Briefly, a function generator (33120A, Agilent Tech.) is connected to a high power RF generator (800A3A, AR Inc.), which feed the RLC circuit; the later consists of a 200 nF condenser couple to an inductance of $1.45 \mu\text{H}$, which consists of a 7 turns, high grade copper coil, 3 cm wide and 4 cm tall; quality Q-factor is ~ 100 . The circuit temperature is kept in the $19 - 25$ °C range by a thermoelectric water cooler/heater (RC7BD, Thermotec Inc.). The generated field is constantly monitored by a multimeter (DMM2001, Kheytlhey) and an oscilloscope (TDS 3012, Tektronix). The system is designed for small animal experiments, and the same nIR camera previously described is used to record the temperature.

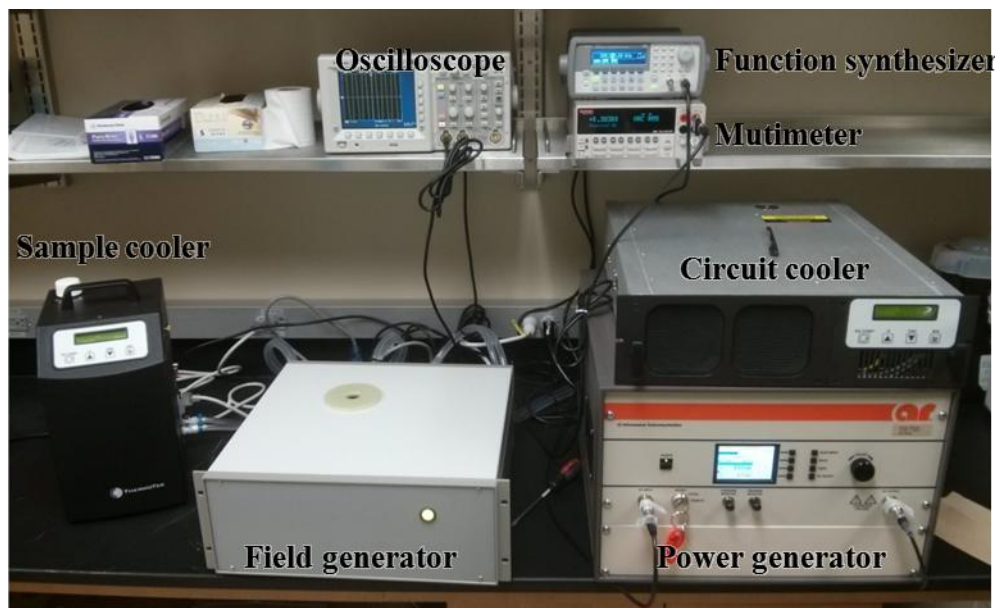


Figure 3-5. High power apparatus.

The function synthesizer feeds an 800W RF power generator which in turn provides the input for the field generator. Two chillers refrigerate the circuit ($T = 25\text{ }^{\circ}\text{C}$) and the sample holder ($T = 18\text{ }^{\circ}\text{C}$), separately. The generated field is monitored by an oscilloscope and a multimeter; the sample temperature is recorded using a nIR camera. This system can generate a field up to 50 kA m^{-1} and a frequency $\sim 300\text{ kHz}$

3.2.4. Homogeneity of the magnetic field

In order to assess the homogeneity of the magnetic field, which can highly affect heating performance, 5 drops ($\sim 6 \mu\text{l}$) of highly concentrated SPIO solution, are deposited in 5 different spots within the magnetic coil. The drops were equally spaced and deposited radially on a petri dish, placed within the spires of the solenoid. Diameter of the drop is $\sim 3 \text{ mm}$, spaced between each other of $\sim 1 \text{ mm}$ (**Figure 3-6A** and **B**). During the field exposure, temperature maps is acquired with the IR camera above reported, and the 5 different spots temperature $T(t)$ is continuously monitored (**Figure 3-6C**). Testing for statistical significance, it results that there is no statistically significant difference ($p \gg 0.05$) between the temperatures of the 3 most inner drops, for $t \leq 50 \text{ s}$. As described in details in paragraph 2.3 the heating property of nanoparticles exposed to excitation is commonly quantified by the SAR, which is directly proportional to the temperature evolution first derivative in $t = 0$ (**Equation (2-33)**). Percentage variation within the 6 %, and no statistical difference of SAR for these 3 drops (923, 1003 and 1022 W kg^{-1}) confirms a confident valuation of homogeneous field deployed within $\sim 10 \text{ mm}$ from the center of the coil (see Table in **Figure 3-6**). Vial used in fluid experiments regularly fall in this range; care is taken during cells and *in-vivo* experiments in order to remain within the confirmed area.

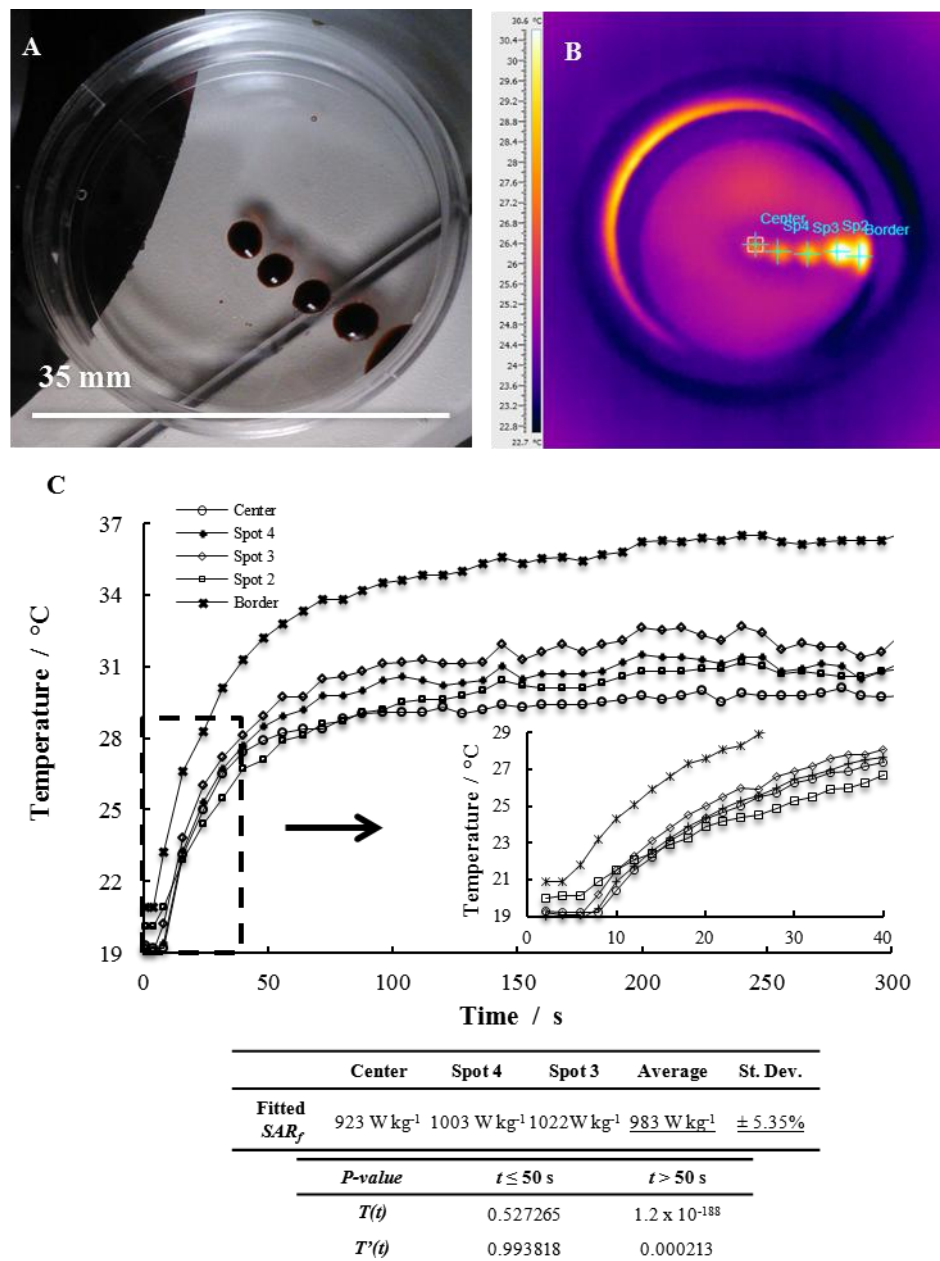


Figure 3-6. Homogeneity verification of the deployed field.

(A) Five drops of nanoparticle fluids are posed radially inside the magnetic coil and (B) the temperature recorded using a thermocamera. (C) The temperature profiles are plotted versus the time and show a negligible variation in temperature (except for the drop next to the coil). The inset show detail on the first seconds of heating; the difference between the first derivative of the inner 3 spots (within ~10 mm radius) is below the 6 %.

3.3. Results

3.3.1. SAR experimental setup

5, 10, and 14 nm SPIOs commercially available formulations were purified as described above. The resulting purified sample (1x) was diluted in DI water to obtain 0.1x, 0.3x, 0.5x, and 0.7 x concentrations. Electro-heating experiments were then conducted under 4 different field conditions: *i*) ~30 MHz and 4 kA m⁻¹; *ii*) ~1 MHz and 5 kA m⁻¹; *iii*) 500 kHz and 10 kA m⁻¹; *iv*) ~200 kHz and 9 kA m⁻¹. Exposure time was 12 min for (*i*), and 20 min for the others setups. Preceding every experiment, samples were sonicated for 2 minutes to dissolve any possible aggregate and to homogenize the solutions. At least six repetitions were performed per group. Before each single experiment the probe end was cleaned with isopropanol, and DI water was used to re-check calibration of the apparatus at intervals of about six experiments. The outcome of each experiment is the temperature - time curve $T(t)$ from which the maximum rise in temperature ΔT and the SAR_f of the solution can be readily extracted. The specific SAR of the particles at test was extrapolated following the calculations in following paragraph 3.3.2.

3.3.2. Correct computing of the specific absorption rate

Correct quantification of the SAR from experimental data was investigated comparing and averaging results from two procedures.

Fitting method

Temperature variation $T(t)$ with time was fitted over the whole duration of the exposure (**Figure 3-7A** and **C**) and used to calculate the derivative $T'(t)$ at time $t = 0$ s; then, SAR_{fit} is obtained based on **Equation (2-35)**. Results from all *in-vitro* experiments with colloidal fluids were processed using *Mathematica* software to interpolate measured data points with **Equation (2-31)**.

Differential method

At the same time, for each measurement, few experimental points next to the origin ($t = 0$ s) were considered to estimate the time derivative $T'(0)$, exploiting the very mathematical definitions of first order derivative and differential quotient:

$$T'(t) = \frac{dT(t)}{dt} = \lim_{\Delta t \rightarrow 0} \frac{T(t + \Delta t) - T(t)}{\Delta t} \quad [\text{K}] \quad (3-1)$$

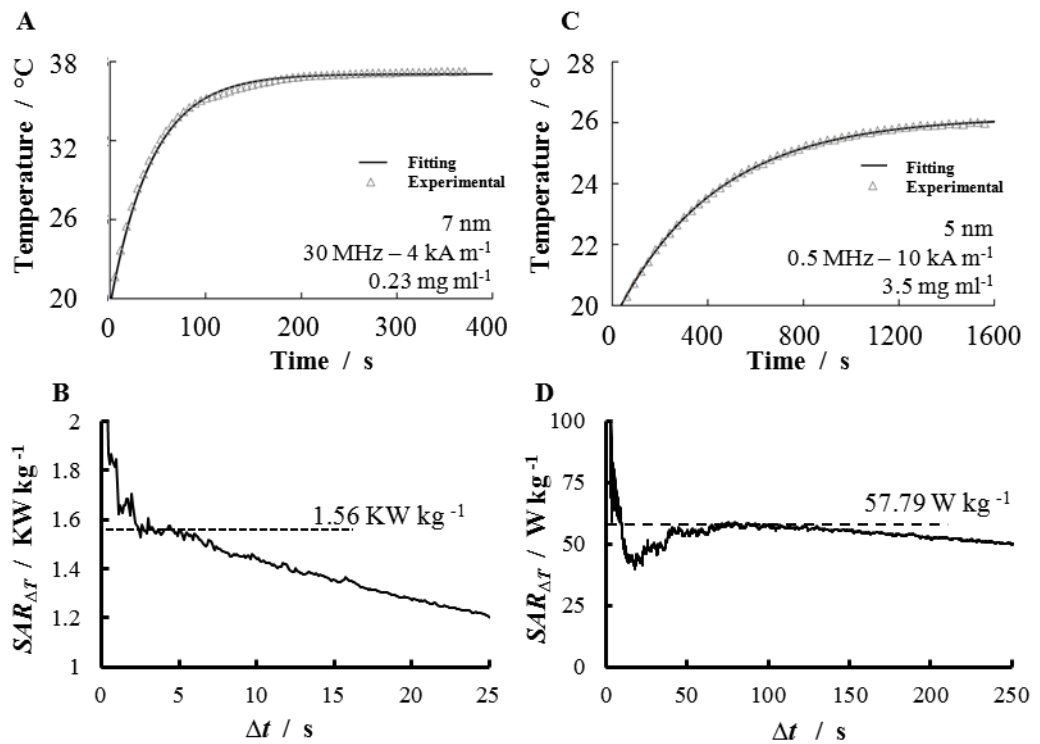
Then, initial temperature rate (and related SAR) was estimated as a function of the time interval Δt based on the formula

$$SAR_{\Delta t} = \frac{T(0 + \Delta t) - T(0)}{\Delta t} \cdot \frac{c_p}{m_{NP}} \quad [\text{W kg}^{-1}] \quad (3-2)$$

The choice of the correct time interval must be based on the linearity of the time derivative, as for the considerations in section 2.3.1. It proceeds as following. As Δt reduces from large values, $SAR_{\Delta t}$ progressively increases till it reaches plateau and its dependence from Δt is negligible. At further smaller time intervals, $SAR_{\Delta t}$ begins changing erratically and tends to rapidly increase as Δt approaches zero. On the other side, for time intervals Δt increasing

beyond the temperature $T(0+\Delta t)$ is approached with no more significant variation in the increment $T(0+\Delta t) - T(0)$. The proper time interval Δt over which $SAR_{\Delta t}$ is constant highly depends on the experimental conditions **(Figure 3-7B and D)**.

The percentage difference between SAR values computed via the differential and interpolating methods is typically within 5 %, but it can reach ~10 % if the measurement is not accurate.



Case	SAR Fitting	Δt	SAR Differential	Difference
A-B	1608.99 W kg ⁻¹	2 ÷ 4 sec	1561.34 ± 21.8 W kg ⁻¹	3 %
C-D	65.65 W kg ⁻¹	70 ÷ 90 sec	57.79 ± 0.6 W kg ⁻¹	12 %

Figure 3-7. Comparisons between computational SAR methods.

The two modes to calculate particles SAR are compared for 2 IOs formulations: (A,B) 7 nm Magnetite in 30 MHz / 4 kA m⁻¹ field and 0.23 mg ml⁻¹ concentration; and (C,D) 5 nm in 0.5 MHz / 10 kA m⁻¹ at 3.5 mg ml⁻¹. SAR_{fit} computed by fitting the temperature profile are calculated as (A) 1608.99 W kg⁻¹, and (C) 65.65 W kg⁻¹; SAR_{Δt} calculated on the Δt increment are (B) 1561.34 W kg⁻¹ and (D) 57.79 W kg⁻¹. The differences between the 2 calculation approaches are 3 % and 12 % for the 7 nm particles and the 5 nm one, respectively.

3.3.3. Hyperthermic performance at high frequency field

Using the high-frequency field apparatus described in section 3.2, the hyperthermic properties of the SPIOs were characterized under different conditions at 30 MHz (RF regime). Results are presented in **Figure 3-8**, for the 5 and 7 nm SPIOs. The total temperature variation ΔT , fluid SAR_f and nanoparticles SAR for the 5 and 7 nm SPIOs are plotted against the iron concentration in **Figure 3-8A, B and C**, respectively. A temperature increase of 15-20 °C was observed over a wide range of nanoparticle concentrations, namely varying from 0.022 to 0.33 mg ml⁻¹. The 7 nm particles heated up the solution slightly more than the 5 nm particles, but the difference is not statistically significant. Even more intriguing are the values derived for SAR_f and SAR . A biphasic behavior is observed for the SAR_f with a maximum occurring at about 0.1 mg ml⁻¹ (**Figure 3-8B**). On the other hand, the SAR decreases continuously as the nanoparticle concentration increases from 0.022 to 0.33 mg ml⁻¹. No statistically significant difference is observed between the 5 and 7 nm SPIOs, for both measured SAR .

Based on the definitions of SAR and following the current literature [76, 77, 79, 82, 93], these results are intriguing in that it was expected *i*) a fixed SAR independent from the iron concentration; *ii*) a steady growing ΔT and SAR_f with the iron concentration; *iii*) statistically significance difference in ΔT and SAR between the 5 and 7 nm particles, which have very different magnetic properties (see **Figure 3-2B and C**).

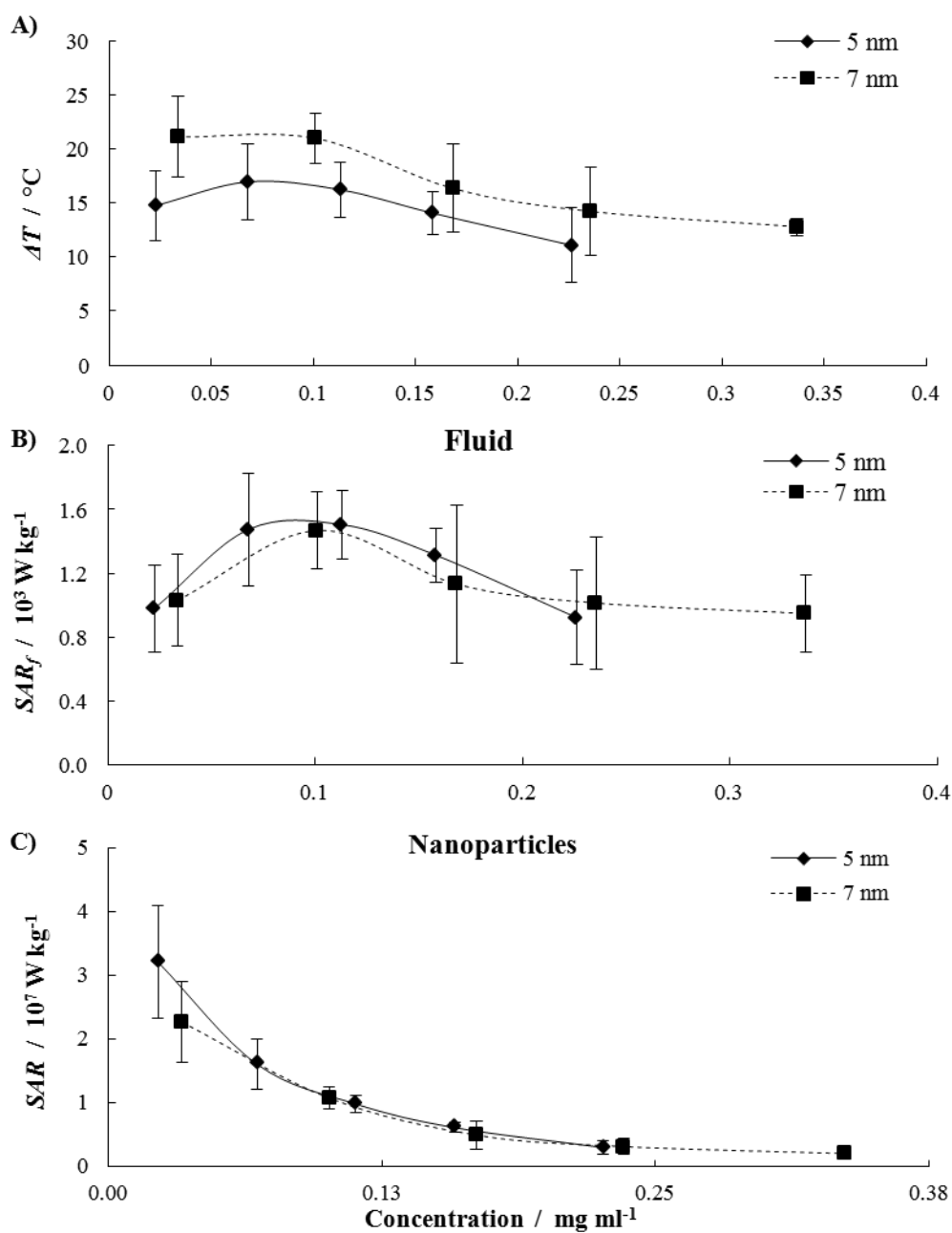


Figure 3-8. Hyperthermic performance at high frequency field (30 MHz). (A) Absolute temperature increase; (B) ΔT specific absorption rate of the solution (SAR_f); and (C) specific absorption rate of the magnetic nanoparticles (SAR) as a function of the iron concentrations in solution, for the 5 and 7 nm SPIOs (30 MHz and 4 kA m^{-1}). The biphasic behavior can be noted for ΔT and SAR_f . No significant difference can be appreciated for 5 and 7 nm SAR , both decreasing with the increase of Fe concentration.

3.3.4. *Non-specific heating at high frequency field*

Puzzled by the results shown in **Figure 3-8**, the ΔT and SAR_f values for a pure solution of NaCl are measured and compared to those registered for the SPIOs. Results are presented in **Figure 3-9**. Different concentrations of NaCl were considered, namely ranging from 0 (pure, DI water) to 300 mM (supra-physiological salt concentrations). The electrical conductivity of the solutions was also measured by electrophoretic light scattering. As expected, **Figure 3-9A** shows a linear increase in the electrical conductivity of the NaCl solution with the salt concentration.

The ΔT and SAR_f for the NaCl solutions at different salinities were measured using the same approach described above for the SPIOs. This is shown in **Figure 3-9B** and **Figure 3-9C** (dot-dashed line with cross) as a function of the electrical conductivity of the solution, rather than the salt concentration. Knowing that non-specific heating in the RF regime can be associated with ions dispersed in solutions [79], the electrical conductivity was also measured for the 5 and 7 nm SPIO solutions. Then, the data from **Figure 3-8A** and **B** were rephrased in terms of the electrical conductivity of the solution rather than its iron concentration. Thus, **Figure 3-9B** and **3C** show the ΔT and SAR_f variation over the electrical conductivity of the solutions with NaCl (dot-dashed line with cross), 5 nm SPIOs (solid line with diamond) and 7 nm SPIOs (dashed line with square).

The trends and absolute values for the three sets of data are very similar with almost no statistically significant difference within the range 0.05 to 1.89 S m⁻¹. The intriguing biphasic behavior noted above for the SPIOs

(Figure 3-8B, C) is here observed also for the free NaCl solution, implying that it might be related to non-specific rather than IOs specific heating. NaCl SAR profile is in agreement with the behavior reported by Beković and Hamler in [79]; in their study they infused solution enriched in NaCl within the malignant tissue prior exposure to RF fields. Also, a statistically significant difference between the SPIOs and the NaCl solutions is only observed for larger electrical conductivities, namely $> 1.5 \text{ S m}^{-1}$. Note that a physiological solution (150 mM of NaCl) exhibits an electrical conductivity of 1.8 S m^{-1} . For $\sim 300 \text{ mM}$ of NaCl, the electrical conductivity is 3.6 S m^{-1} .

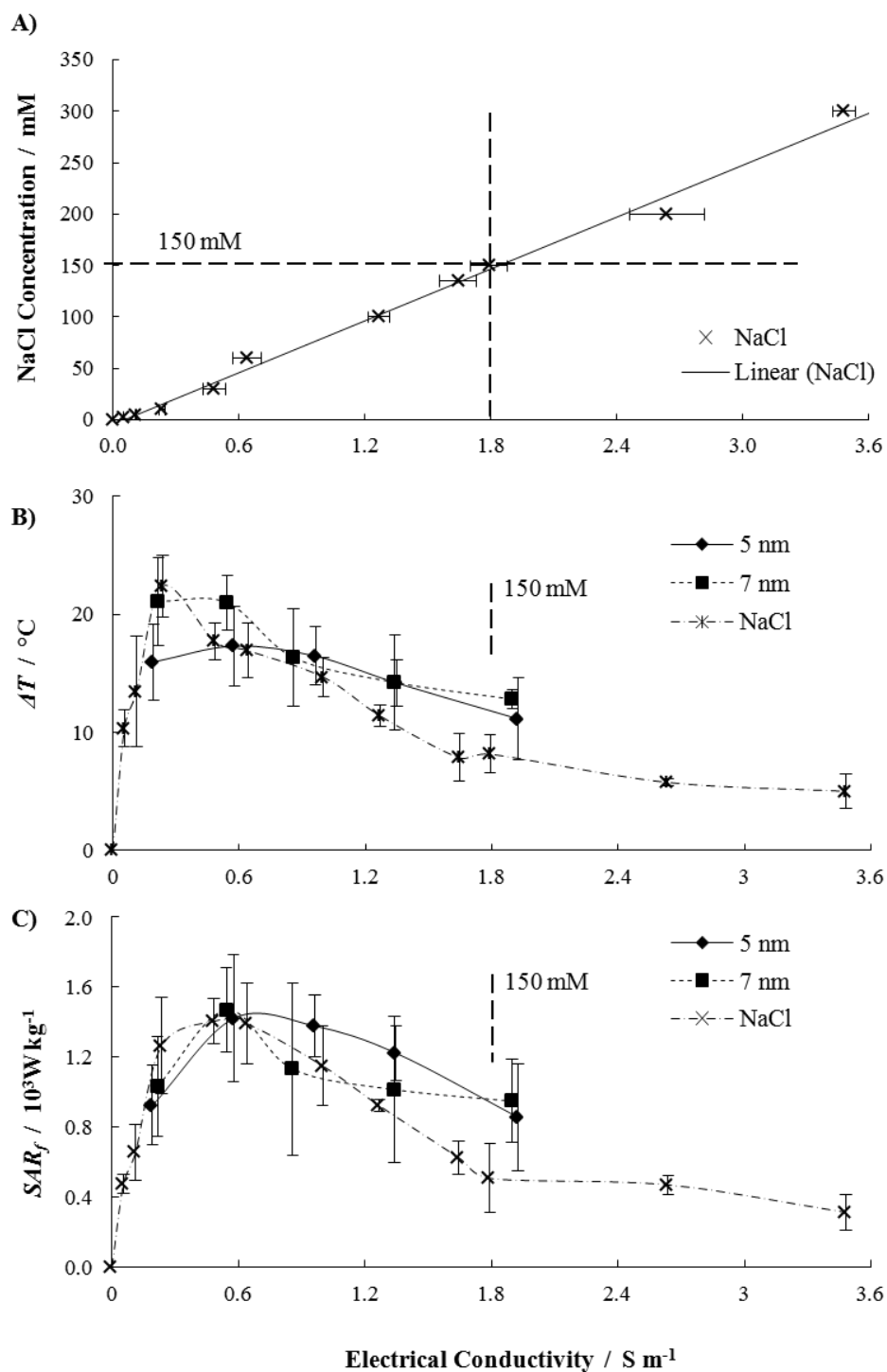
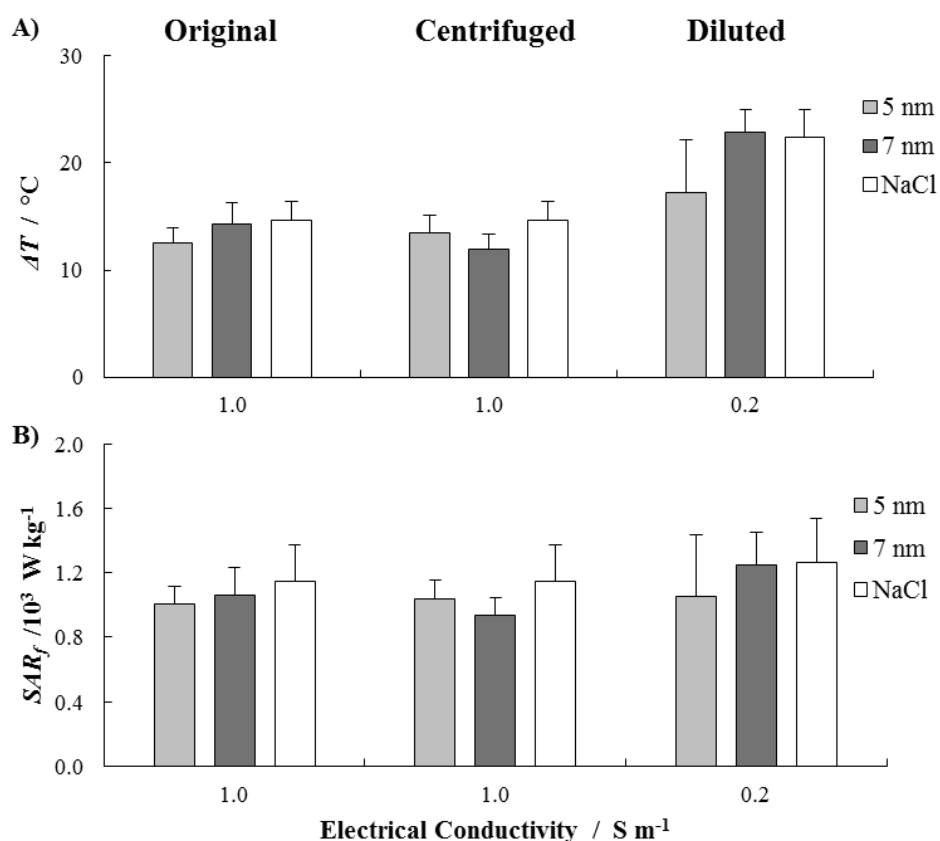


Figure 3-9. Non-specific heating at high frequency field (30 MHz).

(A) Linear relationship between NaCl concentration of water solution and its electrical conductivity. (B) Absolute temperature increase ΔT and (C) fluid specific absorption rate SAR_f as a function of the electrical conductivity for 5, 7 nm SPIOs and saline solutions (30 MHz and 4 kA m⁻¹).

These differences are analyzed in more details in the bar charts of **Figure 3-10** and **Figure 3-11**. The first shows the non-specific nature of the heating by presenting the ΔT and SAR_f for diluted and centrifuged colloidal solutions. Here the behavior of two particle formulations (5 and 7 nm SPIOs) is considered and compared with NaCl solutions. In particular, the original samples, provided by the vendor in a concentration of about 1.0 mg ml^{-1} and with an electrical conductivity of 1 S m^{-1} , were centrifuged. The collected supernatant was then exposed to AMF (centrifuged samples).

Although, the concentration of iron in the centrifuged solution is lower than in the original sample (see table in **Figure 3-10**), no statistically significant difference is observed for ΔT and SAR_f . Indeed, centrifugation process does not alter the ionic concentration and the electrical conductivities remain the same. Then, original samples were diluted about five times in DI water, thus reducing both the iron and ionic concentration; consequently, the electrical conductivity is decreased to about 0.2 S m^{-1} (diluted sample), closer to the SAR_f peak for salt solution (**Figure 3-9B, C**). In this case, a slight variation (increasing) in ΔT and SAR_f is observed as compared to the original sample.

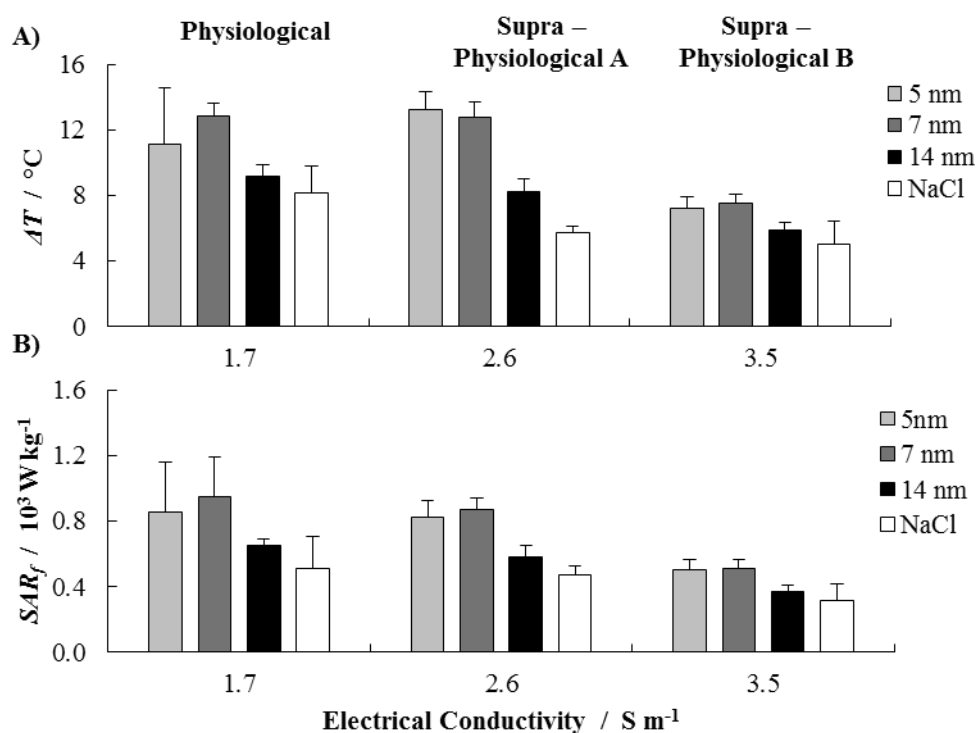


	Sample	El. Conductivity	Concentration
Original	5 nm	1 S m ⁻¹	1.02 mg ml ⁻¹
	10 nm	0.98 S m ⁻¹	1.04 mg ml ⁻¹
	NaCl	1 S m ⁻¹	80 mM
Centrifuged	5 nm	0.99 S m ⁻¹	0.99 mg ml ⁻¹
	10 nm	0.98 S m ⁻¹	0.71 mg ml ⁻¹
	NaCl	1 S m ⁻¹	80 mM
Diluted	5 nm	0.18 S m ⁻¹	0.13 mg ml ⁻¹
	10 nm	0.18 S m ⁻¹	0.09 mg ml ⁻¹
	NaCl	0.23 S m ⁻¹	10 mM

Figure 3-10. Comparison of non-specific heating at high frequency field.

Total temperature variation ΔT (A) and SAR_f (B) of 5 and 7 nm SPIO formulation with NaCl solutions. For each sample the comparison is between: *i*) the original sample; *ii*) the supernatant obtained after centrifugation; and *iii*) a further re-dilution in DI water. The table lists all Fe concentrations and electrical conductivities.

The bar chart of **Figure 3-11** shows the variation of ΔT and SAR_f for three different salt concentrations, namely 135 (physiological), 210 and 300 mM (supra-physiological), and the considered three SPIO preparations. A minimal difference between the 5 and 7 nm SPIOs and the NaCl solution is observed under these conditions, with a SAR_f for the formers being 2-fold than the latter (~ 900 and 450 W kg^{-1}). No significant difference was observed even for the 14 nm SPIOs. These results confirms that in the physiological and supra-physiological regime, the 5 and 7 nm SPIOs heat up the solution with SAR_f that are larger than the NaCl solution alone, but the contribution of non-specific heating is comparable with the heat generated by the magnetic nanoparticles.



	Sample	El. Conductivity	Concentration
Physiological	5 nm	1.67 S m^{-1}	0.22 mg ml^{-1}
	7 nm	1.72 S m^{-1}	0.33 mg ml^{-1}
	14 nm	1.66 S m^{-1}	1.095 mg ml^{-1}
	NaCl	1.65 S m^{-1}	135 mM
Supra-Physiological A	5 nm	2.77 S m^{-1}	0.99 mg ml^{-1}
	7 nm	2.63 S m^{-1}	0.71 mg ml^{-1}
	14 nm	2.42 S m^{-1}	0.89 mg ml^{-1}
	NaCl	2.63 S m^{-1}	210 mM
Supra-Physiological B	5 nm	3.7 S m^{-1}	0.99 mg ml^{-1}
	7 nm	3.48 S m^{-1}	0.71 mg ml^{-1}
	14 nm	3.5 S m^{-1}	1.28 mg ml^{-1}
	NaCl	3.48 S m^{-1}	300 mM

Figure 3-11. Mild heating of SPIOs at high frequency field (30 MHz).

(A) The absolute temperature increase ΔT and (B) SAR_f of 5, 7, 14 nm SPIO and NaCl solutions. The comparison is between the same samples at 1.7, 2.6, and 3.5 S m^{-1} . The table lists the exact values of electrical conductivity and Fe concentrations for the tested sample solutions (30 MHz and 4 kA m^{-1}).

3.3.5. Hyperthermic performance at low frequency field

The hyperthermic properties of the SPIOs were also characterized at 200, 500 and 1,000 kHz using the second apparatus described section 3.2.2. The data are plotted in **Figure 3-12**. No appreciable heat is generated by NaCl solutions, even at physiologically relevant salt concentrations, for all frequencies tested. This confirms that for sufficiently low frequencies, non-specific heating is negligible. Next, the 5, 7, and 14 nm SPIOs were investigated under different conditions with a concentration of 0.4 mg ml⁻¹. However, both the 7 and 14 nm SPIOs did not exhibit any significant heating at these lower frequencies, possibly due to the insufficient magnetization of the first particle and large size of the second. The inferior performances of 14 nm particles can be attributed to their size and also to the surface coating of the particles [83].

The ΔT and SAR_f of the 5 nm SPIOs show a concentration and frequency dependent behavior, in agreement with the linear response theory [54]. **Figure 3-12** shows a linear behavior of ΔT and SAR_f with the Fe concentration, whereas the particle SAR is almost constant over the considered range of concentrations. Also in **Figure 3-12F**, comparing the cases of $f = 200$ and 500 kHz, it can be readily appreciated a SAR increase of 2.5 times (from 6,400 to 16,800 W kg⁻¹) consistent with the corresponding variation in f ($H \sim 10$ kA m⁻¹). Similar observations can be drawn for the other combinations of f and H .

In **Figure 3-12**, the results show that 5 nm SPIOs at a concentration of 5 mg ml⁻¹ would generate a temperature increase ΔT of about 10 °C after

exposure to a 500 kHz field with a strength of just 10 kA m^{-1} . These data demonstrate that at low frequencies ($< 1 \text{ MHz}$) non-specific heating is virtually absent and significant increments in temperature can be generated and sustained for long periods of times. Note however that the maximum temperature increase depends on the volume of solution and the environmental conditions (see section 2.2). Therefore, a feasibility analysis must also include the modeling of the heat generated from the metal nanoparticles, its transfer to the surrounding tissue, and corresponding temperature increase over time. The following paragraphs deal with these considerations, reporting the results obtained from finite elements simulations.

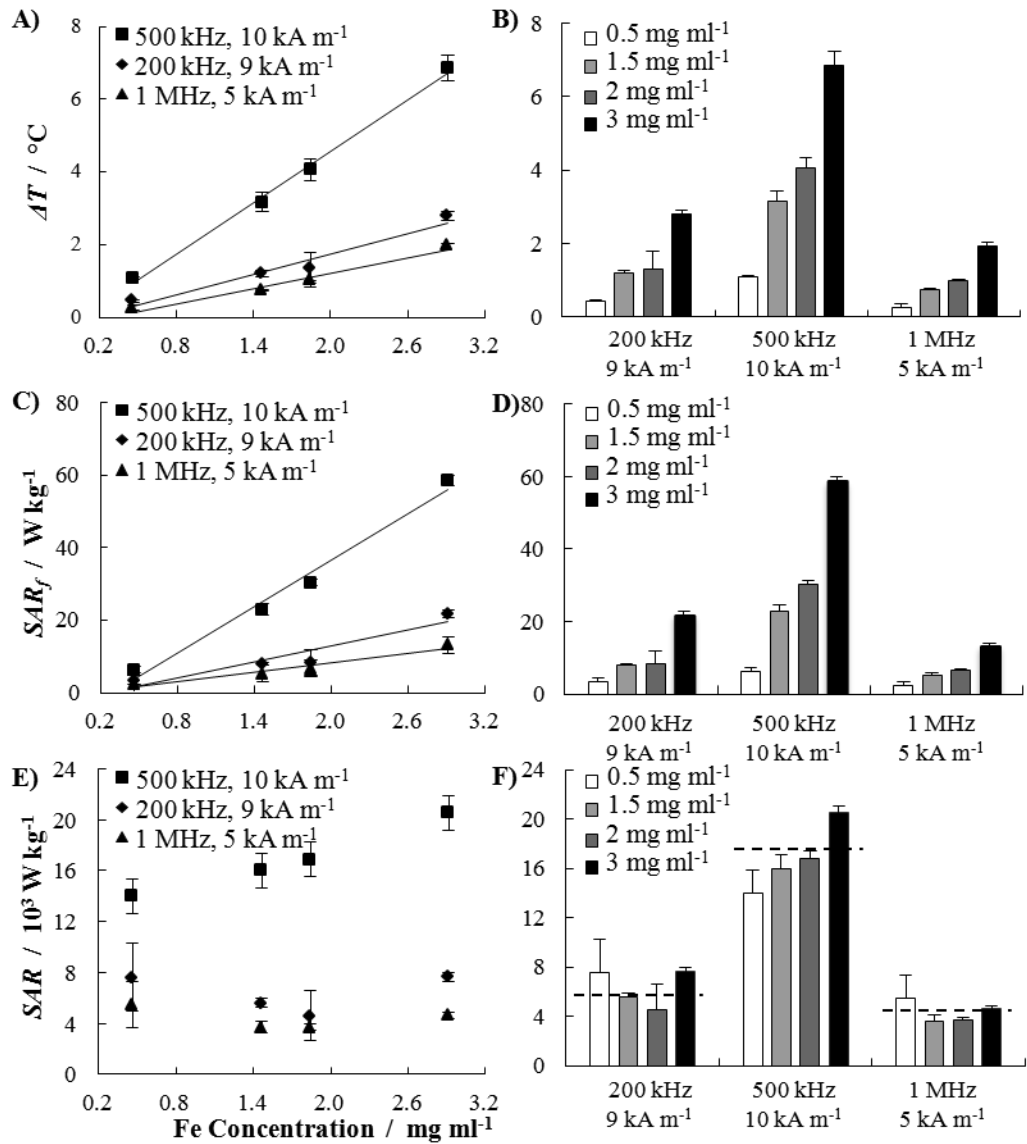


Figure 3-12. Hyperthermic performance at low frequency fields (0.2; 0.5; and 1 MHz).

(A, C, E) ΔT , SAR_f , and SAR as a function of the iron concentration under different AMF operating conditions (200 kHz and 9 kA m⁻¹; 500 kHz and 10 kA m⁻¹; and 1 MHz and 5 kA m⁻¹). (B, D, F) Same ΔT , SAR_f , and SAR for three different AMF operating conditions grouped by iron concentration. (0.5, 1.5, 2, and 3 mg ml⁻¹).

3.3.6. Computational modeling of the temperature field within the tissue

The temperature field is quantified using a finite element method, as described in the paragraph 2.4. A schematic representation of the computational domain is previously shown in **Figure 2-4**. Here Ω_1 is the healthy tissue surrounding the tumor located in Ω_2 , where the SPIOs are uniformly distributed. Per the performed experimental work, two conditions were modeled: high frequency with $f = 30$ MHz and low frequency with $f = 500$ KHz. In the first case, a nanoparticle concentration of 0.22 mg ml^{-1} was considered. Heating capacity are as for **Figure 3-11B**, assuming for the tissue SAR_t the same as found for physiological concentrations of salt solution ($SAR_t = 450 \text{ W kg}^{-1}$ for simple tissue in Ω_1 and $SAR_f = 900 \text{ W kg}^{-1}$ for tissue and IOs in Ω_2). The corresponding volumetric fraction ϕ was about 4.3×10^{-6} , thus it was reasonably assumed that the presence of the nanoparticles did not affect the physical properties of the tissue. The value for the heat exchange parameter h_v was derived by referring to the heating of a pure NaCl solution (**Figure 3-11A**). Considering a single domain with $w_{bl,1} = 0 \text{ s}^{-1}$ a heat exchange coefficient $h_v = 1.65 \times 10^{-3} \text{ W mm}^{-2} \text{ K}^{-1}$ reproduces the observed $8 \text{ }^\circ\text{C}$ increase in temperature for a NaCl solution with $SAR_{NaCl} = 450 \text{ W kg}^{-1}$. Note that this value of h_v is in agreement with data presented in literature [74]. All the parameters used in the simulations are listed in **Table 2-1**.

The temperature field was derived by solving **Equations** (2-36) and (2-37) for $T(\vec{x}, t)$, considering different values of $w_{bl,1}^0, w_{bl,2}^0 = 0 \text{ s}^{-1}$, with

boundary conditions (2-38), (2-39), (2-40) and initial condition (2-41). **Figure 3-13A** shows the temperature distribution within the computational domain at time $t = 600$ s, for $w_{bl,1}^0 = 0.018 \text{ s}^{-1}$. The upper portion of the panel gives the temperature field resulting from the heat generated by the SPIOs deposited in Ω_2 in addition to the non-specific heating; whereas the bottom portion of the panel shows the results corresponding to the sole non-specific heating. There is clearly an increase in temperature within the tumor domain (Ω_2) due to the presence of the SPIOs, however the temperature difference between the two conditions is only of about 3 °C, being the max temperatures equal to ~ 44 and ~ 41 °C, respectively (see **Figure 3-14A**, red lines). Also, the healthy tissue surrounding the tumor is exposed to significantly high heat doses with a minimum temperature of ~ 42 °C, deriving from the non-specific heating of the tissue as well as from the diffusion of heat from the tumor. **Figure 3-14A** shows the increase with time of the temperature in the center of the domain where the absolute maximum temperature was registered within the whole domain, for different perfusion levels of the healthy tissue. Note that within 200 s (~ 3 min), the system reached almost the steady state. In **Figure 3-13A**, the relevance of non-specific heating can be immediately deduced by comparing the data for the solid (specific heating) and dashed (non-specific heating) lines.

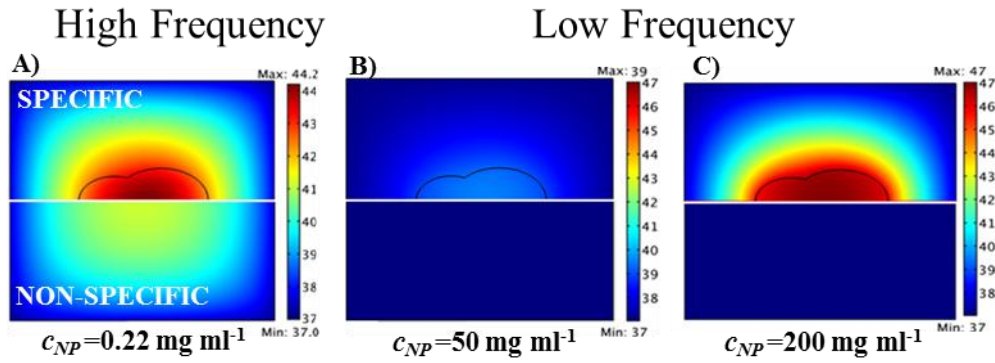


Figure 3-13. Computational modeling of the temperature field within a biological tissue.

Temperature field at equilibrium for a uniform distribution of SPIOs. (A) Simulation of high frequency (30 MHz) heating inside the tumor ($SAR_f = 900 \text{ W g}^{-1}$), and non-specific tissue heating in the outer region ($SAR_f = 450 \text{ W g}^{-1}$) (blood perfusion $w_{bl,I}^0 = 0.018 \text{ s}^{-1}$). (B, C) Low frequency (500 kHz) simulations of temperature field at equilibrium for a uniform distribution of SPIOs at two different concentrations (50 and 200 mg ml^{-1}). All the bottom half-panels refer to non-specific heating alone ($c_{NP} = 0$).

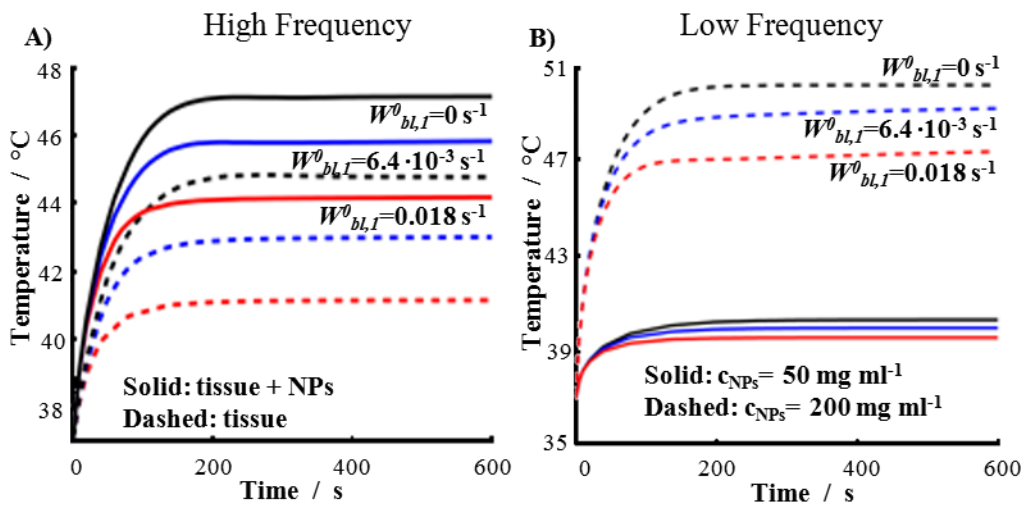


Figure 3-14. Temperature increase in the modelled areas.

Temperature increase with time in the tumor region for different blood perfusion levels of the surrounding, healthy tissue. (A) Solid lines refers to specific heating inside the tumor ($f = 30 \text{ MHz}$), and dashed lines refers to non-specific heating alone. (B) Solid lines and dashed lines refer to 50 and 200 mg ml^{-1} of SPIOs, respectively ($f = 500 \text{ kHz}$).

In the case of low frequency fields, the non-specific heating is negligible and heat is solely generated within the tumor domain Ω_2 where the SPIOs are deposited. Therefore, $SAR_t = 0 \text{ W kg}^{-1}$ everywhere within the computational domain. Considering the same geometry and parameters as for the high frequency case, the temperature field is provided in **Figure 3-13B** and **C** for two different SPIO concentrations, namely 50 mg ml^{-1} . The SAR used was extrapolated from experimental results presented in **Figure 3-12E, F** for the 5 nm SPIOs, assuming a linear increase of the specific absorption rate with the particle concentration. In the both bottom panels of **Figure 3-13B** and **C** no increase in temperature is observed (lack of non-specific heating); whereas, as expected, in the upper panels the temperature increases with the concentration of the SPIOs. At the highest concentration of 200 mg ml^{-1} , the maximum temperature of $\sim 47 \text{ }^\circ\text{C}$ is reached uniformly within the tumor domain Ω_2 . In this case, the temperature increase within the healthy tissue has to be ascribed solely to heat transport from the central tumor domain Ω_2 . **Figure 3-14B** shows the increase with time of the temperature in the center of the domain for different perfusion levels. Even in this case, steady state conditions were reached within almost 200 s ($\sim 3 \text{ min}$). Note that all these data correspond to the case in which no perfusion occurs within the tumor tissue, which indeed leads to slightly higher temperatures within the Ω_2 domain.

Using the same computational framework, a systematic analysis can be performed to quantify the equilibrium temperature under different conditions, and in particular for different values of the SPIO concentration c_{NP} and SAR .

This is shown in the bar chart of **Figure 3-15A**, which confirms a steady, linear increase in the maximum temperature achieved in the tumor tissue with c_{NP} and SAR . It is well accepted that tissue thermal ablation can be efficacious only by achieving temperatures equal or larger than 50 °C for sufficiently long periods of time. Mild ablation or hyperthermia can be achieved at temperatures equal or larger than 42 °C. Therefore, choosing these as target temperatures, two lines can be drawn in the c_{NP} - SAR plane as shown in **Figure 3-15B**.

These are quasi-linear lines in a double logarithmic plot for the range of concentrations and specific absorption rates considered, and are described by the equation

$$c_{NP} \times SAR^a \geq b \quad [\text{W m}^{-3}] \quad (3-3)$$

where $a = 1.0616$ and $b = 2.2714 \times 10^6 \text{ W m}^{-3}$ for $T = 42 \text{ °C}$; $a = 1.0737$ and $b = 7.1565 \times 10^6 \text{ W m}^{-3}$ for $T = 50 \text{ °C}$. Three characteristic operating regimes can be identified in **Figure 3-15B**: *i) insufficient heating* for c_{NP} - SAR values falling below the hyperthermia curve ($T_{eq} < 42 \text{ °C}$, green area); *ii) hyperthermia* for c_{NP} - SAR values falling between the hyperthermia and ablation curves ($42 \text{ °C} \leq T_{eq} < 50 \text{ °C}$, white area); and *iii) ablation* for c_{NP} - SAR values falling above the ablation curve ($T_{eq} \geq 50 \text{ °C}$, red area). **Figure 3-15B** provides a design map for rationally selecting the hyperthermic treatments and identifying the proper route of administration – systemic versus intratumor injection – depending on the magnetic and biodistribution properties of the nanoparticles. Note that this result is general in that it can be applied for any

nanoparticle, including ferromagnetic particles, for which the *SAR* and local tissue concentration are known.

It should here be emphasized that nanoparticles, especially if systemically injected, would not distribute uniformly within the target tissue. Their concentration is expected to be larger at sites with higher vascular permeability and blood perfusion; and this will vary within the tumor mass as well as with the type and stage of the disease. Nonetheless, the assumption of a uniform distribution of nanoparticles within the target tissue provides a conservative estimation on the maximum temperature that can be reached within the region of interest, for a given total number of particles.

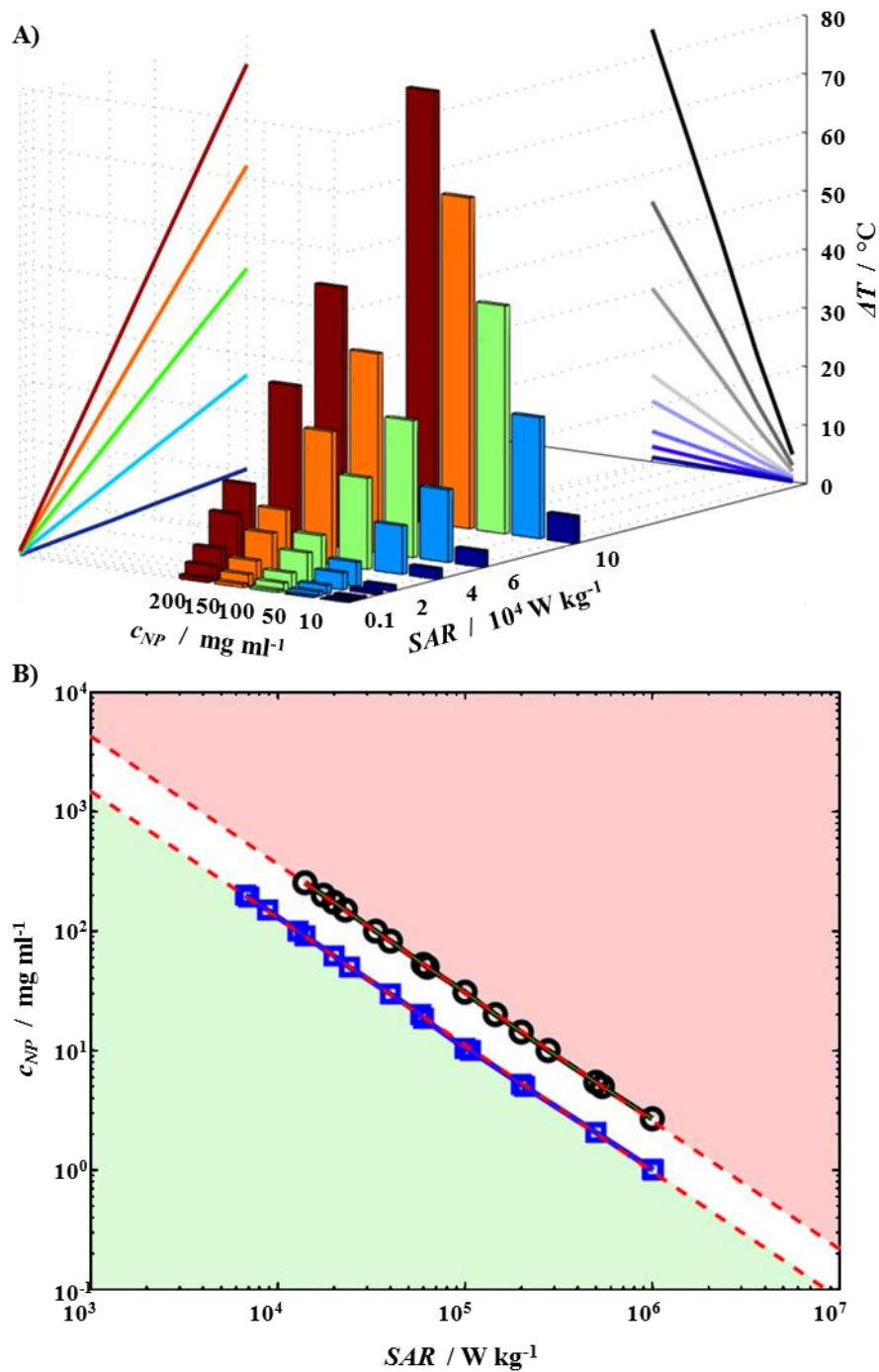


Figure 3-15. Design map for local hyperthermia and ablation therapy.

(A) Maximum absolute temperature reached in the tumor center for different nanoparticle concentrations, c_{NP} and specific absorption rates, SAR. (B) Isotherm lines for tissue hyperthermia ($T_{tissue} = 42^\circ\text{C}$) and thermal ablation ($T_{tissue} = 50^\circ\text{C}$) drawn as a function of the nanoparticle concentration c_{NP} and specific absorption rate SAR.

3.4. Discussion on the clinical feasibility of thermal therapies

The data presented in **Figure 3-15B** demonstrates that in order to achieve tissue hyperthermia and thermal ablation, sufficiently large values of *SAR* and SPIO concentrations are required. Therefore, it is here important to discuss strategies to improve the hyperthermic properties and tumor accumulation of magnetic nanoparticles.

Section 2.5 describes the dependence of the particle intrinsic loss power (*ILP*) from features such as the size, shape and surface properties of the SPIOs. Once the optimal nanoparticle properties are established, the *SAR* can be still tuned by controlling the operating conditions of the AMF apparatus (meaning frequency f and strength H_0) following the linear response theory. Theoretical and experimental works have confirmed that, within the AMF regime here of interest, the specific absorption rates would grow linearly with the frequency ($\propto f$) and with the second power of the AMF strength ($\propto H^2$). This is also confirmed here by the data presented in **Figure 3-12**. The 5 nm SPIOs used in the present work provides an *ILP* value of $\sim 382 \cdot 10^{-12} \text{ (m}^2 \text{ s}^{-1} \text{ A}^{-1})^2$. By increasing the field strength up to 50 kA m^{-1} , their *SAR* would grow up to $\sim 5 \cdot 10^5 \text{ W kg}^{-1}$, and the corresponding concentrations needed for hyperthermia and ablation therapy would be ~ 2 and 5.5 mg ml^{-1} , respectively, as from **Equation (3-3)**.

It is here important to recall the seminal work done by Atkinson and Brezovich on magnetic hyperthermia treatments and patient discomfort. In

particular, Atkinson and colleagues [94] proposed a maximum limit for the product $fH = 4.85 \times 10^8$ A turns m s^{-1} . This number was based on discomfort during measurements performed on patients over 20 years ago. In the same work, the authors have clearly reported that the maximum tolerable dose depends also on the equipment, duration, location and extension of the region of treatment; and on the specific patient. Therefore, the value $4.85 \cdot 10^8$ A turns m s^{-1} should be considered as an indication rather than an absolute strict limit.

The majority of the *in-vivo* experiments available in the literature have dealt with locally, intratumorally injected nanoparticles with concentrations ranging from a few mg ml^{-1} to a few hundreds of mg ml^{-1} . Therefore, the questions should be posed on whether sufficient concentrations of SPIOs for hyperthermia and thermal ablation could be achieved within a tumor mass via systemic injection. A very elegant study on the biodistribution of radio-labeled SPIOs have been published demonstrating tumor accumulation on the average of $\sim 1.0\%$ ID g^{-1} for up to 70 nm in size nanoparticles [95]. This level of tumor accumulation for systemically injected nanoparticles could be enhanced by following two strategies: *i*) encapsulating SPIOs into larger carriers that are rationally designed to lodge within the diseased vasculature of tumors [96, 97] and *ii*) magnetically dragging the SPIOs within the tumor mass using external forces, generated by static magnetic fields [98, 99]. In order to complete the investigation on the rational design of IOs-based nanodevices for hyperthermic treatments, both these approaches was also explored. Results are presented in the next **Chapter 4**.

An issue that can arise when performing experiments on mice is non-specific major uptake of SPIOs in other organs, such as the liver or spleen. Accumulation here can highly exceed the level of 1% ID g^{-1} found in the tumor, causing unwanted damage if the whole mouse body is exposed to AMFs. Nevertheless, in human application it is possible to localize the area of exposure with highly focused field, reducing the risk of unwanted damages. Cytotoxicity analysis conducted on SPIOs in mice, rats and humans had shown from mild to tolerable side effects up to concentrations of 4'000 mg Fe kg^{-1} [100, 101]. This would imply an injected dose of ~ 100 mg Fe for a 20 g mouse. Thus, considering of 1% ID g^{-1} tissue accumulation data given above, a total SPIO concentration within the tumor mass of ~ 1.0 mg Fe ml^{-1} would be expected (1 g \approx 1 ml of tissue). For these levels of tumor accumulation, hyperthermia and thermal ablation could solely be achieved via the systemic injection of SPIOs with a $SAR \sim 10^6 - 10^7$ W kg^{-1} . This would be only one order of magnitude larger than the values obtained here with commercially available 5 nm SPIOs stimulated at 500 kHz and 50 kA m^{-1} . Referring to the **Table 2-2**, the nanoparticles presented in [62] with a $SAR \sim 4 \times 10^6$ W kg^{-1} at 500 kHz and 37.3 kA m^{-1} could reach such high values by increasing the field strength to 50 kA m^{-1} ($\sim 7.2 \times 10^6$ W kg^{-1}) and the minimum concentrations required for hyperthermia and ablation would be of 0.1 and 0.3 mg ml^{-1} , respectively.

Based on the above reasoning, one would conclude that hyperthermia and thermal ablation of cancerous tissues are feasible with the systemic injection of magnetic nanoparticles for sufficiently high SAR values, as given by **Equation (3-3)**.

4. A novel class of magnetic nanoconstructs

Chapter. 4 expounds on the optimal design of a superparamagnetic iron oxides particles (SPIOs) based system, merging heating proprieties with other typical features of SPIOs.

The magnetic properties of SPIOs have been exploited for both imaging, diagnosis, and therapy in diverse biomedical applications [86, 102-104]. Indeed, SPIOs offer a significant shortening of the transverse relaxation time of water and can be efficiently used as T_2 -MRI contrast agents [105-107]; they are generally made of biodegradable iron that, upon dissolution, can enter the physiological metabolism of cells limiting possible concerns on toxicity [108-110]. Moreover, their surface can be chemically modified using a variety of well-established protocols to confer specific molecular and electrostatic properties [111, 112]. Finally, the intrinsic magnetic character allows for improved target accumulation through the use of directed magnetic gradient field [113, 114].

A plethora of work have been dedicated to develop SPIOs and SPIO-based systems, with enhanced MRI or thermal ablation performance. Nevertheless, it seems that no publications yet investigate the possibility to exploit more of these capacities at the same time. The potential of SPIOs to perform simultaneously much different functionalities strongly appeals to the idea of a more complete nanodevice for cancer treatments.

In order to modulate the magnetic properties of iron oxide NPs, several strategies were proposed in recent literature, as that of forming clusters of SPIOs [115, 116]. The mobility of the water molecules within and around the cluster is thereof altered and, depending on the SPIO spatial organization, the cluster can present higher transversal relaxivities r_2 as compared to the individual SPIO [117, 118]. Other investigator systematically had analyzed the effect of the size and surface properties of SPIOs in numerous manuscripts showing that transversal relaxivity can be boosted by increasing the metal core size up to ~ 30 nm [119, 120]; whereas the type and thickness of polymer coatings can be detrimental to r_2 in that it could negatively affect the diffusion of the water molecules and their interaction with the metal core [121]. Recently, the shape of the SPIOs has been also explored as a parameter for optimizing magnetic response. Needles, star-shaped and cubical particles have been reported by several groups. Among the different iron oxide particles (IOs) shapes, iron oxide nanocubes (NCs) demonstrated remarkable MRI and thermal ablation properties [63, 108, 122-126].

Following these leads, three different formulations of magnetic nanoconstructs were here generated by confining multiple, individual SPIOs into a polymeric matrix. The nanoconstructs were named: *i*) Hybrids NanoParticles (HNPs); *ii*) Discoidal Polymeric Nanoconstructs (DPNs); and *iii*) Magnetic NanoFlakes (MNFs). These were characterized for their physico-chemical properties, stability in solution over time, relaxometric and hyperthermic properties, cytotoxicity, and in flow magnetic targeting. The third formulation was especially defined as a multi-functional device able to

perform at the same time in all the above mentioned SPIOs features. Additionally, a preliminary *in-vivo* study confirms the hyperthermic potentiality of this last nanoconstruct.

4.1. Synthesis, physico-chemical characterization, and cell viability assessment of polymeric nanoconstructs

4.1.1. Particles synthesis

Synthesis for several particles formulation were approached with the assistance of different collaborators, starting with the basic SPIO nanoparticles, which are the focus of this Ph.D. work, and moving to more complex polymer-based structures.

Spherical and cubical IOs

With the help of Dr. Minjung Cho, spherical (several sizes from 5 up to 20 nm) and cubical (22 nm) IO nanoparticles were synthesized following the protocol in [127, 128].

The procedure for spherical IOs was the following: 0.178 g of FeO(OH), 2.26 g oleic acid (OA) and 5 g 1-ODE were mixed in a 100 ml three neck flask and heated to 120 °C for 2 hours to remove residual water and further heated to 240 °C for 30 minutes to synthesize iron carboxylate, iron-oleate; then, the reaction mixture was heated to 320 °C for 2 hours under N₂ condition; to purify the resulting black colloidal nanocrystals, 20 ml of

methanol and 20 ml acetone were added to 5 ml resulting colloidal solution and centrifuged at 4150 rpm for 30 minutes; the precipitates at the bottom were re-dispersed using hexanes and this process was repeated six times. Finally, 10 nm iron oxide nanocrystals were purified and dispersed in hexanes.

For 16 nm Fe₃O₄ nanocrystals, the molar ratio between FeO(OH) and oleic acid was changed from 1:3 to 1:5 with all other conditions remaining the same. To produce smaller IO nanocrystals (< 5 nm), iron oleate was used as the iron precursor. 4 nm IO nanocrystals were prepared using iron oleate (0.015 mM, 0.009 g) and oleic acid (0.3 mM, 0.08 g) in 5 g ODE at 320 °C for 3 hours under the N₂ flow. The largest iron oxide nanocrystals (33 nm), required a higher molar concentration of FeO(OH), oleic acid, and ODE. FeOOH (50 mM, 4.5 g), oleic acid (200 mM, 56 g), and 1-ODE (40 mM, 10 g) were first heated to 240 °C for 2 hours and further heated to 320 °C for 12 hours.

Synthesis of NC consisted in: 0.71g of iron (III) acetylacetonate, 1.27 g of oleic acid, 10.40g of benzyl ether, and 0.41g of 4-biphenylcarboxylic were mixed in a three neck flask, then degassed by nitrogen gas (1 hour) before reaction. The mixture was heated up to 290 °C and left to react for 30 minutes and then cooled down and the produced nanocubes could be precipitated by ethanol; a magnetic separator of Dexter Magnetic Technologies Inc. (Elk Grove Village, IL) is employed to remove supernatant; the purified nanocubes were resuspended in chloroform. Iron (III) acetylacetonate, 4-biphenylcarboxylic acid, and benzyl ether were purchased from Thermo Fisher

Scientific Inc. (Waltham, MA). Oleic acid is obtained from Sigma-Aldrich Corp (St. Louis, MO).

Both spherical and cubic IOs were finalized with a thin coating of oleic acid, performed as follows [129]: oleic acid (0.95 μM to 9.5 μM) was introduced to 1 ml of nanocrystals solution dispersed in ethyl ether (1,500 - 4,000 mg/l of iron concentration); after stirring the mixture for 24 hours, ultra-pure water (MILLIPORE, 18.2 M Ω) or 0.1 M sodium bicarbonate (*pH* 9) solution was introduced and stirred for an additional 2 hours; then the sample was probe sonicated (UP 50H, Dr. Hielscher) at 60 % amplitude for 10 minutes to help disperse the material in water. The nanocrystal solution was stirred, uncovered for 1 day to completely evaporate the residual organic solvents; the purification of water-soluble nanocrystals was carried out using ultracentrifugation (optima L-90K ultracentrifuge, Beckman coulter) at 40'000 rpm for 3 hours twice followed by syringe filtration (pore size of 0.45 μM , Whatman NYL); the resulting aqueous solutions were acquired after these ultracentrifugation and syringe filtration steps.

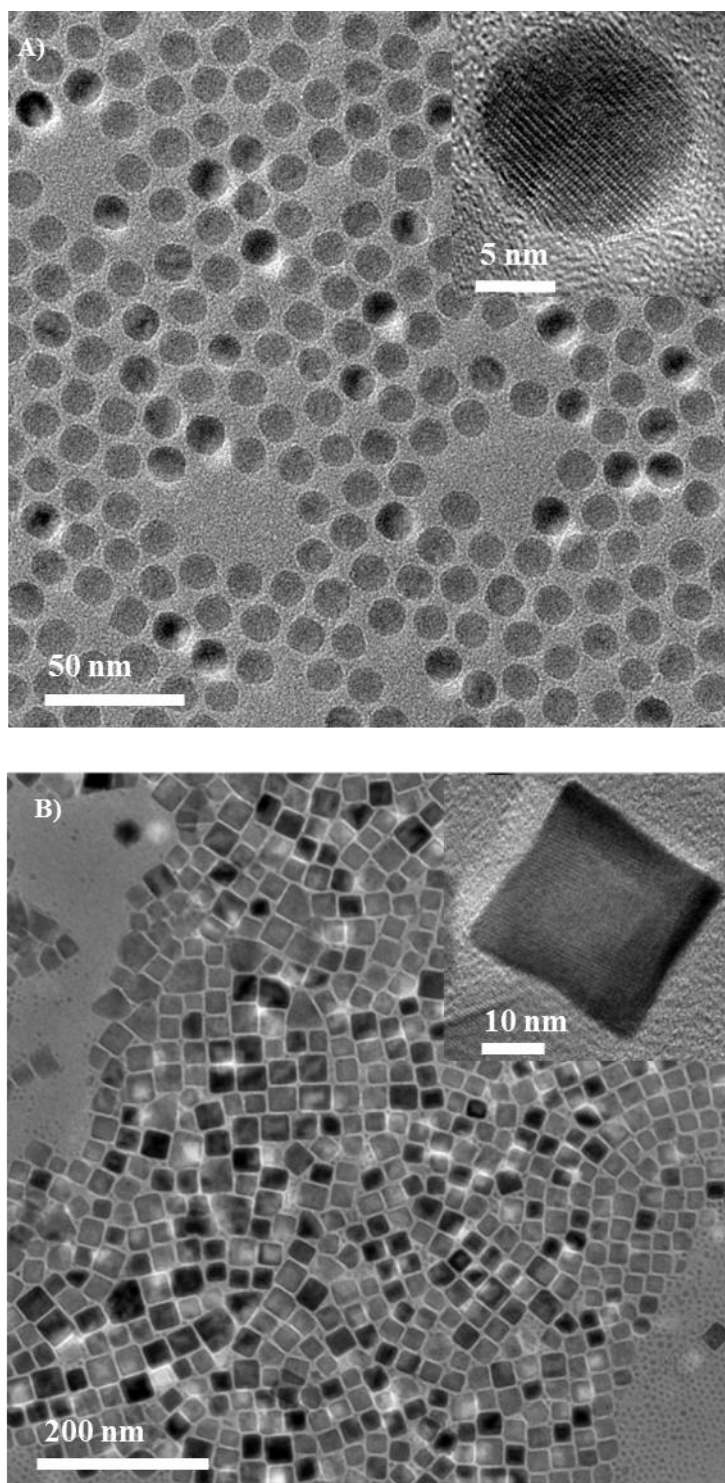


Figure 4-1. TEM Iron Oxides nanoparticles.

Transmission electron imaging of (A) freshly synthesized 11 nm spherical and (B) 22 nm cubical IOs. The insets show high resolution details. (From Dr. Minjung Cho.)

Polymeric hybrid particles

Assisted by Dr. Santosh Aryal, hybrid nanoparticles with a polymeric core of PLGA (poly(lactic acid-co-glycolic acid), Lactate Absorbable Polymers - DURECT Corporation) mixed with 17 nm sized spherical hydrophobic SPIOs and PEG-lipid shell were developed. Synthesis followed a single step nano-precipitation method: 200 µg of Egg PC (*L*-phosphatidylcholine, egg, chicken, Avanti Polar Lipid Inc.) and 260 µg DSPE-PEG-COOH (*1,2*-distearoyl-*sn*-glycero-3-phosphoethanolamine-*N*-carboxy-(polyethyleneglycol)-2000, Avanti Polar Lipid Inc.) were dissolved in 4% ethanol at 68 °C; to this solution, PLGA (1 mg, Mn ~50 kDa) and 0.1 mg of SPIOs dissolved in acetonitrile (Fisher Sci.) were added drop wise while heating and stirring. Then the vial was vortexed for 3 min followed by the addition of room temperature DI water (1 ml). The solution mixture was stirred at room temperature for 2 h, washed using an Amicon Ultra centrifugal filter (Millipore, Billerica, MA) with a molecular-weight cutoff of 100 kDa. Finally, the purified HNPs were collected in 1 ml water or phosphate buffer saline and stored at 4 °C. The procedure is reported in **Figure 4-2**.

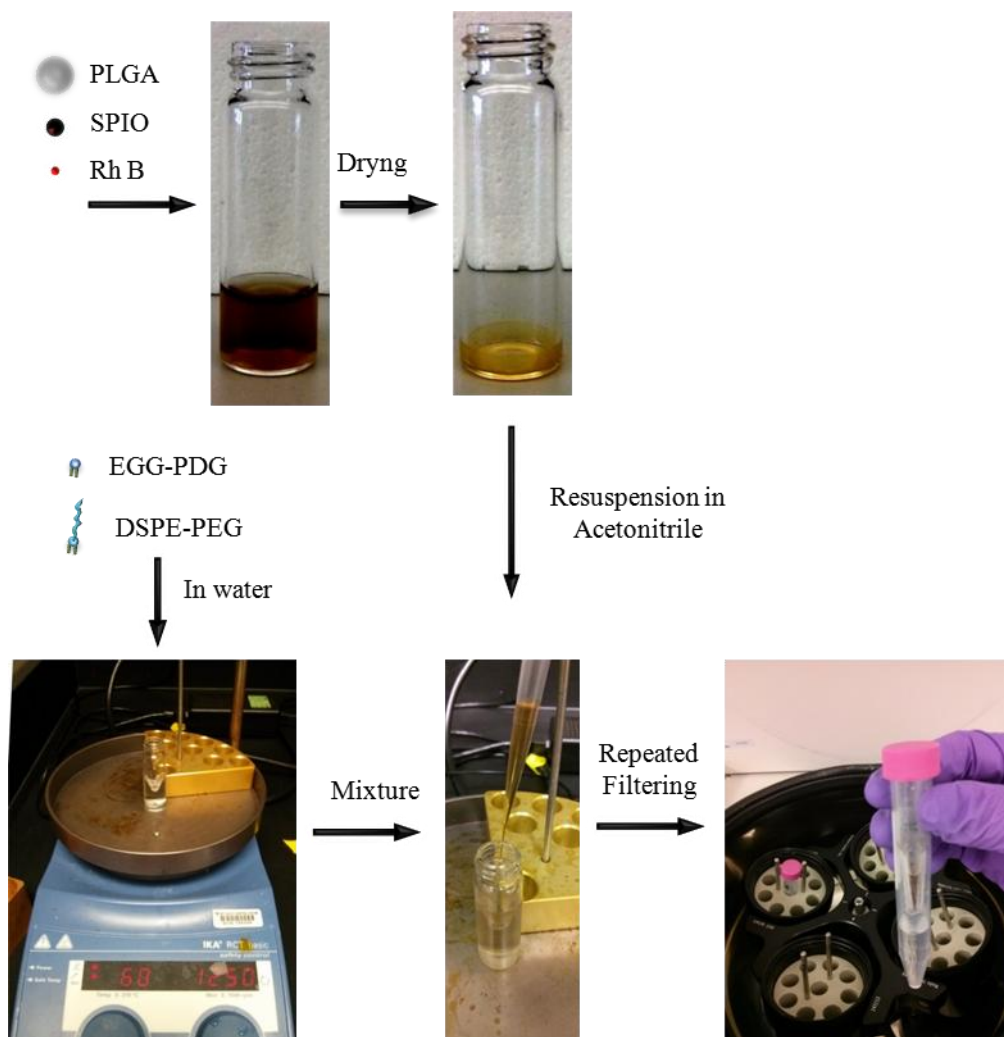


Figure 4-2. Synthesis steps in Hybrid NanoParticles (HNPs).

The hydrophobic mixture of IOs, Rh B, and PLGA was left dry and then re-suspended in Acetonitrile. In the meantime lipids were stirred at 60 °C in water and then added with the first component when still on the stirring. The obtained solution is purified several times by centrifugal filtering and resuspended in DI water

DPNs

In collaboration with Dr. Jaehong Key, DPNs were synthesized following the procedure detailed in [130]. Briefly: a silicon master template provided by the Dept. of Bio/Nanotechnology and /Engineering, University of Magna Graecia, Italy, was used in the fabrication of hydrogel templates. 5 ml of PDMS:elastomer (10:1) was transferred onto the silicon master template. To completely polymerized PDMS solution, it was placed at 60 °C in oven. For preparation of PLGA, 30 mg of powder were dissolved in dichloromethane (DCM). 100 µl of the diluted solution were mixed with 0.5 mg of 5 nm SPIOs (in toluene) and dried overnight in oven (60 °C). The mixture was resuspended 1:1 in 200 µl of DCM; aftermath PEG dimethacrylate (10 µl), RhB (0.5 mg), and Photo-initiator (10 µl) was also included. This polymeric mixture was loaded on the PVA templates and exposed to UV-light further polymerization. After drying, PVA templates were dissolved in deionized water at 60 °C and then the DPNs harvested from the dissolved PVA templates. Commercially available reagents were utilized for the synthesis: Poly(vinyl alcohol) (PVA, Mw 31,000-50,000), Poly(DL-lactide-co-glycolide) acid terminated (PLGA, lactide: glycolide 50:50, Mw 38,000-54,000), Poly(ethylene glycol) dimethacrylate (Mn 750) (PEG dimethacrylate), 2-Hydroxy-4'-(2-hydroxyethoxy)-2-methylpropiophenone (Photo-initiator), and ultras-small SPIO (II,III) (5 nm) were purchased (Sigma, St. Louis, MO, USA). Sylgard 184 kit as polydimethylsiloxane (PDMS) and elastomer was purchased from Dow Coming Corp (Midland, MI). Methacryloxyethyl thiocarbamoyl rhodamine B (RhB) was purchased from

Polysciences, Inc. (Warrington, PA). 1,2-dioleoyl-sn-glycero-3-phosphoethanolamine-N-(lissamine rhodamine B sulfonyl) was ordered from Avanti Polar Lipids Inc. (Alabaster, AL).

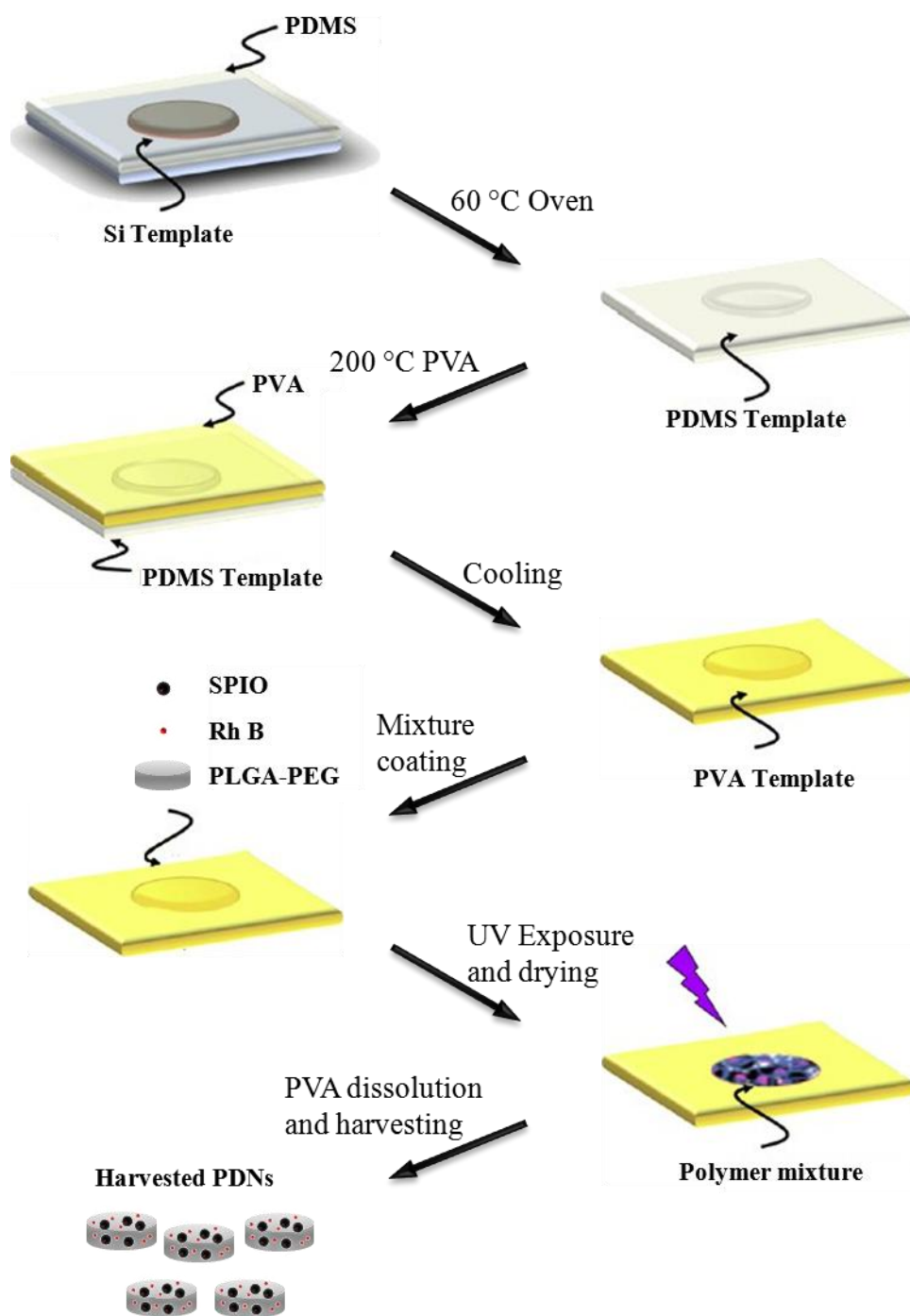


Figure 4-3. Discoidal Polymeric Nanoconstructs (DPNs) synthesis.

A first complementary template in PDMS is obtained from the original Si template. From that, a perfect copy of the original template is obtained in PVA. A mixture of Rh B, 5 nm iron oxides nanoparticles and PEGylated PLG is coated on this last template. The particles are collected upon degradation of the PVA and purification.

Magnetic NanoFlakes (MNFs)

Prior to nanoconstruct synthesis, deoxycholic acid-modified chitosan conjugate (deoxy-chitosan) was synthesized following the published protocol in [131]. Briefly, chitosan (80 mg) was dissolved in a 9/1 (v/v) solution of DMSO/water, and then deoxycholic acid (200 mg) activated by EDC/NHS in presence of catalytic amount TEA was added, as demonstrated in **Figure 4-4A**. The products were then purified by extensive dialysis and lyophilized to obtain dry powder. The synthesized deoxy-chitosan was characterized using FT-IR spectroscopy (**Figure 4-4B**).

Then, the synthesis of the MNFs followed an emulsion procedure, in which 10 ml of 1% acetic acid in water containing 750 μg of 1,2-distearoyl-*sn*-glycero-3-phosphoethanolamine-*N*-[carboxy(polyethylene glycol)-2000] (1 mg ml^{-1} of DI water, Carboxalate-DSPE-PEG - Avanti Polar Lipids, Inc.), 500 μg of *L*- α -phosphatidylglycerol (1 mg ml^{-1} of DI water, Egg PG - Avanti Polar Lipids, Inc.), and 1 mg of deoxy-chitosan dispersed in 1% acetic acid in water (1 mg ml^{-1}) were mixed together.

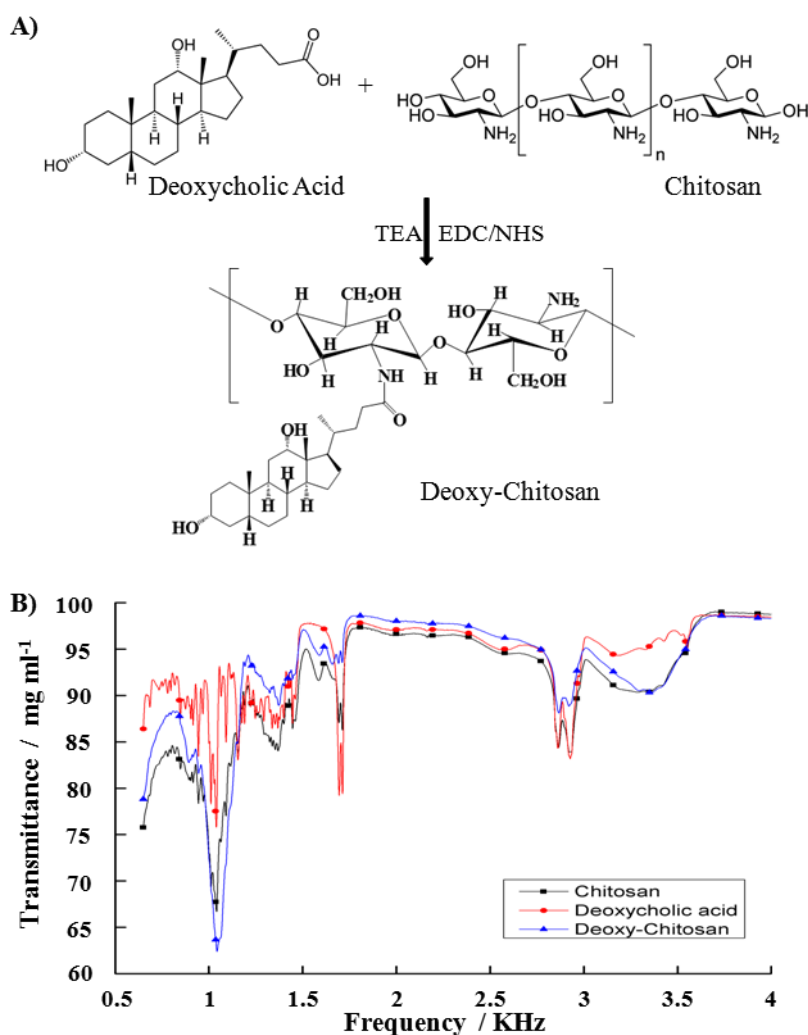


Figure 4-4. Deoxy-chitosan conjugation.

(A) Schematic of Deoxy-Chitosan reaction. (B) FT-IR spectra of chitosan, deoxycholic acid, and chitosan-deoxycholic acid conjugate. The characteristic bands, amide I (1656 cm^{-1}), amide II (1593 cm^{-1}), and amide III (1373 cm^{-1}) of chitosan are intact in both chitosan and chitosan-deoxycholic acid conjugate. However, the H-bonded, N-H Stretching, and O-H stretching centered at 3500 cm^{-1} to 3100 cm^{-1} was slightly modified to small intense band at 3446 cm^{-1} along with the broad band, which reduces the extent of the H-bonding due to the conjugation with deoxycholic acid, confirms the formation of the conjugates. Likewise, the absorption of alkyl C-H stretching band of conjugate decreases as compare to that of chitosan at $2950\text{--}2850\text{ cm}^{-1}$ is possibly due to the incorporation of alicyclic rings.

Finally, for the synthesis of the nanoconstruct 1.1 mg of magnetite (Fe_3O_4) cubes coated with a thin layer of oleic acid dispersed in chloroform, was emulsified in the lipid, PEG, the deoxy-chitosan mixture. Following overnight evaporation of chloroform, the particles were filtrated 4 times using Millipore centrifugal filters to clean any residual of acetic acid and unformed particles, and then re-diluted in Milli-Q water or PBS as needed.

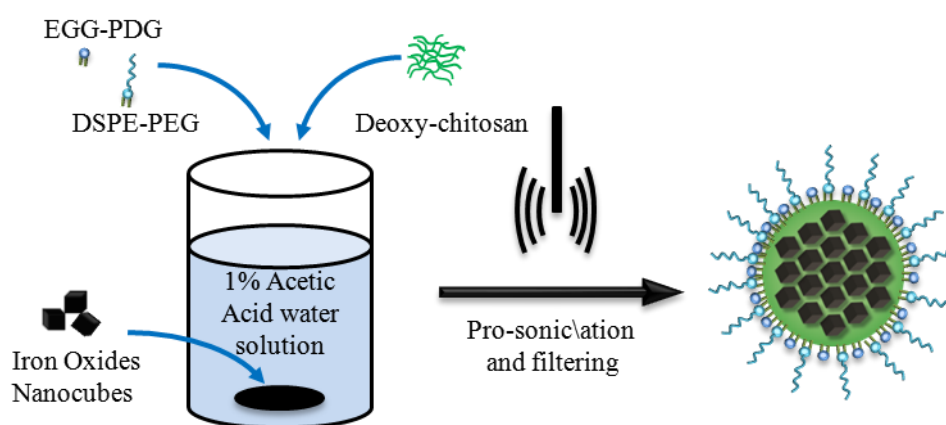


Figure 4-5. Emulsion procedure for Magnetic NanoFlakes (MNFs).

Lipids and deoxy-chitosan were earlier mixed in a 1 % acetic acid solution at room temperature. Hydrophobic solution of nanocubes is then placed at the bottom of the tube without further mixing. Emulsion is executed by pro-sonication of the whole solution for 1 min. The result was let under hood for few hours to let the organic solvent completely evaporate. Finally the solution was purified by centrifuge filtering.

4.1.2. *Chemico-physical characterization*

Physical, chemical, and magnetic characterizations followed the same instruments and procedure previously described in **Chapter. 3** for SPIOs, where possible. Direct light size measurements are not adequate for discoidal particles, which not present an aspect ratio close to 1; DPNs measurements were therefore performed using an atomic force microscope (AFM).

Atomic Force Microscope (AFM)

AFM from Bruker (high-speed Bruker MultiMode AFM – Billerica, MA, USA) was employed for a correct analysis of DPNs width and height. A silicon tip on nitride lever (spring constant = 0.4 N m^{-1}) of 500 nm was utilized with in-air scan modality SCANASYST tapping mode, 4 Hz scanning rate. DPNs in aqueous solution were prepared by dropped few μl on a cleaned silicon wafer and completely dried at room temperature. Last, the silicon wafer was directly attached to the magnetic stainless steel disc on the AFM.

4.1.3. *Cell Culture*

Cell lines

Cell experiments *in-vitro* were performed on the following cell lines: *i*) *J-774 macrophages* – this macrophage cell line is provided by ACTT and cultivated using medium DMEM, 10% FBS, 1% Pen/strep in standard conditions of 37 °C and humidified 5 % CO₂ atmosphere; *ii*) *HUVECs* – Human umbilical vein endothelial cells from PromoCell were originally cultured in 10 cm petri-dish, grown until the 6th passage in endothelial growth

(PromoCell) at 37 °C, in a 5 % CO₂ atmosphere; *iii*) *MDA-MB-231* – breast adenocarcinoma, obtained from ATCC, cultured in Leibowitz L-15 medium supplemented with 10% FBS and antibiotics (100 U ml⁻¹ penicillin G, 100 mg ml⁻¹ streptomycin), and grown at 37°C in a free gas exchange with atmospheric air. **Figure 4-6** shows these three cell line during culture.

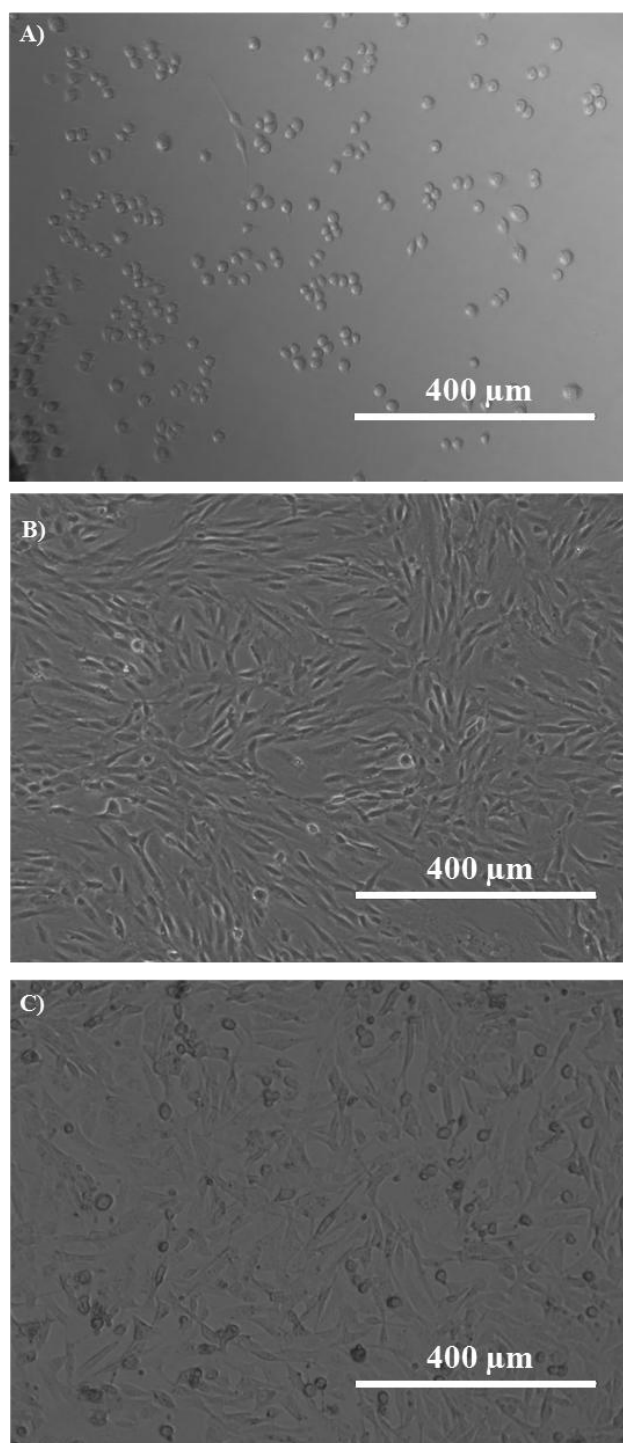


Figure 4-6. Cultured cells in adhesion

(A) J-774, (B) HUVECs, and (C) MDA-MB-231 cell line in culture.

Cell culturing

Growing cells requires extreme care in observing standard procedure and sterile environment to assure good health, uniformity of responses, and to prevent any sort of pollution, i.e. microbial contamination. Handling of any cell line therefore must be operated under a sterile biohood with constant aspirating air flow; to ensure the work safety for the user, high-efficiency particulate absorption (HEPA) filters are required as the air exits the biosafety cabinet. Basic sterilization procedures include earlier wiping with 70 % ethanol solution on worn safety gloves and working surface, as well as every non-sterile object brought inside the hood; in addition the hood surface was wiped again after the use and exposed to UV light for a minimum of 20 min to totally deplete any presence of bacteria.

Cells were typically seeded in Petri dishes (3.5, 5, or 10 cm in diameter) and stored in incubators when not operated; growing medium is replaced on a 2 days basis, or depending on the particular cell line requirements. Harvesting method of cells for suspensions or reseeded, i.e. when confluent, depends on the cell line. For J-774 macrophages medium was removed with a Pasteur pipette and the cells were washed with a small volume of DPBS with Ca^{2+} and Mg^{2+} ; cells were gently scraped from the dish bottom and collected in tube. HUVECs and MDA-MB-231 cell were washed in the same DPBS and treated with trypsin (PromoCell). Trypsin is used to cleave proteins bonding the cells to the dish, in few minutes under incubation; as soon as the cells were detached from the dish growing medium in ratio 3:1

was added with the purpose of blocking the trypsin function, and the cells were collected in tube (**Figure 4-7A**).

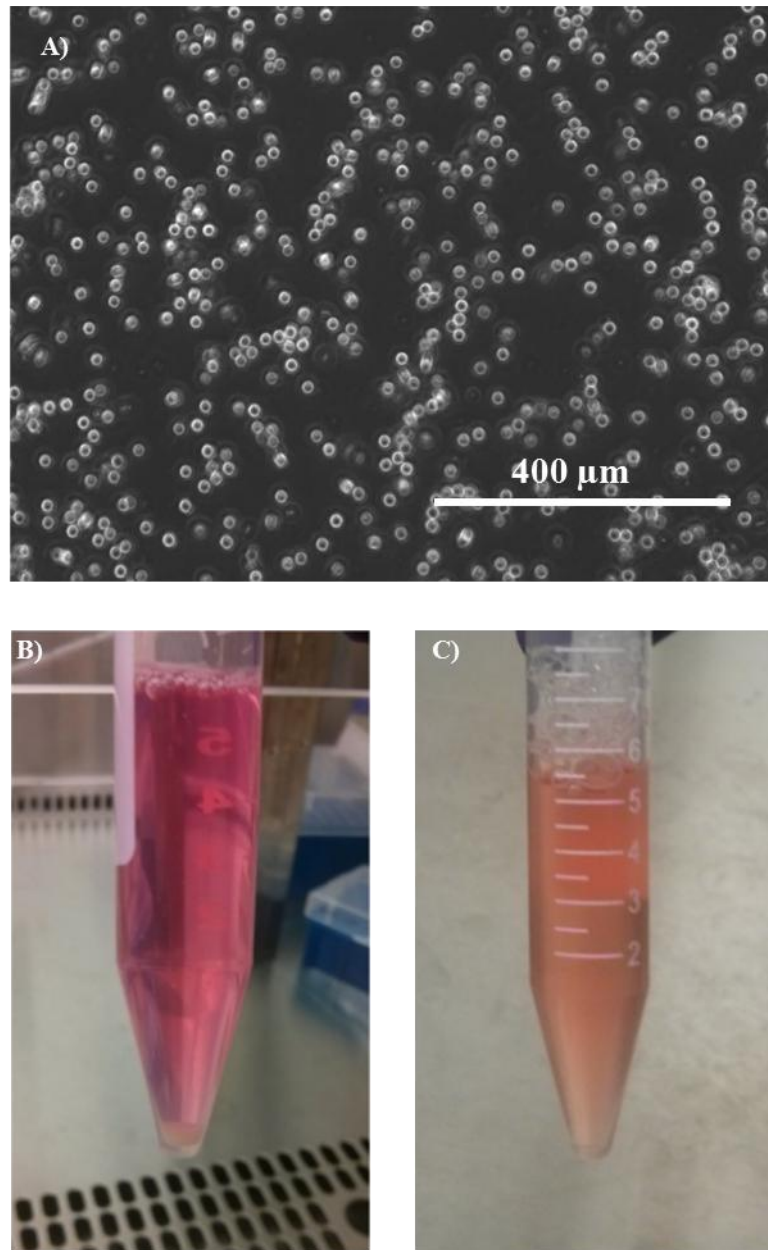


Figure 4-7. Cells harvesting process

(A) Suspended cells (HUVECs) (B) centrifuged cell pellet before re-suspension and (C) after.

For both methods, the cells need to be centrifuged (~4 min at 11.2) so that the supernatant can be removed and the cell pellet re-suspended in few ml of fresh growing medium (**Figure 4-7B** and **C**); cells can be reseeded or treated in suspensions. To count the cells number, 10 μl of the suspended solution are mixed 1:1 with 0.4 % trypan blue solution; 10 μl of the mixture are applied to each of the two coverslip edges of a hemocytometer – Hausser Scientific. Trypan blue is a diazo dye used as vital stain for a dye exclusion method, since it is not absorbed by a viable cell but it traverses a dead cell membrane (**Figure 4-8**). Dead – or dying – cells are therefore colored in blue, whilst live cells are easily distinguishable under the microscope. The average number of living cells on 4 quadrants is used to calculate the cell concentration in suspension, based on the formula:

$$\text{conc} = \text{average cell count} \cdot \text{dilution factor} \cdot 10^4 \quad [\text{cell ml}^{-1}] \quad (4-1)$$

Where the dilution factor is 2. All the solution used are stored following vendor instruction and warmed in water bath at 37 °C before use.

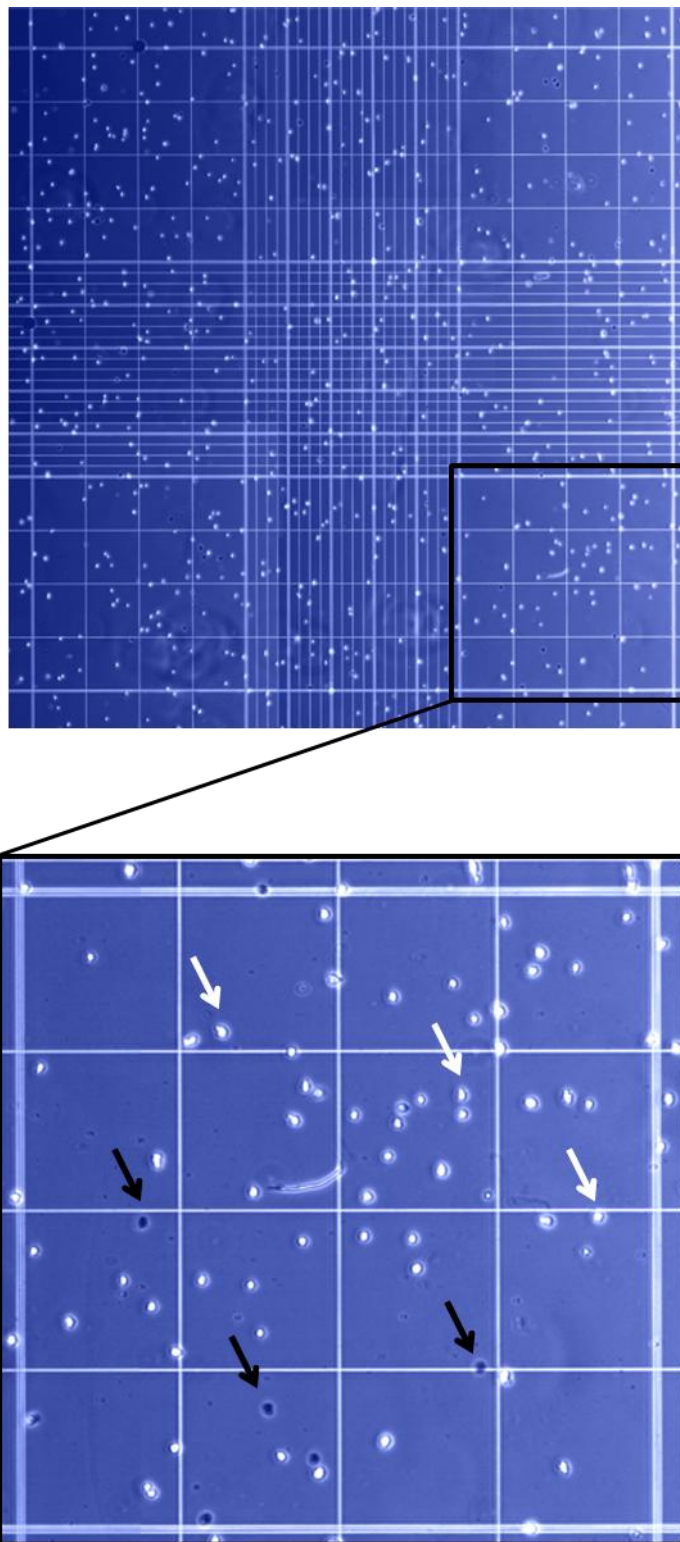


Figure 4-8. Cell counting

Hemocytometer counting area and magnification of the bottom-right quadrant. Detail of living (white) and dead (dark) cells. Arrows point to some of these as example.

Viability assay

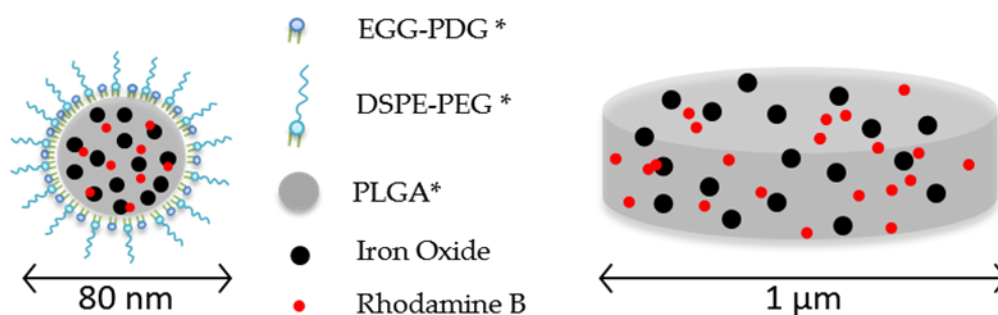
MTT viability tests (3-(4,5-Dimethylthiazol-2-yl)-2,5-Diphenyltetrazolium Bromide, from Invitrogen Life Sciences) was used in order to assess the toxicity arising from the several particles formulation. Cells seeded in 96-well plates were treated with at least five different iron concentrations (0, 50, 100, 500, 1000 μ M) of iron, for at least 5 replicates; then cytotoxicity tests were run at 24, 48, and 72 hrs 5 mg of MTT salts were previously dispersed per ml of PBS, and 10 μ l of solution added to each well and incubated again until the interior of the cells could be seen by microscope totally stained in blue (≥ 2 hrs); plates were then centrifuged at 2000 g for 5 min in order to completely deposit the hydrophobic salts crystals to the bottom of the wells. After removing the medium and replacing it with 100 μ l 2-propanol (from Fisher Scientific, #A416-500) to suspend the crystals, the plates were spun for 10 min (300 rpm); absorption can be read (Synergy H4 Hybrid Multi-Mode Microplate Reader, from BioTek Instruments, Inc.) at both 540 and 690 nm wavelength. Reading values from the second wavelength were subtracted from the first one to clear background noise. Final average and standard deviation of viability values were calculated over the five replications after blank subtraction. Control in pure medium was taken as reference at 100 %.

4.1.4. Results

PLGA based constructs

Investigation on the confinement effects of SPIOs were originally developed with two particles formulations based on a polymeric matrix of PLGA, represented in **Figure 4-9**:

- (i) Hybrid NanoParticles (HNPs) [132];
- (ii) Discoidal Polymeric Nano-constructs (DPNs) [130].



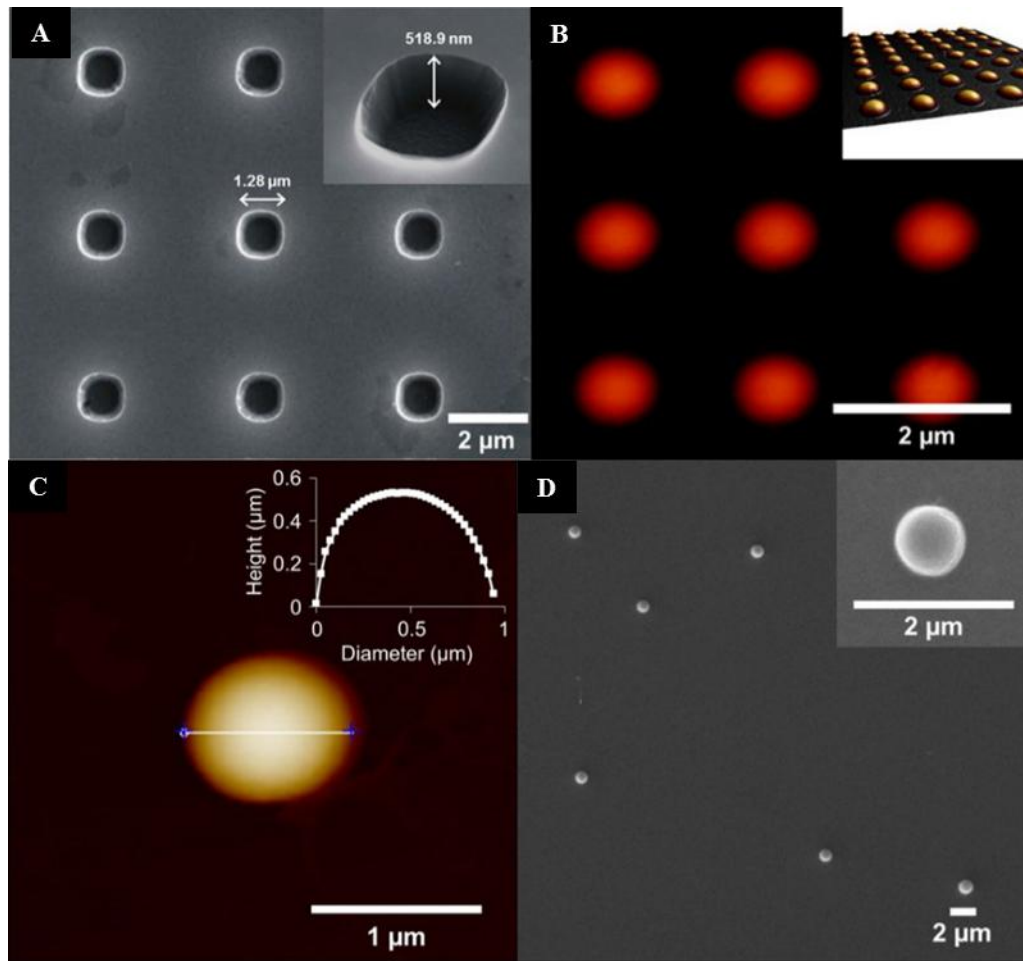
* DSPE-PEG : Carboxil-1-2-Distearol-sn-Glycero-3-Phosphoethanolammine-N-[Methoxy(Polyethylene Glycol)-2000]
 EGG-PDG: L- α -Phosphatidyl-DL-Glycerol (Egg Chicken)
 PLGA: Poly(DL-lactide-co-glycolide) acid terminated

Figure 4-9 Hybrids NanoParticles (HNPs) and Discoidal Polymeric Nanoconstructs (DPNs) structure.

Shown in the figure are the inner structures of both HNPs (**left**) and DPNs (**right**) used for preliminary tests. Both present a polymeric matrix in PLGA, loaded with several sizes of IOs and Rhodamine B fluorescent dye. HNP core is stabilized by a corona of PEGylated lipids, which permit a better solubility in hydrophilic media. Diameters are ~80 nm and ~1000 nm respectively; DPNs height is 500 nm.

HNPs are nano-metric assemblies based on a matrix of PLGA with a PEGylated lipid corona. The polymeric core is highly porous and allows for inner loading of third components, as can be drugs or, in this case, 17 nm spherical IO particles; the high porosity is also critical for T_2 contrast performances. The aim of the PEGylated lipid corona surrounding the polymer is to stabilize the structure and provide a higher fluidity in hydrophilic suspension. Together with the SPIOs, HNPs were loaded with Rodhamine B as red fluorescent staining. Direct laser measurements (DLS) indicate a well monodispersed population, $PDI = 0.198 \pm 0.008$, and hydrodynamic radius of 78.8 ± 6.9 nm.

DPNs are PLGA-based discoidal nano-constructs with highly homogeneous sizes of 1 μm diameter and 500 nm height, due to their top-down method of fabrication. PLGA was directly functionalized with PEG chains, which highly increase water affinity. Similarly to HNPs, the porous structure of PLGA permits loading with several components and water diffusivity for enhanced contrast imaging properties; in addition, their bigger size assures higher loading capacity therefore versatility of application. AFM measurement (**Figure 4-10**) reports 968 nm in diameter and 509 nm in height, and zeta-potential is quantified to be -19 ± 8 mV.



J. Key et al. / Biomaterials 34 (2013) 5402–5410

Figure 4-10. Physical characterization of DPNs.

(A) SEM image original Si template reporting a width of $1.28\ \mu\text{m}$ and a height of $518.9\ \text{nm}$. (B) Fluorescence microscopy of the particle inside PVA template as for before the harvesting, and inset of a reproduction of the PDMS complementary template. (C) AFM image indicating a diameter of $968\ \text{nm}$, and a height of $509\ \text{nm}$. (D) SEM image showing the high uniformity of DPNs. A high resolution image of a single particle is reported in the inset. (Source: Key, J., Aryal, S., Gentile, F., Ananta, J. S., Zhong, M., Landis, M. D., Decuzzi P.; *Biomaterials*, 2013 Vol. 34 Num 21)

MNFs: physico-chemical characterization

Last, a third formulation named magnetic nanoflakes was developed with a polymeric core of chitosan. The synthesis procedure was defined through a systematic investigation aimed to refine average beads size, population homogeneity, and magnetic core encapsulation. The final protocol, deeply described in paragraph 4.1.1, consists in an emulsion technique where few tens of ~ 22 nm hydrophobic NCs are closely joined together by deoxy acid-modified chitosan (deoxy-chitosan), and then stabilized by a lipid monolayer and PEG chains. A schematic representation of the MNF is shown in **Figure 4-11A**.

The MNF stability and monodispersity were determined up to 7 days using standard DLS analysis. The data of **Figure 4-11B** show an average hydrodynamic diameter of 156 ± 3.6 nm and a polydispersity index (*PDI*) of ~ 0.2 throughout the 7 days. TEM images of the NCs used for the formation of the magnetic nanoflakes are presented in **Figure 4-11C**, where the image in the right-top inset clearly demonstrates an edge size of ~ 22 nm. Electron micrographs of the whole nanoconstruct are presented in **Figure 4-11D, F**. These micrographs provide a diameter of the MNFs of ~ 140 nm, under dry conditions. Also, the SEM and TEM images show the spatial organization of the NCs within the chitosan matrix which resembles to that of the unpopped pop-corn; this inspired the name for these nano-constructs. In the synthesis of the MNFs, the iron yielding is 50 ± 15 % which was calculated as the ratio between the initial and final mass of iron estimated via ICP-OES. The zeta-potential of the MNFs was measured to be 37.9 ± 2.7 mV, lower than that

measured for chitosan alone (~46 mV). The reduction in surface electrostatic charge has to be associated with the presence of the lipid and PEG-COOH corona which stabilizes the whole nanoconstruct.

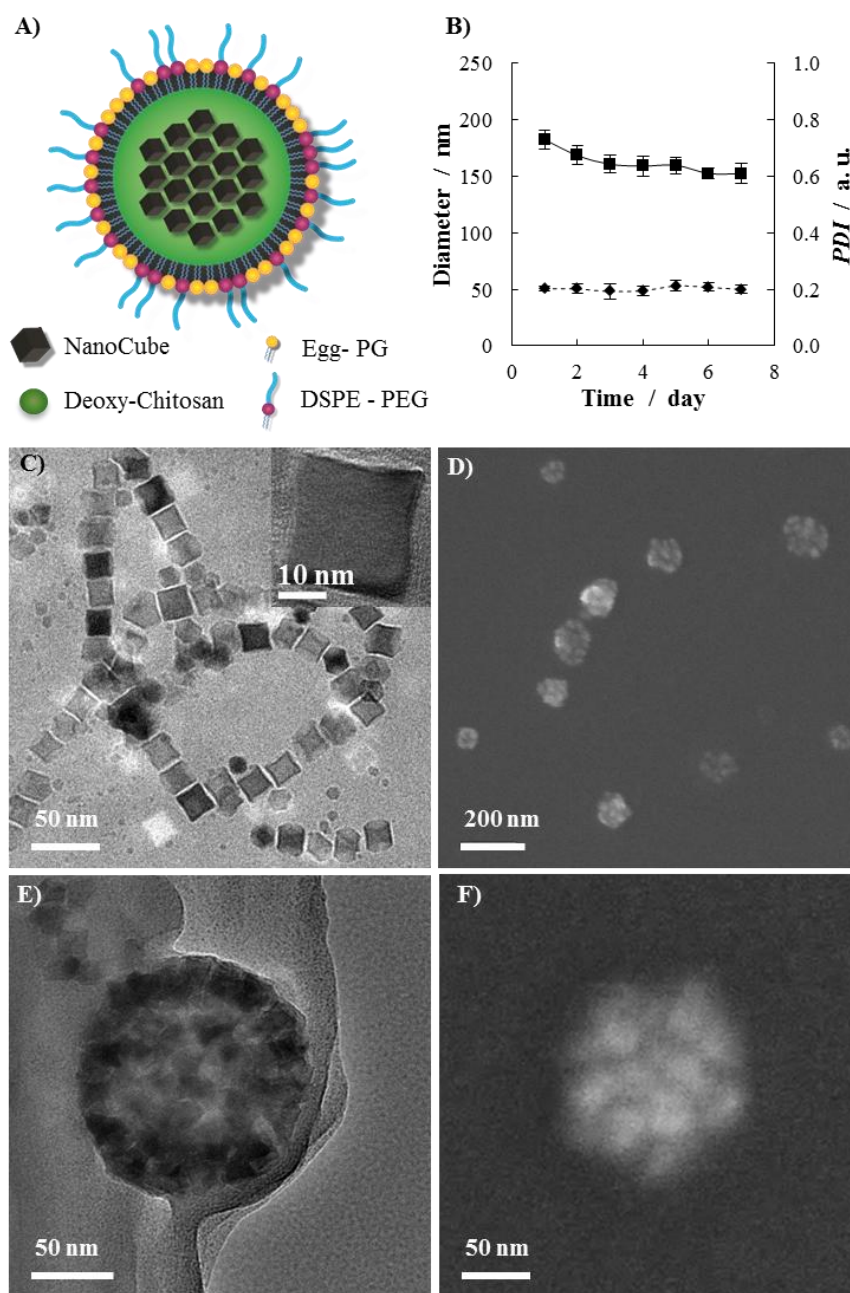


Figure 4-11. Physico-chemical properties of Magnetic NanoFlakes (MNFs).

(A) Schematic representation of a MNF; (B) Stability test over time in PBS solution (av. diameter = 156 ± 3.6 nm; av. $PDI = 0.2 \pm 0.007$); (C) TEM image of the nanocubes (NCs) used during the synthesis. The NC edge length is ~22 nm (inset); (D) SEM image of the MNFs; (E, F) TEM and SEM images of the MNFs showing the NCs confined within the polymeric matrix. MNFs appear as spherical nanoconstructs with an average size of ~140 nm.

Cytotoxicity

The cytotoxic behavior of the magnetic nanoflakes was characterized on endothelial cells (HUVECs), which represent the first cell type encountered by nanoconstructs upon system injection, and a breast cancer cell line (MDA-MB-231). Different concentrations of MNFs were incubated with the cells and cell viability was monitored at 24, 48 and 72h post incubation using a MTT assay.

As shown in **Figure 4-12**, during the first day of incubation, no loss in viability is observed for the HUVECs up to concentrations of 500 μM . At 1,000 μM , the HUVEC viability dropped to 70%. Similarly, some negligible toxicity (i.e. viability < 90%) is detected at concentrations larger than 100 μM for the second and third days of analysis. A similar trend is observed for the MDA-MB-231, but the overall toxicity is lower than what documented for the HUVECs. Cancer cell viability is higher than 80% for concentrations of 500 μM up to 72h. Only at the highest concentration, of 1,000 μM , the cell viability of the MDA-MB-231 dropped below 80%.

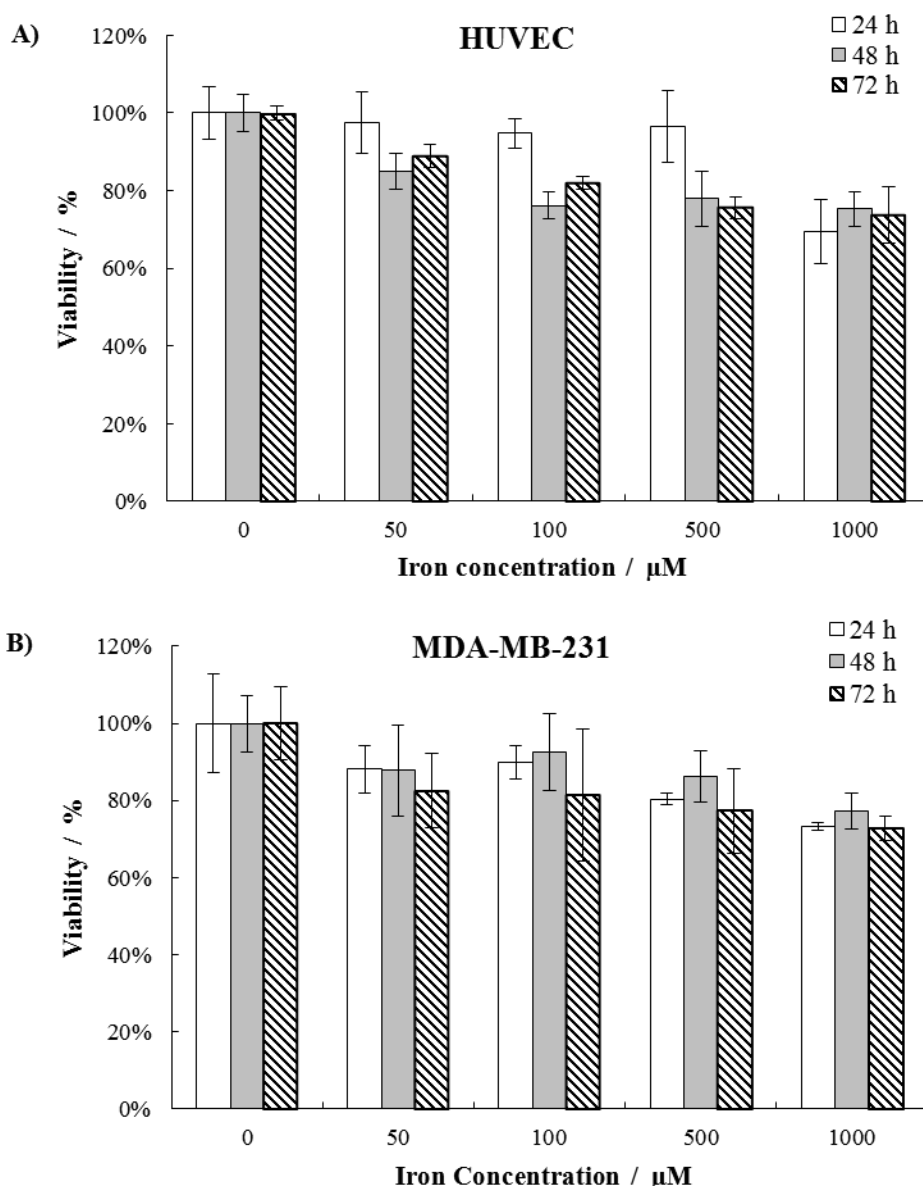


Figure 4-12. Cytotoxicity of MNFs.

To assess the toxic effects of bare MNFs on both healthy and tumor cells, MTT viability test was performed on (A) HUVECs and (B) breast cancer MDA-MB-231 cell lines up to three days of incubation in normal conditions and with no exposure to magnetic field. Cell viability was measured at three different time points and four different MNF concentrations, up to a particle concentration in the culture medium of 1mM of iron. HUVECs cells, well-known for their high sensitivity, show a good survival rate up to 80 % viability at 72 hr; as well, MDA-MB-231 cancer cells show a similar trend, with a slightly higher overall viability.

4.2. *Magnetic dragging*

4.2.1. *Microfluidic experiments*

Fluorescence microscope

The observation of micro- and nano- scale was possible thanks to an inverted fluorescence microscope – Ti-Eclipse, Nikon (**Figure 4-13A**). Particles, static or in motion, were seen using dry microscope objectives, magnifications of 10x, 20x and 40x; the microscope mounts fluorescent filters for blue (DAPI) and red (FITC) transmitters. These components allowed for a clear view on particles down to 200 nm in size. Dynamic acquisition of images was possible because of Andor's Luca^{EM} S camera; it utilizes a 658 × 496 “interline frame transfer” EMCCD sensor to acquire the region of interest (ROI). A highly informative real time sequence of events could further be generated by means of an automatic shutter on the transmitted light path, which alternates the acquisition of the desired ROI in bright-field and fluorescence mode with duty cycle on the orders of tenths of a second. The shutter operation, all the acquisition, and analyses were managed by the dedicated software *NIS-Elements*, from the same microscope producer.

Flow chamber

The same shear rate and flow velocity the particles would experience in a vein were reproduced using a commercially available flow-chamber (GlicoTech), shown in **Figure 4-13B** and **C**. This is a microfluidic device composed of a discoidal body, 3.5 cm diameter × 1 cm height, in casted acrylic; two inlet/outlet tubes provide for the flow, and a third one is

connected to an annular chamber for vacuum. The 20 mm long channel is created applying on of the silicon rubber gaskets, provided in several combination of width (0.25, 0.5, 1 cm) and thickness (0.005 and 0.01 in), and then a glass coverslip. Vacuum grease spread between the gasket and the coverslip enhances the adhesion between these and the three components, which are firmly kept together by vacuum. For the flow, a syringe containing the sample with the desired concentration was mounted on syringe pump – Pump 33, Harvard Apparatus – and connected to the flow chamber inlet; it provides a constant flow rate from 0.0004 $\mu\text{l/hr}$ up to a maximum of 106.6 ml/min, and can host syringe sizes from 0.5 μl up to 140 ml. Using the inverted microscope described above, ROI of 658×496 px are captured over the channel with the higher possible acquisition rate, in relation with the particular exposure time required by the sample for an optimal visualization.

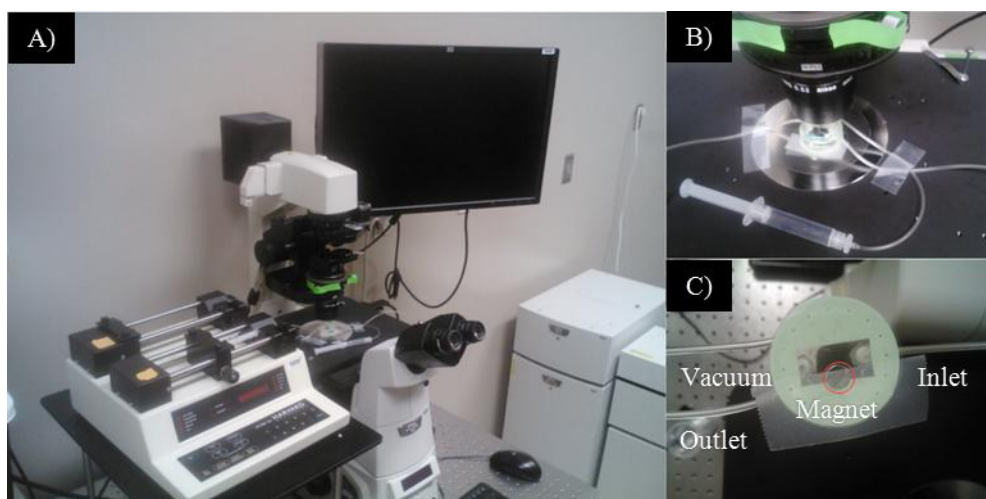


Figure 4-13. Microfluidic apparatus

(A) Fluorescence inverted microscope with the syringe pump. (B) The flow chamber mounted on the microscope. (C) Back of the flow chamber with the magnet mounted on the channel side

Static and in-flow particles dragging

The capacity to respond at an external static magnetic field attraction was investigated in both cases of resting and dynamic fluids. The fluorescence microscope previously described was employed to record in real time the particles, nanoconstructs, or IOs loaded cells dragged using 2 discoidal magnets (**Figure 4-14**) purchased by Apex Magnets:

- a) 12.7 mm × 1.6 mm height diameter, grade N48 – able to express a magnetic pull force of 35.6 N at an L50 distance of 0.33 mm from steel and 7.9 N at L50 distance of 0.75 mm from a second magnet;
- b) 6.4 mm × 0.8 mm height diameter, grade N52 – able to express a magnetic pull force of 9.38 N at an L50 distance of 0.12 mm from steel and 1.51 N at L50 distance of 0.42 mm from a second magnet;

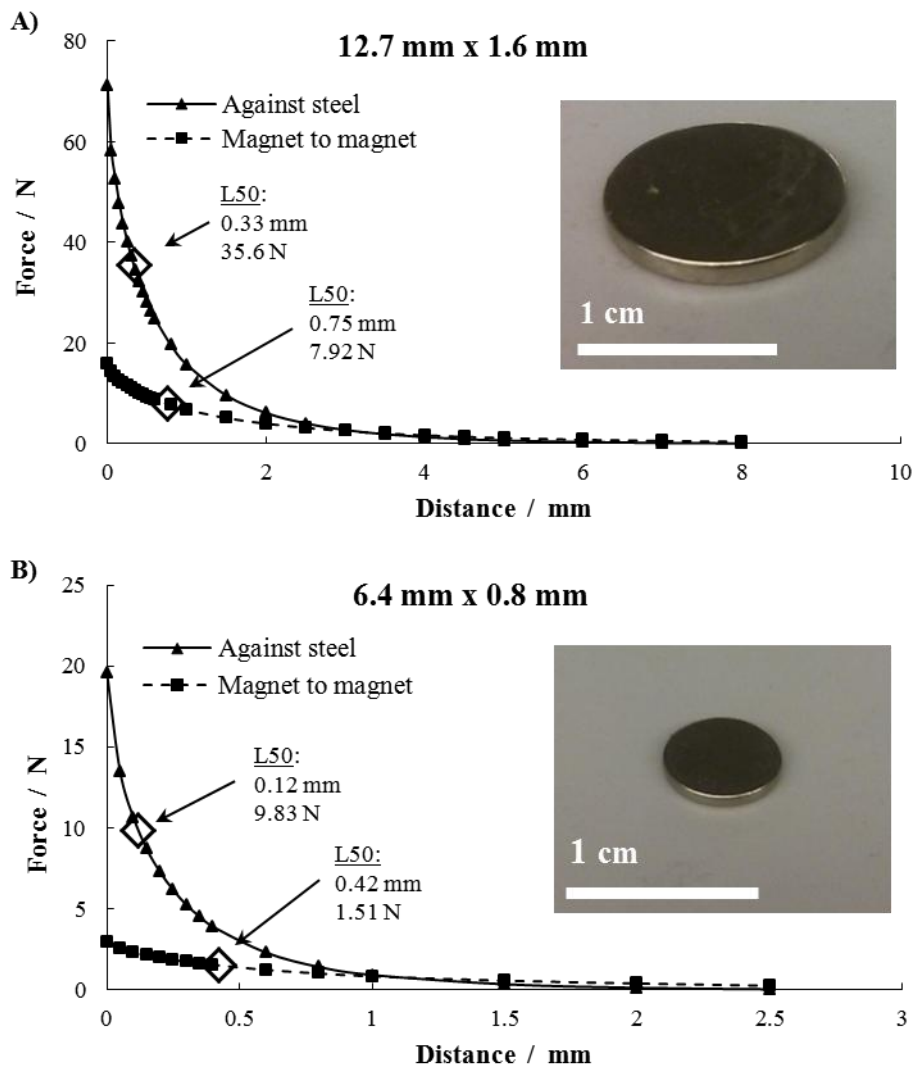


Figure 4-14. Magnets used for dragging experiments.

The plots show the pull forces (magnet/steel and magnet/magnet) of the (A) 12.7 mm and (B) 6.4 mm diameter discoidal magnets used during experiments, with images in the insets.

In all the experiments, except for a few cases in which was not possible or not convenient for the researched interrogation, the samples were prepared such to present a red fluorescence, and the microscope shutter set to switch between bright field and FITC filter. In this way recorded movies show superimposition of the two. Red fluorescence was provided by Rhodamine B dye – *L- α -Phosphatidylethanolamine-*N*-(lissamine rhodamine B sulfonyl)*, Avanti Polar Lipids, Inc.

For static dragging tests a drop of few μl of sample was placed on a glass coverslip edge and the microscope field of view is pointed to the drop edge closer to the magnet. The focus was set case-by-case such to better distinguish the highest number of particles possible, eventually close to half the height of the drop; nevertheless, due to its small height, most of the particles are still recognizable even if out of focus. The software started recording and, following, the magnet (a) was approached to the sample; movies were recorded at 1, 3 and 6 mm distance from the drop edge, for the time required by each experiment (but always ≥ 2 min).

For dynamic dragging tests, meaning a quantification of the particles drifting from the blood flow direction towards a static magnet and their local accumulation, the flow chamber from GlicoTech previously described was mounted on the microscope platform with magnet (b) attached on its bottom (**Figure 4-15**). In this system a laminar flow with parabolic velocity profile was established in the between the two parallel walls. The channel sizes (height h and width w) and the flow rate Q provided by the syringe pump are chosen such to satisfy the equation:

$$S = 6 \frac{Q}{h^2 w} \quad [\text{s}^{-1}] \quad (4-2)$$

for shear rate S values relevant to physiological condition of healthy tissues ($100 - 200 \text{ s}^{-1}$) or sub-physiological ones found in tumoral vasculature ($10 - 100 \text{ s}^{-1}$) [133]. Magnet was positioned halfway in the channel on one side, in order to witness the particle drifting from the horizontal flow towards the magnet.

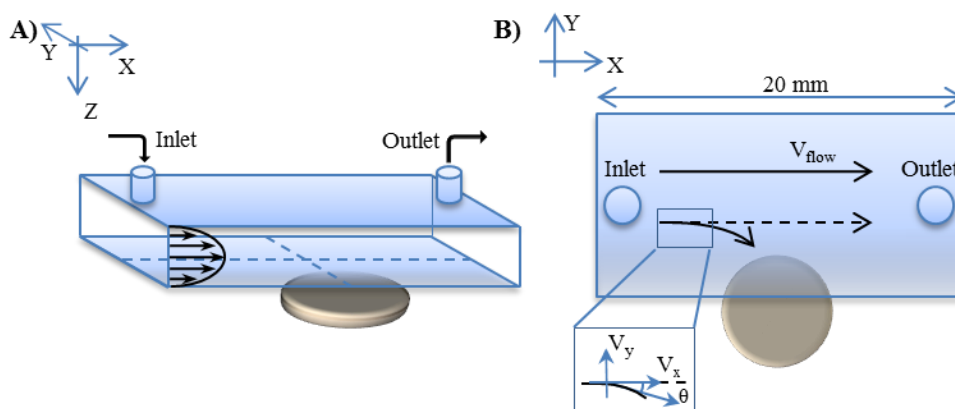


Figure 4-15. Flow chamber channel with magnet position.

Representation of the channel inside the flow chamber and with the magnet position during dragging experiments. The magnet is poses halfway of the channel, on the side

The camera started recording right after the flow completely fills the channel. For the drifting quantification was then measured the angle of particle trajectory versus the distance from the magnet. The preferential accumulation of particles required an earlier preparation step: a sample drop is left dry on the coverslip with a magnet underneath before mounting on the flow chamber. Once the whole system is mounted, the deposited particles will eventually get

magnetized by the external magnetic field, producing a local magnetic gradient in their proximities. This cooperative effect was quantified by the increasing area of the originally deposited clusters over time. All the images captured were processed using *Image-J* software (**Figure 4-16**).

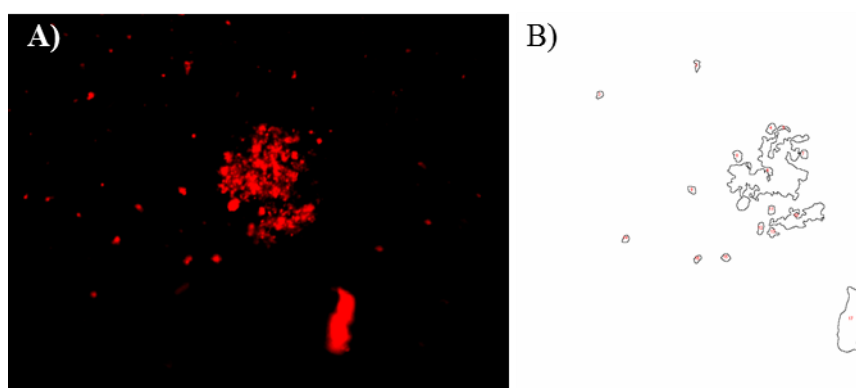


Figure 4-16. Imaging process of the flow chamber aggregates.

(A) Fluorescence microscope image of deposited aggregates of DPNs particles. (B) Outlines of the aggregates processed by *Image J* software during the area quantification.

Imaging process

Every post processing of images, for size distribution or intensity fluorescence estimation, were executed by *ImageJ software*, developed for scientific purposes at the American National Institutes of Health (NIH), Research Center, in Maryland.

4.2.2. Results

HNPs were employed for static dragging studies of macrophages upon internalization. J-774 macrophages cell line is incubated for 6 hrs. with HNPs+17nm IOs, iron concentration of 0.9 mM. After washing and re-suspension, J-774 are dropped on a glass coverslip and mounted on a fluorescence inverted microscope (see paragraph 4.2.1). Superposition of bright-field and FITC fluorescence images in **Figure 4-17** demonstrates a clear internalization of the HNP+17 nm IOs. In every panel the totality of the fluorescent signal is co-localized within the macrophages; instead, no signal can be found on the outside. At time $t = 0$, the magnet (a) described in section 4.2.1 was placed ~1 mm away from the drop edge, in correspondence to the bottom side of the figure. **Figure 4-17** shows frames from the recorded video of the experiment up to 20 sec at intervals of 4 sec. In this sequence, cells quickly accumulates on the edge next to the magnet, pushed by the magnetic particles internalized; after 15 sec the only cells not moving towards the magnet are those already attached to the coverslip.

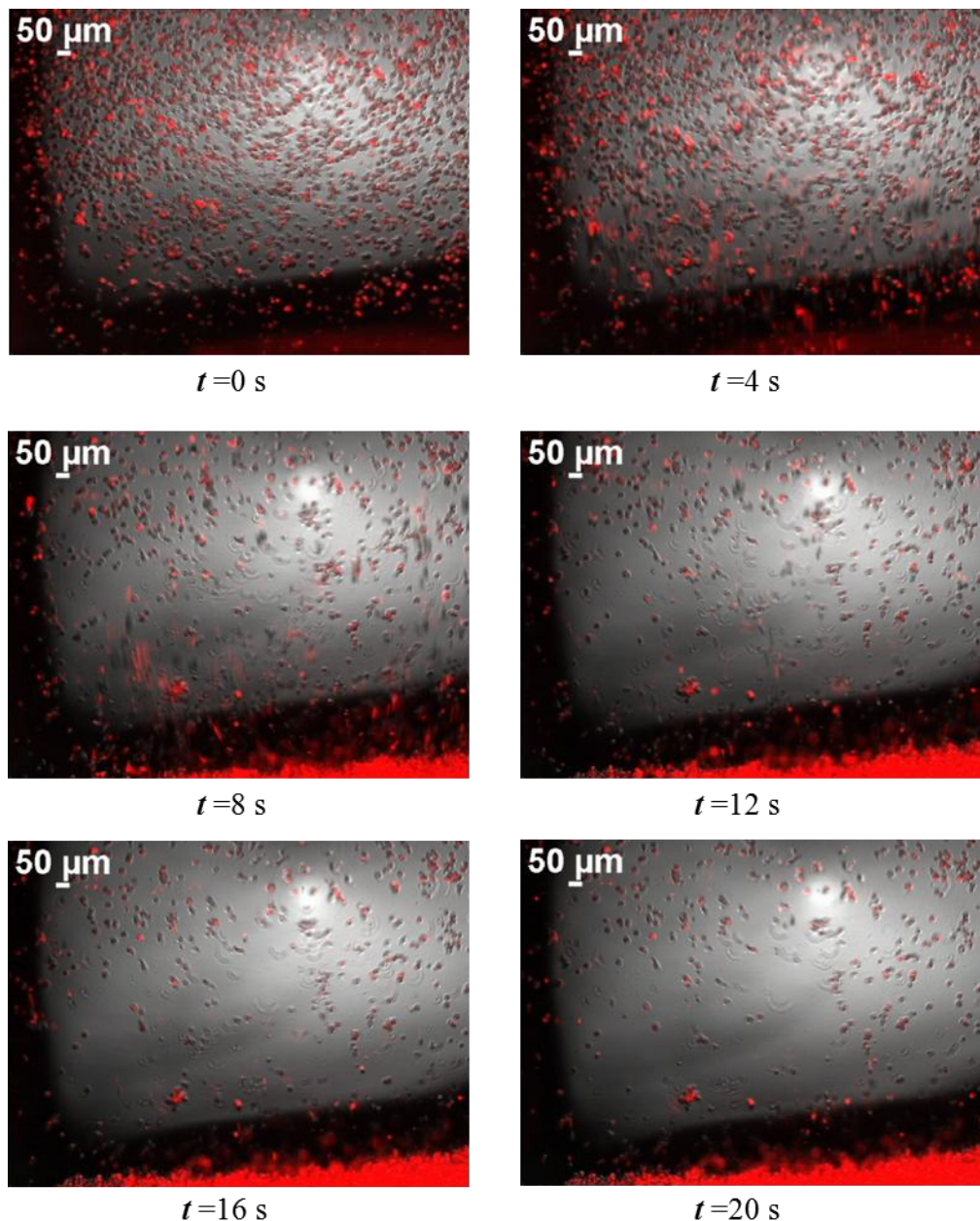


Figure 4-17. Dragging of J-774 macrophages loaded with Hybrids NanoParticles (HNPs) + 17 nm IOs.

J-774 macrophages were incubated 6 hrs. with 17 nm IOs loaded HNPs. Iron concentration in grown medium was 0.9 mM iron. Particles are stained red dye. Few μl of re-suspended macrophages were dropt on a glass coverslip and a magnet placed next. Movie was recorded in bright and red fluorescence fields. In the first frame at $t = 0$ is clearly visible the solo localization of the HNPs inside the cell area. Most of the cells were then attracted towards the magnet in the bottom of the visible area within the first 10 sec.

Similarly, few μl of suspended DPNs+5 nm SPIOs were dropped on the flow-chamber coverslip previously placed on a magnet, and left dry so as to create pre-existing, deposited aggregates. During control experiments in flow chamber without magnet (**Figure 4-18A**), these aggregates deposited beforehand decrease in their net intensity and, in some cases, also in area; per counter, application of magnet (b) (paragraph 4.2.1) on the chamber bottom produces an increase of both agglomerates area and intensity (**Figure 4-18B**). Most importantly, the incoming particles do not distribute randomly over the visible area, rather selectively deposit on pre-existing aggregates. **Figure 4-18C** reports the increase rate of the overall area covered by the original aggregates. After ~ 5 min flow, deposited MNFs cover a total area 4.1 times bigger than the area covered at $t = 0$.

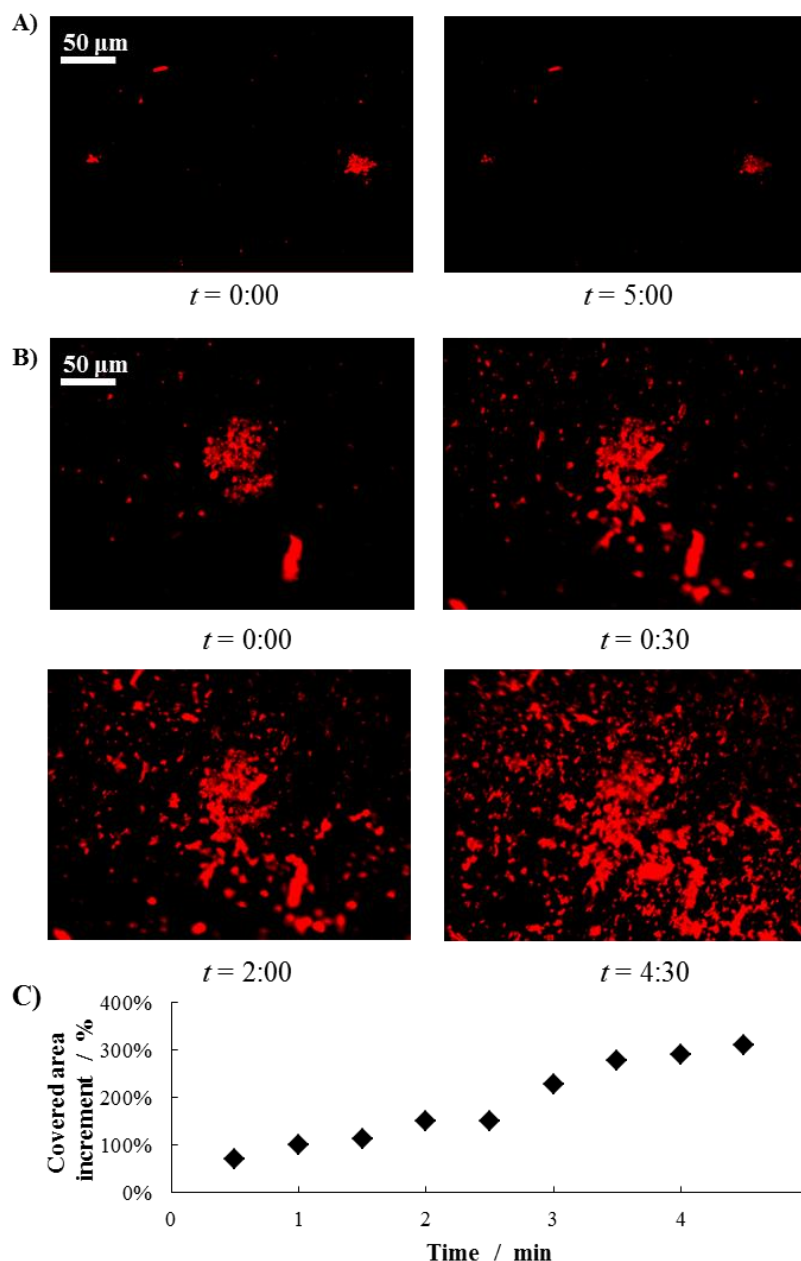


Figure 4-18. In flow accumulation experiments

(A) Two frame from the control experiment movie, with pre-deposited DPNs on the bottom floor and no magnet. Without a magnet most of the particles are carried away by the flow. Area and intensity are hence reduced. (B) From in-flow experiment with the magnet, progressive accumulation is appreciable in the reported frame at $t = 0, 0:30, 2:00$, and $4:30$. Both size and fluorescence intensity grows in time. (C) Few aggregates are taken as reference and their area monitored over 5 min flow. The charts shows continuous increase of their total area, up till 4.1-fold compare to $t = 0$.

The response of MNFs to static fields was investigated by exposing a MNF solution under flow to magnet (a), as depicted schematically in **Figure 4-19A**. The flow rate and the chamber geometry were selected to impose a fixed, physiologically-relevant wall shear rate of 100 s^{-1} [134]. As usual, the MNFs were labeled with rhodamine B and appeared as red dots under a fluorescent microscope. For undisturbed conditions, the MNFs are transported downstream by the flow following the stream lines, whereas in the presence of the external magnet, the MNFs were observed to drift laterally across the stream lines and accumulate next to the magnet forming a dense red corona, as shown in **Figure 4-19B**. The surface density of the MNFs accumulating around the magnet is shown in **Figure 4-19C** and is presented in terms of percentage of surface covered as a function of the distance y from the magnet surface. In proximity of the magnet, the deposited MNFs cover up to 60% of the available surface. Indeed, as the separation distance from the magnet increases, the surface density of deposited MNFs reduces being $\sim 5 \%$ at ~ 1.2 mm away. Note that the width of the parallel plate flow chamber is 10.0 mm, in the present configuration.

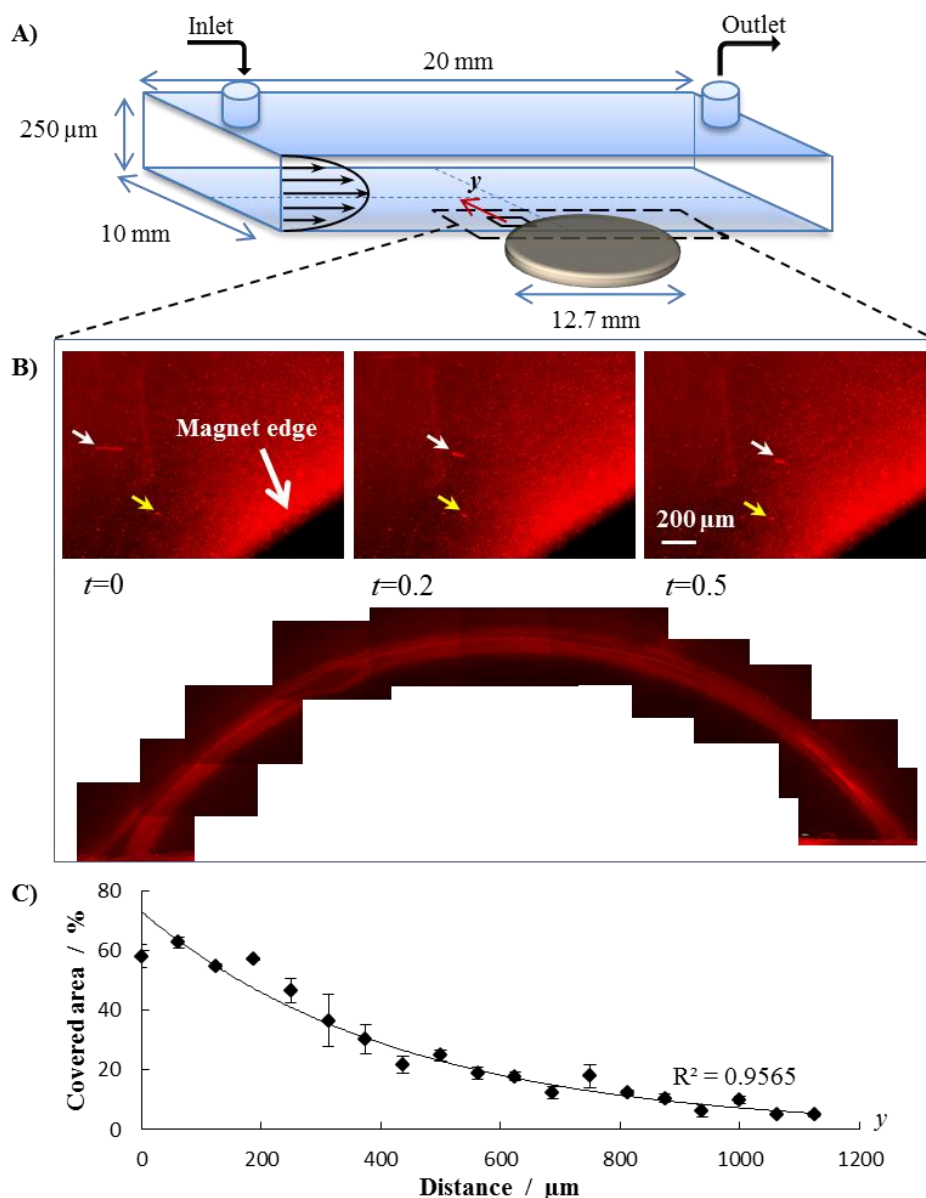


Figure 4-19. Remote guidance of the Magnetic NanoFlakes (MNFs)

(A) Schematic representation of the parallel plate flow chamber used for the experiments. (B) MNFs are stained with red dye to allow for a clear visibility at low magnification. Three individual images show the path of two particles in flow (yellow and white arrow) at three consecutive time points; also a fluorescent annulus is well recognizable around the magnet edge by the deposited MNFs after the experiment. (C) Percentage of the area covered by the deposited nanoparticles is plotted as a function of the separation distance from the magnet edge. Up to 5% of the area is still covered by MNFs at ~ 1 mm away from the magnet.

The dynamics of accumulation can also be appreciated in the brightfield image in **Figure 4-20**, clearly showing the lateral drift of MNFs. As for DPNs, even in absence of pre-formed agglomerate the first clusters deposited on the channel floor become seeds for the growth of needle-like structures; acting as a local magnet, these attract the MNFs floating in their proximity which eventually become part of a bigger aggregate. The growing direction at 70° from the horizontal flow points towards the magnet, confirming once more the particles drift.

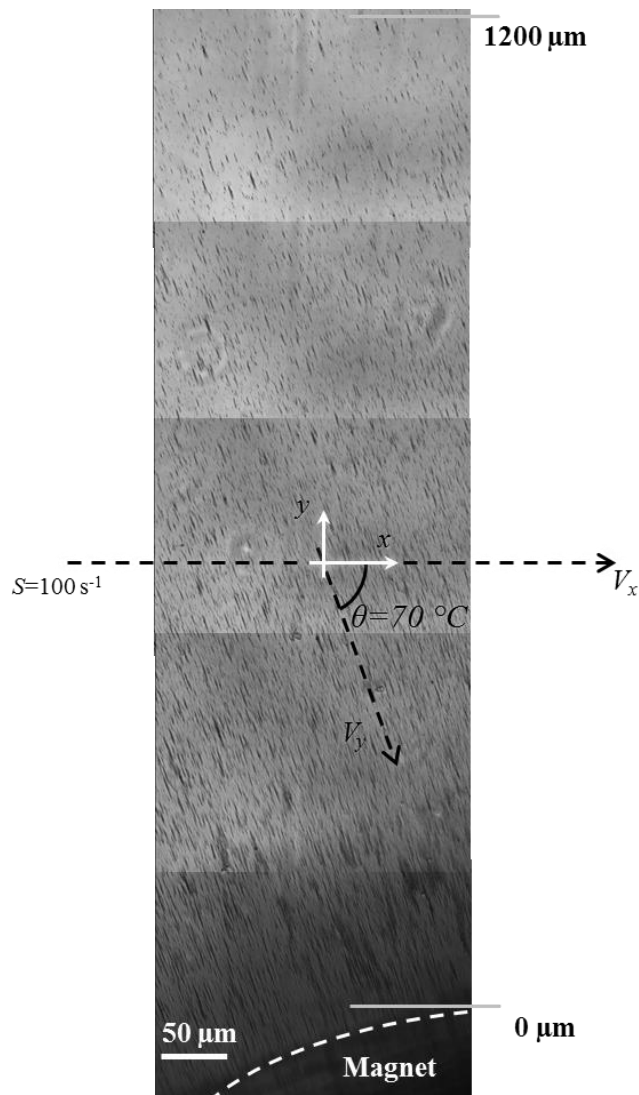


Figure 4-20. Accumulation of MNFs at the bottom of the flow chamber during flow in physiological condition.

The bright-field images shown accumulation on the channel floor up to a distance of ~ 1 mm from the magnet edge, marked by the dashed line. The flow in the channel is set as to reproduce the same physiological condition of blood flow in a healthy tissue (shear rate 100 s^{-1}), which is typically faster than the blood flow in tumor vasculature (shear rate $20 - 100 \text{ s}^{-1}$). Attracted by the magnet, MNFs considerably drift away from the horizontal flow direction and tend to accumulate on the bottom of the channel, covering $\sim 5\%$ to 60% of the visible area as the distance to the magnet reduces from 1.2 mm to 0 mm . It can be appreciated the local accumulation of several particles in bigger structure, due to mutual attraction from the local magnetization field of the MNFs.

4.3. *Relaxometric properties*

4.3.1. *Relaxivity characterization*

In order to assess the particles capacity to shorten longitudinal and transversal relaxation time T_1 and T_2 , it was used a bench-top relaxometer (mq60 “The Minispec” – Bruker Corporation) operating at 1.41 T and 37 °C. For each sample, high dilutions were required to reach required iron concentrations below 3 μMol ($\sim 1.7 \cdot 10^{-4}$ mg ml⁻¹); each dilutions are in triplicate, so as to minimize approximation errors. Longitudinal and transversal relaxation r_1 and r_2 are then calculated as:

$$r_i = \left(\frac{1}{T_i} - \frac{1}{T_i^w} \right) / [Fe] \quad [\text{mM}^{-1} \text{s}^{-1}] \quad (4-3)$$

In which T_i^w represents the proton relaxation of pure water, and T_i is for the sample.

4.3.2. *Results*

The local confinement of IOs in a porous structure as a polymer matrix has been proven to enhance the transversal relaxivity provided by a single particle. In [130], Key and co-workers using DPNs show a remarkable r_2 relaxivity increase of ~ 4.6 times if compared to the single particles. In fact, commercially available, hydrophilic 5 nm IOs had shown an intrinsic transversal relaxivity of $107 \pm 24 \text{ mM}^{-1} \text{ s}^{-1}$, whereas 1 μm DPNs loaded with the same particles reached values of $495 \pm 36 \text{ mM}^{-1} \text{ s}^{-1}$. In comparison, the low

r_1 for free ($8 \pm 1 \text{ mM}^{-1} \text{ s}^{-1}$) and constrained ($6 \text{ mM}^{-1} \text{ s}^{-1}$) iron oxides confirms their quality as T_2 contrast agents.

Similarly, MNFs were also characterized for their quality as T_1 and T_2 contrast agents. Compared to pure water, relaxometric measurements report a $\Delta T_1 = 473 \pm 47.1 \text{ s}$ and a $\Delta T_2 = 2242 \pm 49 \text{ s}$; these correspond to a longitudinal relaxivity r_1 of $4.98 \pm 0.58 \text{ (mM s)}^{-1}$ and a transversal relaxivity r_2 of $475 \pm 28 \text{ (mM s)}^{-1}$. The iron concentration is measured to be $0.15 \text{ } \mu\text{g ml}^{-1}$, via ICP-OES. Note that since the individual NCs are coated with a single layer of oleic acid (i.e. are hydrophobic) and the relaxometric properties depend on the surface chemistry of the nanoparticles, the r_2 for the individual NCs could not be estimated for a direct comparison.

Figure 4-21 compares the relaxometric performances of the different particles; it is interesting to note the capacity of MNFs, which are $\sim 140 \text{ nm}$ in diameters, to perform comparably to DPNs, which are several times bigger ($\sim 1 \text{ } \mu\text{m}$).

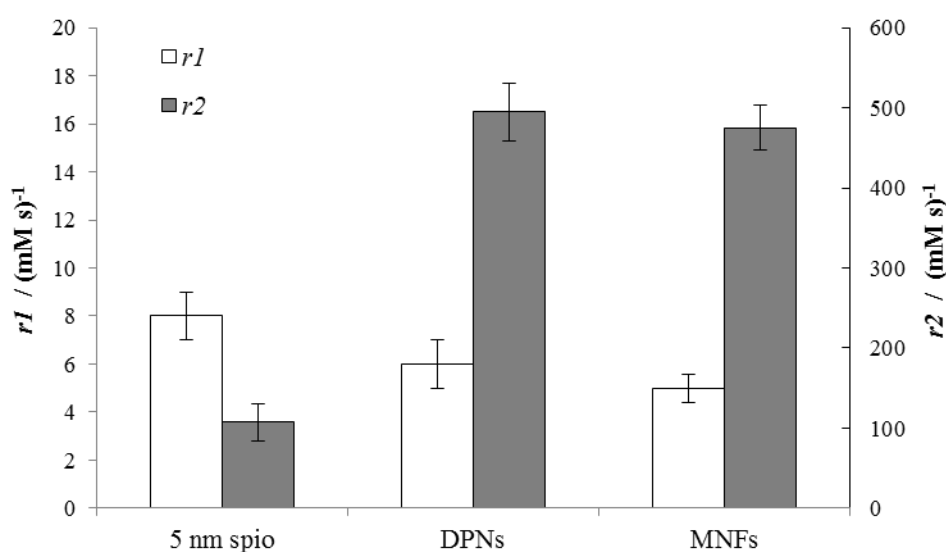


Figure 4-21. Relaxometry performance of free Iron Oxides (IOs) free and loaded inside Discoidal Polymeric Nanoconstructs, and Magnetic NanoFlakes (MNFs).

The bar chart shows the efficacy of local confinement of the SPIOs inside a bigger construct. In the latter, in fact, an enhancement of ~ 4.6 times compared to the case of free particles is achieved. 5 nm iron oxides show an intrinsic transversal relaxivity of $107 \pm 24 \text{ mM}^{-1} \text{ s}^{-1}$, whereas $1 \mu\text{m}$ DPNs loaded with the same particles reach values of $495 \pm 36 \text{ mM}^{-1} \text{ s}^{-1}$. In comparison, the low r_1 for free ($8 \pm 1 \text{ mM}^{-1} \text{ s}^{-1}$) and constrained ($6 \text{ mM}^{-1} \text{ s}^{-1}$) iron oxides confirms their quality as T_2 contrast agents.

4.4. Thermal ablation properties: in-vitro and preliminary in-vivo experiments

In-vitro characterizations of the heating performances for the synthesized nanoconstructs followed procedures previously described for the scope. A preliminary work on animal model bearing a breast tumor was developed based on the results discussed in the previous chapters.

4.4.1. Animal studies

Tumor model

All animal protocols was reviewed and approved by Animal Protocol Review Committee at the The Methodist Hospital Research Institute, Houston, TX. The same institution provided the mouse for the experiment. Tumor model was initially generated by xenograft transplantation of patient human breast cancer tumor MC1 in the #4 mammary gland and grown for about 1 month prior treatment, to a size of $\sim 500 \text{ mm}^3$

Particles injection

The tumor was treated with MNFs a 2 hrs ahead the magnetic hyperthermia treatment, such to allow the particles to permeate from the injection site to its proximities. From 9 to 10 injections, for a total of 100 μl , were performed around the whole volume of the tumor. Iron concentration in the sample was $\sim 2.6 \text{ mg ml}^{-1}$. The same procedure was repeated on day 1 and day 9 of the treatment.

Hyperthermia treatment

On the days of injections, and the following 2 days, the mouse was exposed for 30 min to alternated magnetic fields at a frequency of 298.5 kHz. The field strength was modulated to 35 kA m⁻¹ for the first 20 min, than raised to 45 kA m⁻¹ for the remaining 10 min of the treatment.

4.4.2. *In-vitro* characterization

The magnetization properties of the MNFs are presented in **Figure 4-22**. Using the SQUID magnetometer previously described (paragraph 3.1), the magnetization M_s of the nanoconstructs was measured as a function of the external applied field H . The data of **Figure 4-22A** demonstrate the lack of any hysteresis loop and a magnetization saturation of ~80 emu g⁻¹, which is comparable with the values obtained in literature. However, with a susceptibility of ~0.21, the present MNFs tend to have a lower rate of magnetization at low fields if compared with the NCs synthesized in [63, 123, 135].

The ablation properties of the MNFs were derived by exposing the nanoconstructs to an alternating magnetic field (AMF) and registering the temperature variation of the sample over time. In particular, a vial containing an aqueous solution (0.6 ml) of magnetic nanoflakes (0.76 mg ml⁻¹) was exposed to an AMF (512 kHz, 10 kA m⁻¹), showing an increase in temperature of ~6 °C within 30 min of treatment (**Figure 4-22B**). The experiment was repeated 5 times with very small variations in temperature.

Following the protocols described in 3.3.2, from the temperature-time curve the specific absorption rate (*SAR*) of the MNFs is quantified to be $73.8 \pm 2.3 \text{ W g}^{-1}$. This value is ~ 60 time larger than the *SAR* measured for the individual NCs in ethanol (tested at 0.94 mg ml^{-1}), which is measured to be $1.25 \pm 0.12 \text{ W g}^{-1}$. The corresponding *ILP* values are $0.024 \pm 0.002 \cdot 10^{-9} (\text{m}^2 \text{ s}^{-1} \text{ A}^{-1})^2$ and $1.44 \pm 0.045 \cdot 10^{-9} (\text{m}^2 \text{ s}^{-1} \text{ A}^{-1})^2$ for singles NCs and MNFs, respectively. These data are presented in the bar chart of **Figure 4-22C**. The significant enhancement in the heating performance should be attributed to the geometrical confinement of the NCs within the polymeric matrix.

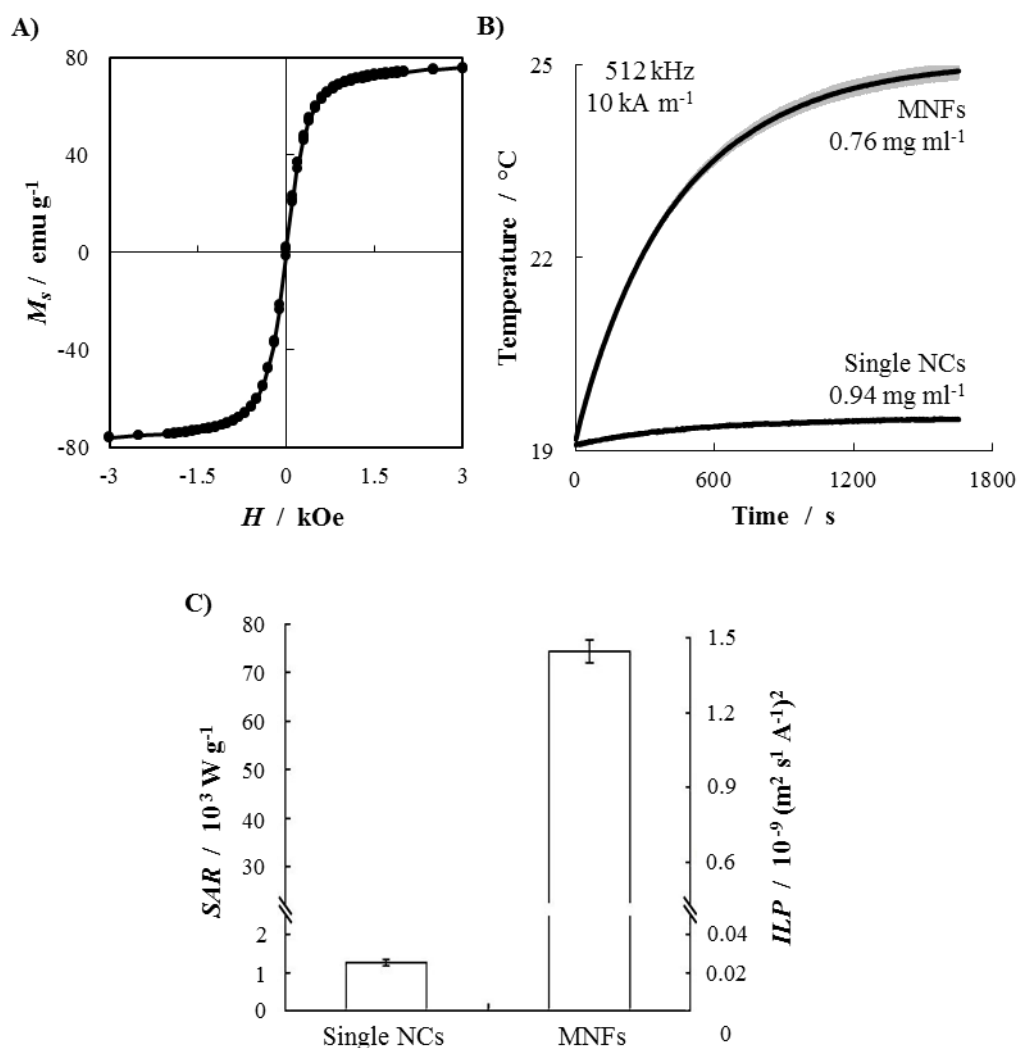


Figure 4-22. Magnetic properties of the Magnetic NanoFlakes (MNFs)

(A) SQUID analysis of cycle magnetization shows the lack of hysteresis loop and a magnetization saturation of $\sim 80 \text{ emu g}^{-1}$. (B) Temperature increase over time for two 0.6 ml solutions of MNFs (0.76 mg ml^{-1}) and NCs (0.94 mg ml^{-1}) exposed to an alternating magnetic field ($512 \text{ kHz} / 10 \text{ kA m}^{-1}$ AMF) for 30 min; solid black line indicates the average over 5 repetitions, and the grey shadow the standard deviation. (C) Bar chart comparing the hyperthermia related values of single NCs / MNFs nanoconstruct: $\text{SAR} = 1.25 \pm 0.12 / 73.8 \pm 2.3 \text{ W g}^{-1}$; $\text{ILP} = 0.024 \pm 0.002 \cdot 10^{-9} / 1.44 \pm 0.045 \cdot 10^{-9} (\text{m}^2 \text{ s}^{-1} \text{ A}^{-1})^2$. Note that encapsulated nanocubes (NCs) in MNFs show performances as ~ 60 times larger than that free ones.

4.4.3. Preliminary in-vivo test on small animal

Preliminary work on the tumoritopic efficacy of MNFs was conducted on a small animal subject. The mouse was injected in the #4 mammary gland with a human MC1 patient-derived breast tumor; the tumor was allowed to grow for about 1 month before starting the treatment. Several 10 μl injections of MNFs were performed around the whole tumor volume to better distribute the particles. Based on the design map in **Figure 3-15** and on **Equation (3-3)**, with $H_0 = 35 \text{ kA m}^{-1}$ and $f = 300 \text{ kHz}$, the concentration of MNFs required to reach an efficient hyperthermia ($42 \text{ }^\circ\text{C}$) is calculated to be 1.9 mg ml^{-1} , whilst an ablation treatment would requires ($50 \text{ }^\circ\text{C}$) is 5.1 mg ml^{-1} . Hence, MNFs were injected at an iron concentration of $\sim 2.6 \text{ mg ml}^{-1}$, also considering tissues permeation of the fluid upon injection.

After about 2 hrs following the injections, the mouse was placed inside the high power hyperthermia apparatus described in section 3.2.3, with the tumor at the center of the coil (**Figure 4-23A** and **B**). Hyperthermia was performed at $\sim 35 \text{ kA m}^{-1}$ for about 20 min; then the power was increased up to 45 kA m^{-1} in the last 10 min; frequency of the AMF was kept stable at $\sim 300 \text{ kHz}$. Exposure to magnetic field was repeated for 3 consecutive days; particles injection and treatment were identically repeated a week after the first injection. The mouse and its tumor were monitored for about 4 weeks, and then sacrificed.

Temperature increase of the tumor is reported in **Figure 4-23C**. The temperature recorded by the nIR camera reaches a first equilibrium around $36.5 \text{ }^\circ\text{C}$ after $\sim 10 \text{ min}$ of exposure at 35 kA m^{-1} ; instead, a second plateau is

still not seen 10 min after increasing the field to 45 kA m^{-1} . The maximum temperature reached within the 30 min of exposure is $42.9 \text{ }^\circ\text{C}$, in the two points indicated by the arrows in **Figure 4-23A** and **B**. These points present a minor quantity of hairs compared to the rest of the tumor area, which definitely affect the camera reading. Hence, it can be deducted that the overall area of the tumor reaches a higher temperature than what actually recorded; also, most probably the inner volume of the tumor reaches a temperature few degrees higher than the recorded 36.5 or $43 \text{ }^\circ\text{C}$.

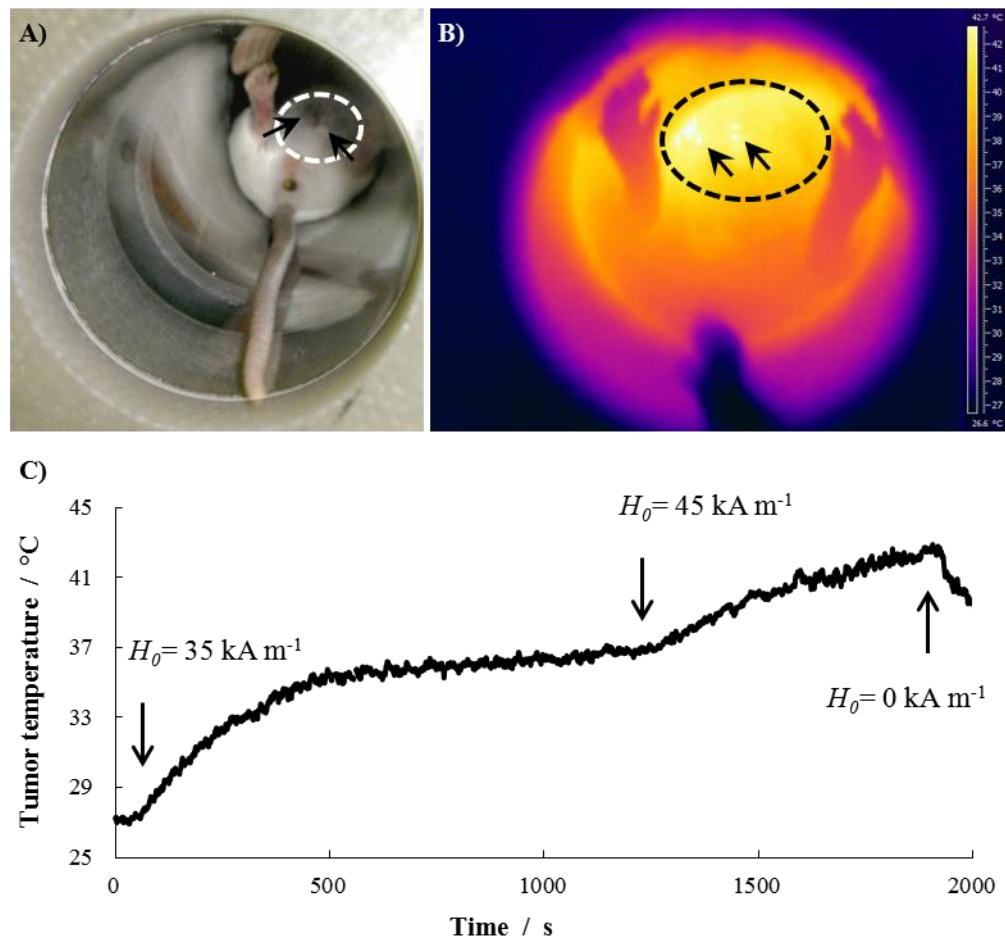


Figure 4-23. Tumor exposure to magnetic field.

The mouse was placed such that tumor can be at the center of the coil developing the magnetic field. The dashed line highlights the tumor in the visible-light picture (A) and in the infra-red picture (B); the arrows points to the same spots in both the pictures, which results in the highest temperature ($\sim 43 \text{ }^\circ\text{C}$) during the whole treatment. These have few hairs compared to the rest of the tumor, which can explain the higher temperature detected; at the same time this suggests the inner temperature of the tumor is actually higher than what indicated by the camera; (C) Temperature profile of the tumor over 20 min of exposure at $\sim 35 \text{ kA m}^{-1}$ and then $\sim 45 \text{ kA m}^{-1}$ for the remaining 10 min. At the 30th minute of exposure the temperature did not reach equilibrium yet.

Before the treatment the tumor was measured to be ~1.4 cm in length and 1.1 cm in width (see **Figure 4-24**). For the first three days during hyperthermia treatments the tumor length seen a small reduction, but its width increased. During the following days without further treatments, both width and length were stable around 1.25 cm and neither increase nor reduction can be appreciated. A second injection and second cycle of exposures to AMF had similar results showing neither increase nor reduction of tumor size. It was also observed that on day 1 the tumor felt stiff on touch, whilst on day 3 it was considerably softer. This can indicate a decreasing volume of necrotic tissues as results of the treatment. The tumor remained stable up to the end of the 3rd week. On the 10th days from the last treatment (day 21) the tumor started to grow again and the animal was sacrificed on the 16th day (day 27).

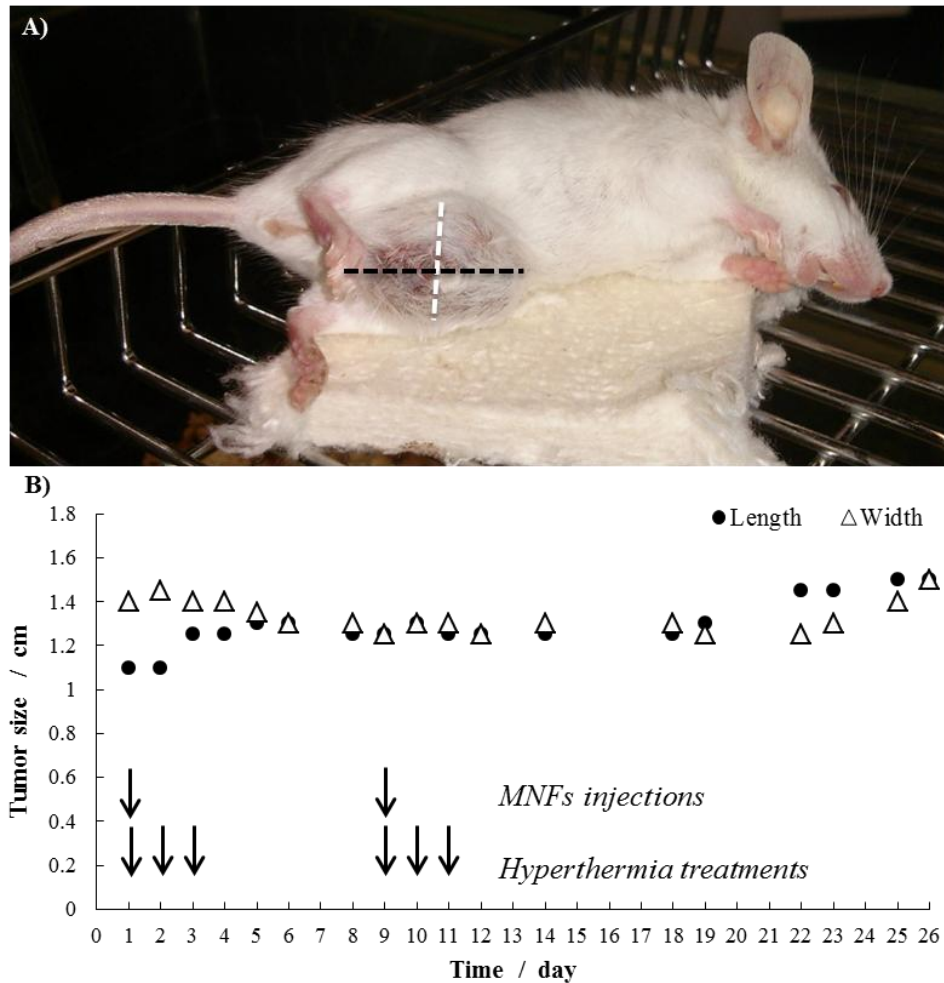


Figure 4-24. Tumor size during preliminary hyperthermia treatment with MNFs.

(A) The mouse on day 1. MC1 patient-derived breast tumor xenograft were grown on the mouse #4 mammary gland (orthotropic); its sizes are measured on the white (width) and black (length) dashed line reported. (B) The mouse is injected with MNFs on day 1 and day 9, and subdued hyperthermia treatment at $\sim 40 \text{ kA m}^{-1}$ and 300 kHz on each injection day and following for 2 days. Measured length of the tumor starts at 1.4 cm and is slightly decreasing to 1.25 cm in the first five days; in the same period the width increases from 1.1 cm to 1.25 cm and both reach a steady state after about a week. On average, the tumor shows no further increase during the treatment period and both the sizes oscillate between 1.2 and 1.25 cm till the third week. 10 days after not receiving treatments the tumor started to grown again.

4.5. Comparison with conventional SPIOs and iron oxide nanocubes

Dragging

Polymeric nanoconstructs are exploited to maximize the iron density in a defined geometry, and test the accumulation potential in flow conditions; a second hypothesis of this study was that the generated magnetization field of magnetic aggregate is capable to capture the particles flowing in its proximities.

Experiments performed in physiological relevant conditions (microfluidic flow channel with shear rate $S = 100 \text{ s}^{-1}$) demonstrate a cooperative accumulation of DPNs and MNFs particles. Next to the magnet, externally applied to the region of interest, local accumulation of polymer based nanoconstructs increases at least 12 times. It is worth to be noted that accumulation rates would be further increased in tumors, due to the lower shear rate of a typical neoplastic vasculature. At the author knowledge, similar improvement in local accumulation has not yet been demonstrated for application of the kind.

Nanoparticles injected through systemic administration typically result in excessive accumulations in liver or spleen, and a minimal percentage make its way to the tumor [97]; this corresponds to a higher intoxication for the patient and a huge loss of curative efficacy. The results achieved here are a promising first step towards the leveraging of this unbalance relationship. Additionally, in a preliminary study IOs loaded HNPs attracted by the

magnetic field successfully managed to move J-774 macrophages that have these particles internalized.

Relaxometry

The group of Hyeon [135] has shown that single, 22 nm NCs can provide transversal relaxivities r_2 as high as 761 (mM s)^{-1} (**Figure 4-25A**). Importantly, this large relaxivity value has been never demonstrated for clustered NCs. Here, polymeric architectures are exploited for their capacity to assure the water diffusivity with the inner IOs core. $1 \mu\text{m}$ sized discoidal particles were able to enhance the relaxometric property of the single spherical particle entrapped in their core; similar values of transversal relaxivity r_2 are also achieved with much smaller nanoconstructs ($\sim 140 \text{ nm}$) starting from cubic shaped iron oxides. This shows that remarkably high relaxivities can also be achieved by forming proper clusters of NCs.

Both DPNs and MNFs shows a transversal relaxivities r_2 around $485 \text{ mM}^{-1} \text{ s}^{-1}$, which is only 40% smaller than what been measured by Hyeon for individual NCs. This value is significantly larger than that offered by other IOs and IO-based systems, such as the FIONs ($r_2 = 324 \text{ mM}^{-1} \text{ s}^{-1}$), MPIOs ($r_2 = 169 \text{ mM}^{-1} \text{ s}^{-1}$), and the Feridex nanoparticle ($r_2 = 133 \text{ mM}^{-1} \text{ s}^{-1}$). This transversal relaxivity is also larger than that documented for clusters generated with conventional spherical IOs. For instance, the group of Simard had demonstrated a r_2 up to $400 \text{ mM}^{-1} \text{ s}^{-1}$ [115]; whereas the group of Morales had obtained r_2 up to $\sim 300 \text{ mM}^{-1} \text{ s}^{-1}$ [116]. It is then possible that even larger relaxivities can be achieved by packing NCs in the same polymeric matrix.

Heating

The *SAR* is a dosimetric quantity that has been introduced for assessing the amount of absorbed radiation power by unit mass of particle. It depends on the operating conditions of the AMF apparatus used for stimulating the IOs, namely the frequency f and field strength H_0 . *SAR* is proportional to $H_0^2 \cdot f$ therefore a meaningful comparison for the ablation properties among different nanoparticles can only be performed if the individual *SAR* are normalized by $H_0^2 \cdot f$. Based on these considerations, the intrinsic loss power (*ILP*) has been introduced as more efficient index to compare particles tested in different conditions (section 2.5).

Consequently, the *SAR* of $\sim 2'500 \text{ W g}^{-1}$ reported by Pellegrino&Gazeau group [63] ($f = 520 \text{ kHz}$ and $H_0 = 29 \text{ kAm}^{-1}$) correspond to an *ILP* of $\sim 5.6 \cdot 10^{-9} (\text{m}^2 \text{ s}^{-1} \text{ A}^{-1})^{-2}$. Similarly, the *ILP* values for 5 nm SPIOs and the Feridex nanoparticles would be equal to $\sim 0.39 \cdot 10^{-9}$ and $\sim 0.17 \cdot 10^{-9} (\text{m}^2 \text{ s}^{-1} \text{ A}^{-1})^{-2}$, respectively. The magnetic nanoflakes here developed present a *SAR* of $1.44 \pm 0.045 \cdot 10^{-9} \text{ W g}^{-1}$. Although the *ILP* of the MNFs is ~ 4 times lower than that measured by Pellegrino&Gazeau's group, it still results to be 4 to 15 times larger than the *ILP* depicted for more conventional systems (see **Table 2-2** and **Figure 2-6**). The difference in *ILP* between the MNFs and the Pellegrino&Gazeau's NCs can be attributed to the different magnetic behavior of the individual NCs. In particular, the magnetic susceptibility of the Pellegrino&Gazeau's NCs is at least two times larger than that of the NCs used here, and of all other IO formulations (**Figure 4-25B**). The bar chart also confirms that *ILP* and magnetic susceptibility are directly related. Since the

ILP of the MNFs is 60 times larger than that of the oleic acid-coated NCs ($0.024 \pm 0.002 \cdot 10^{-9} (\text{m}^2 \text{s}^{-1} \text{A}^{-1})^2$), it is reasonable to speculate that even larger *ILP* could be reached for the MNFs by confining NCs exhibiting higher magnetic susceptibility.

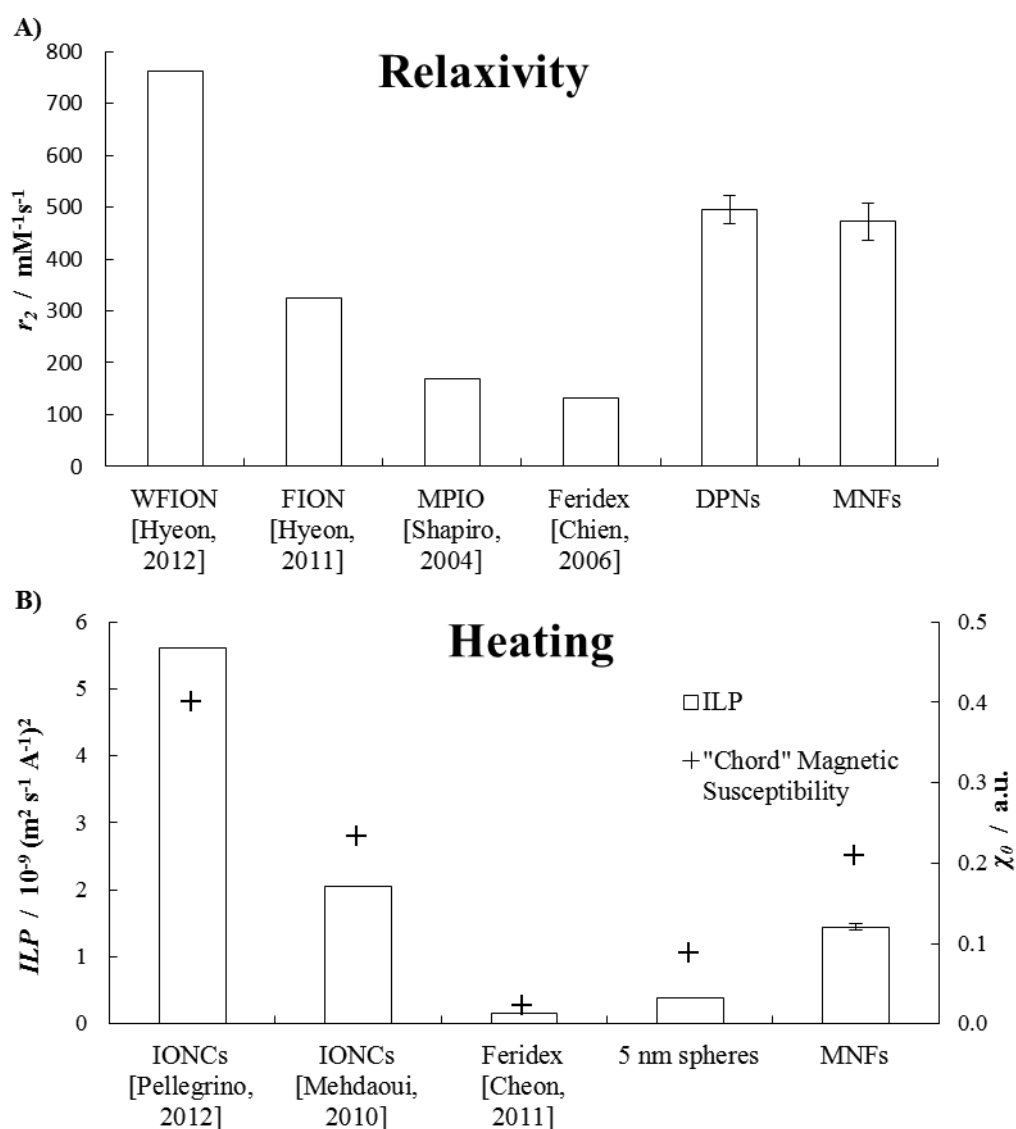


Figure 4-25. Polymeric particles performances compared to literature.

(A) Transversal relaxivity r_2 of the MNFs and DPNs compared to other iron oxide nanocubes and nanoparticles presented in the open literature. (B) Comparison of the intrinsic loss power (bar chart) and the magnetic susceptibility (crosses) between MNFs and the best performing IOs nanocubes reported in literature.

Summarizing, the presented data demonstrate that a construct highly performing in several fields can be obtained with a properly designed nanoconstruct based on superparamagnetic nanoparticles. In particular, that newly synthesized magnetic nanoflakes can combine together: (i) a remarkably high relaxivity (475 ± 28 (mM s)⁻¹); (ii) specific absorption rate (73.8 ± 2.3 W g⁻¹, at $f = 512$ kHz and $H_0 = 10$ kAm⁻¹); (iii) high local accumulation rates next to an applied magnet upon systemic injection (at least 12 times). The synthesis of this nano-construct successfully achieved the aim of merging together cut-edge performances that cannot be simultaneously achieved by using either individual NCs or IO nanospheres.

Last, a trial experiment for *in-vivo* hyperthermia was designed based on the results achieved in the previous chapters and other investigators procedures [49, 136, 137]. The MNFs particles show a superficial maximum temperature of 42 °C, still increasing. Despite this value is not enough to trigger an efficient treatment, no appreciable tumor growth is noted up to 10 days after the last treatments, and for a total of 3 weeks; from the 4th week the tumor started to grow again with an overall rate of 0.24 mm³ per day. As well, in the first period the tumor was not decreasing, which suggests an overall mild hyperthermia. Based on the design map defined at the end of the previous **Chapter. 3** and on the linear response theory, the concentration required for an effective hyperthermia should be at least 1.9 mg ml⁻¹; MNF iron concentration upon injection was no more than 2.6 mg ml⁻¹, and good chances are that actual concentration decreases in the time between injection and the treatment, due to tissue permeabilization. This result was therefore expected.

5. Conclusions and future works

In relation to a rational design of nanoconstructs for thermal treatment, definitions of comparative parameters that could be valid in different operative conditions were investigated. The available theory for superparamagnetic power loss was analyzed on its dependence on applied field, and magnetic properties of particles. Intrinsic Loss Power (*ILP*) is proposed as better suitable substitute for the more common Specific Absorption Rate (*SAR*). This choice is then investigated and validated within ranges typical of biomedical applications (**Figure 2-5**). Evaluations of various literature materials also confirms the efficiency of *ILP* in comparing heating performances of different particles tested in diverse experimental conditions (**Figure 2-6**). These considerations also indicate a clear decoupling in the design between the magnetic field, as hyperthermia generator, and the employed nanodevice, as treatment actuator.

Three commercially available formulations of superparamagnetic iron oxide nanoparticles (SPIOs) were characterized for their hyperthermic performance using Alternating Magnetic Fields (AMFs) with field strength H_0 ranging from 0.2 - 30 MHz and frequency f ranging from 4 - 10 kA m⁻¹, respectively. The three formulations had different magnetic core diameters (5, 7, and 14 nm) and the nanoparticles surfaces were coated with short PEG chains. The absolute temperature increase ΔT and specific absorption rate *SAR* were measured under different AMF operating conditions. In the high frequency regime (30 MHz) non-specific heating, associated with salts dispersed within the sample solution, dominated; a mild SPIO-induced heating

is detected only at physiological and supra-physiological salt concentrations (≥ 150 mM). At lower frequencies (≤ 1 MHz) heating is solely generated by the relaxation of SPIOs while no heating is measured for control, salt solutions. The undesired, non-specific heating generated at high frequency goes in the same direction (and suggests explanation) of the well-known limitation for fH_0 first proposed by Atkinson [94], in 1984. Still, as stated in the same paper, this threshold is more of a general suggestion than a strict limit. Until a dedicated investigation clarifies the effective boundaries, this local heating can be synergistically exploited to enhance local sensitivity to other treatments.

A mathematical model, based on the finite element discretization of the bio-heat equation, was developed to predict the increase over time of the temperature field in a biological tissue. From this, two scaling laws in the form $c_{MNP} \times SAR_{MNP}^a \geq b$ are derived to identify minimum requirements for local hyperthermia ($T_{tissue} > 42$ °C; $a = 1.0616$, $b = 2.2714 \times 10^6$ W m⁻³) and thermal tissue ablation ($T_{tissue} > 50$ °C; $a = 1.0737$, $b = 7.1565 \times 10^6$ W m⁻³). The resulting design maps (**Figure 3-15**) can be used to rationally design hyperthermic treatments and select the proper route of administration – systemic *versus* intratumor injection –, which depends on magnetic properties and bio-distribution performance of nanoparticles. This map makes a pair together with the indications defined by the linear response theory and reported in **Figure 2-7**. These are overall and general comprehensive guidelines of the most influencing parameters, and should be used in the rational design of an efficient hyperthermic treatment. The guidelines and the stated aspects are valid for every superparamagnetic assembly including the

SPIOs nanoparticles, but not limited to these. Additionally, based on experimental results obtained from *in-silico* simulations, one could suggest that tumor tissue ablation can be feasible also via the systemic administration of nanoparticles provided that sufficient local accumulation is met. In order to achieve the required quantities, strategies as surface targeting or directed magnetic gradient can be employed. As secondary effect this strategy would also reduce non-specific bio-distribution and off-target toxicity.

To fully exploit the intrinsic potential of SPIOs as multifunctional nanoparticles, new magnetic nanoconstructs – Magnetic NanoFlakes (MNFs) – were derived. By geometrically confining iron oxide nanocubes of ~22 nm in edge within a polymeric matrix of deoxy-chitosan, MNFs demonstrates merged functionality in heating, MRI imaging contrast, and magnetically targeted accumulation. Following such a strategy, a remarkably high transversal relaxivity ($r_2 = 475 \pm 28 \text{ (mM s)}^{-1}$ at 1.41 T) and specific absorption rate ($SAR = 73.8 \pm 2.3 \text{ W g}^{-1}$, at $f = 512 \text{ kHz}$ and $H_0 = 10 \text{ kAm}^{-1}$, $ILP = 1.44 \pm 0.045 \cdot 10^{-9} \text{ (m}^2 \text{ s}^{-1} \text{ A}^{-1})^2$) are achieved for the same nanoconstructs. Preliminary *in-vivo* study confirmed the generation of mild hyperthermia by using MNFs. This result was expected, based on the design map shown earlier.

Significant enhancement in magnetic properties from individual NCs is also confirmed resulting from their geometrical confinement within the polymeric matrix. In particular, the SAR/ILP of MNFs has a ~60-fold increase compared to individual NCs ($1.25 \pm 0.12 \text{ W g}^{-1} / 0.024 \pm 0.002 \cdot 10^{-9} \text{ (m}^2 \text{ s}^{-1} \text{ A}^{-1})^2$). The geometrical confinement of NCs exhibit higher magnetic properties,

particularly in terms of magnetic susceptibility and saturation that lead to higher SAR and r_2 values. Also, in physiologically relevant conditions, the denser magnetic core improves their local accumulation (~12-fold) compared to areas without magnet nearby. Requirements for systemic administration with a limited non-specific accumulation seem therefore closer in being satisfied. Another interesting aspect is the cooperation function of MNFs in recruiting other particles during magnetic accumulation.

The goal of merging together cutting-edge performances in a single nanoconstruct was successfully achieved. The synthesis of this nano-construct shows potentials that cannot be met by using either individual iron oxide nanocubes or -spheres. Nevertheless it represents a first step towards the realization of nanoconstructs with superior theranostic capabilities.

Future works

A complete, optimal design of heat-focused nanodevices for tumor treatments must include analysis on more parameters. A final model describing the shape influence on power lost is still missing. Indeed, it is confirmed that cubic iron oxides (IOs) perform better compared to spherical counterparts with comparable size. However, the reason remains a matter of discussion. Mathematical models for theoretical predictions (modeling) of these enhancements would significantly reduce the required concentration for an effective local hyperthermia. Other investigations should also consider synergy with other co-adjuvant treatments and patient-specific considerations.

Also, the only available method to test particle efficiency is by indirect recording of overall temperature in diffused media which generate

inaccuracies. A very elegant solution to this problem was recently proposed by the group of Pellegrino [138]. This method can be used for temperature mapping at a single particle level, during AMF exposure; this would allow a better characterization of particles heating properties and, most importantly, unleash direct observation and validation of proposed mathematical models.

As for Magnetic NanoFlakes (MNFs) synthesis process, it only represents a very first step in the development of a proper multifunctional nanodevice. An optimization process will include testing of different polymer, loaded with drug for a triggered release, and also test effect of surface functionalization. Additionally while enhancement in *SAR* has been quantified, corresponding changes or enhancement in relaxivity is yet to be investigated. Finally, it should be verified that similar levels of enhancements of particles performances can be reproduced using different SPIOs formulations.

Dragging of macrophages, which have internalized IOs loaded HNPs, is successfully achieved in a preliminary study. This suggests that properly targeted particles can be used as drivers to lead bigger cells on specific routes, and/or promote interactions between bigger bodies.

Proper *in-vivo* studies will continue testing the MNFs particles to improve accumulation (histology tests and organs post-digestion), imaging capabilities (direct MRI imaging), and to further enhance hyperthermia treatment.

6. References

1. Feynman, R.P., *There's plenty of room at the bottom*. Engineering and Science, 1960. **23**(5): p. 22-36.
2. Taniguchi, N. *On the basic concept of nanotechnology*. in *Proc. Intl. Conf. Prod. Eng. Tokyo, Part II, Japan Society of Precision Engineering*. 1974.
3. Kroto, H.W., et al., *C 60: buckminsterfullerene*. Nature, 1985. **318**(6042): p. 162-163.
4. Drexler, K.E., *Engines of Creation: The Coming Era of Nanotechnology*. 1986: Doubleday.
5. Li, X.-M., D. Reinhoudt, and M. Crego-Calama, *What do we need for a superhydrophobic surface? A review on the recent progress in the preparation of superhydrophobic surfaces*. Chemical Society Reviews, 2007. **36**(8): p. 1350-1368.
6. Karn, B., T. Kuiken, and M. Otto, *Nanotechnology and in situ remediation: a review of the benefits and potential risks*. Environmental Health Perspectives, 2009. **117**(12): p. 1813.
7. Pacheco-Torgal, F. and S. Jalali, *Nanotechnology: advantages and drawbacks in the field of construction and building materials*. Construction and building materials, 2011. **25**(2): p. 582-590.
8. Lu, W. and C.M. Lieber, *Nanoelectronics from the bottom up*. Nature Materials, 2007. **6**(11): p. 841-850.
9. Enzo, M.V., *Analysis of Blood-Based Markers as Predicting Tools of Pathologic Tumour Response in Rectal Cancer Patients Receiving Neo-Adjuvant Chemoradiotherapy*, in *Department of Surgical, Oncological and Gastroenterological Sciences 2013*, University of Padova.
10. Bettinger, C.J., R. Langer, and J.T. Borenstein, *Engineering Substrate Topography at the Micro- and Nanoscale to Control Cell Function*. Angewandte Chemie International Edition, 2009. **48**(30): p. 5406-5415.
11. Ruoslahti, E., S.N. Bhatia, and M.J. Sailor, *Targeting of drugs and nanoparticles to tumors*. The Journal of Cell Biology, 2010. **188**(6): p. 759-768.
12. Ferrari, M., *Frontiers in cancer nanomedicine: directing mass transport through biological barriers*. Trends in Biotechnology, 2010. **28**(4): p. 181-188.
13. Goldberg, M., R. Langer, and X. Jia, *Nanostructured materials for applications in drug delivery and tissue engineering*. Journal of Biomaterials Science, Polymer Edition, 2007. **18**(3): p. 241-268.
14. Hu, Y., et al., *Nanodevices in diagnostics*. Wiley Interdisciplinary Reviews: Nanomedicine and Nanobiotechnology, 2011. **3**(1): p. 11-32.
15. Godin, B., et al., *Multistage nanovectors: from concept to novel imaging contrast agents and therapeutics*. Accounts of Chemical Research, 2011. **44**(10): p. 979-89.

16. Mamo, T., et al., *Emerging nanotechnology approaches for HIV/AIDS treatment and prevention*. *Nanomedicine (Lond)*, 2010. **5**(2): p. 269-85.
17. Vauthier, C., N. Tsapis, and P. Couvreur, *Nanoparticles: heating tumors to death?* *Nanomedicine*, 2011. **6**(1): p. 99-109.
18. Gazeau, F., M. Lévy, and C. Wilhelm, *Optimizing magnetic nanoparticle design for nanothermotherapy*. *Nanomedicine*, 2008. **3**(6): p. 831-844.
19. Baronzio, G.F. and E.D. Hager, *Hyperthermia in cancer treatment: a primer*. 2006: Springer.
20. Frey, E.F., *The earliest medical texts*. *Clio Med*, 1985. **20**(1-4): p. 79-90.
21. Adams, F., *The genuine works of Hippocrates*. Vol. 1. 1886: W. Wood and company.
22. Glazer, E.S. and S.A. Curley, *The ongoing history of thermal therapy for cancer*. *Surgical oncology clinics of North America*, 2011. **20**(2): p. 229.
23. Kampinga, H.H., *Cell biological effects of hyperthermia alone or combined with radiation or drugs: a short introduction to newcomers in the field*. *Int J Hyperthermia*, 2006. **22**(3): p. 191-6.
24. Ito, A., et al., *Heat shock protein 70 expression induces antitumor immunity during intracellular hyperthermia using magnetite nanoparticles*. *Cancer Immunol Immunother*, 2003. **52**(2): p. 80-8.
25. Coss, R.A. and W.A. Linnemans, *The effects of hyperthermia on the cytoskeleton: a review*. *Int J Hyperthermia*, 1996. **12**(2): p. 173-96.
26. Garcia, M.P., J.R. Cavalheiro, and M.H. Fernandes, *Acute and long-term effects of hyperthermia in B16-F10 melanoma cells*. *PLoS One*, 2012. **7**(4): p. e35489.
27. Hildebrandt, B., et al., *The cellular and molecular basis of hyperthermia*. *Crit Rev Oncol Hematol*, 2002. **43**(1): p. 33-56.
28. Huang, S.H., et al., *Effects of hyperthermia on the cytoskeleton and focal adhesion proteins in a human thyroid carcinoma cell line*. *J Cell Biochem*, 1999. **75**(2): p. 327-37.
29. Majda, J.A., et al., *Heat shock-induced shedding of cell surface integrins in A549 human lung tumor cells in culture*. *Exp Cell Res*, 1994. **210**(1): p. 46-51.
30. Cremer, J. and J. Bligh, *Body-temperature and responses to drugs*. *British Medical Bulletin*, 1969. **25**(3): p. 299-306.
31. Liu, D.J.a.J., *Current devices for high-performance whole-body hyperthermia therapy*. *Expert Rev. Med. Devices*, 2010. **7**(3): p. 407-423.
32. van der Zee, J., *Heating the patient: a promising approach?* *Ann Oncol*, 2002. **13**(8): p. 1173-84.
33. Coleman, A., et al., *Optimizing regional infusion treatment strategies for melanoma of the extremities*. *Expert Rev Anticancer Ther*, 2009. **9**(11): p. 1599-609.

34. Meyer, J., *Hyperthermia as an anticancer modality--a historical perspective*. Frontiers of radiation therapy and oncology, 1984. **18**: p. 1.
35. Xiang, S.-H. and J. Liu, *Comprehensive evaluation on the heating capacities of four typical whole body hyperthermia strategies via compartmental model*. International Journal of Heat and Mass Transfer, 2008. **51**(23): p. 5486-5496.
36. Hahn, G.M., *Potential for therapy of drugs and hyperthermia*. Cancer Research, 1979. **39**(6 Part 2): p. 2264-2268.
37. Arciero, C.A. and E.R. Sigurdson, *Diagnosis and treatment of metastatic disease to the liver*. Semin Oncol, 2008. **35**(2): p. 147-59.
38. Curley, S.A., *Radiofrequency ablation of malignant liver tumors*. Ann Surg Oncol, 2003. **10**(4): p. 338-47.
39. Hildebrandt, B. and P. Wust, *The biologic rationale of hyperthermia*. Cancer Treat Res, 2007. **134**: p. 171-84.
40. Wust, P., et al., *Hyperthermia in combined treatment of cancer*. Lancet Oncol, 2002. **3**(8): p. 487-97.
41. Rao, W., Z.S. Deng, and J. Liu, *A review of hyperthermia combined with radiotherapy/chemotherapy on malignant tumors*. Crit Rev Biomed Eng, 2010. **38**(1): p. 101-16.
42. Melancon, M.P., et al., *In vitro and in vivo targeting of hollow gold nanoshells directed at epidermal growth factor receptor for photothermal ablation therapy*. Molecular Cancer Therapeutics, 2008. **7**(6): p. 1730-9.
43. Ghosh, S.K. and T. Pal, *Interparticle coupling effect on the surface plasmon resonance of gold nanoparticles: from theory to applications*. Chem Rev, 2007. **107**(11): p. 4797-862.
44. Gobin, A.M., et al., *Near-infrared-resonant gold/gold sulfide nanoparticles as a photothermal cancer therapeutic agent*. Small, 2010. **6**(6): p. 745-52.
45. Terentyuk, G.S., et al., *Photothermal effects induced by laser heating of gold nanorods in suspensions and inoculated tumours during in vivo experiments*. Quantum Electronics, 2012. **42**(5): p. 380-389.
46. Huang, X., et al., *Plasmonic photothermal therapy (PPTT) using gold nanoparticles*. Lasers Med Sci, 2008. **23**(3): p. 217-28.
47. An, W., et al., *Radiative properties of gold nanorod solutions and its temperature distribution under laser irradiation: Experimental investigation*. Experimental Thermal and Fluid Science, 2013. **44**: p. 409-418.
48. Yanase, M., et al., *Intracellular hyperthermia for cancer using magnetite cationic liposomes: an in vivo study*. Cancer Science, 1998. **89**(4): p. 463-470.
49. Brusentsova, N.A., et al., *Magnetic fluid hyperthermia of the mouse experimental tumor*. Journal of Magnetism and Magnetic Materials, 2002. **252**(2002): p. 378-380.
50. Bulte, J.W. and D.L. Kraitchman, *Iron oxide MR contrast agents for molecular and cellular imaging*. NMR Biomed, 2004. **17**(7): p. 484-99.

51. Laurent, S., et al., *Magnetic iron oxide nanoparticles for biomedical applications*. *Future Med Chem*, 2010. **2**(3): p. 427-49.
52. Pankhurst, Q.A., et al., *Progress in applications of magnetic nanoparticles in biomedicine*. *Journal of Physics D: Applied Physics*, 2009. **42**(22): p. 224001.
53. Kumar, C.S. and F. Mohammad, *Magnetic nanomaterials for hyperthermia-based therapy and controlled drug delivery*. *Advanced Drug Delivery Reviews*, 2011. **63**(9): p. 789-808.
54. Rosensweig, R.E., *Heating magnetic fluid with alternating magnetic field*. *Journal of Magnetism and Magnetic Materials*, 2002. **252**(1-3): p. 370-374.
55. Hergt, R., S. Dutz, and M. Roder, *Effects of size distribution on hysteresis losses of magnetic nanoparticles for hyperthermia*. *J Phys Condens Matter*, 2008. **20**(38): p. 385214.
56. JILES, D.C., *Theory of Ferromagnetic Hysteresis*. *Journal of Magnetism and Magnetic Materials*, 1986. **61**: p. 48 - 60.
57. Pennes, H.H., *Analysis of tissue and arterial blood temperatures in the resting human forearm*. *Journal of Applied Physiology*, 1948. **1**(2): p. 93-122.
58. Wissler, E.H., *Pennes' 1948 paper revisited*. *J Appl Physiol* (1985), 1998. **85**(1): p. 35-41.
59. Shliomis, M.I., *Magnetic fluids*. *Soviet Physics Uspekhi*, 1974. **17**(2): p. 153.
60. Jánosfalvi, Z., J. Hakl, and P.F. de Châtel, *Larmor precession and Debye relaxation of single-domain magnetic nanoparticles*, 2013, Cornell University: arXiv:1201.5236 [cond-mat.mes-hall].
61. Néel, L., *Théorie du traînage magnétique des ferromagnétiques en grains fins avec application aux terres cuites*. *Annales de Géophysique*. Vol. 5. 1949
62. Lee, J.H., et al., *Exchange-coupled magnetic nanoparticles for efficient heat induction*. *Nature Nanotechnology*, 2011. **6**(7): p. 418-22.
63. Guardia, P., et al., *Water-soluble iron oxide nanocubes with high values of specific absorption rate for cancer cell hyperthermia treatment*. *ACS Nano*, 2012. **6**(4): p. 3080-91.
64. Pennes, H.H., *Analysis of tissue and arterial blood temperatures in the resting human forearm (Reprinted from Journal of Applied Physiology, vol 1, pg 93-122, 1948)*. *Journal of Applied Physiology*, 1998. **85**(1): p. 5-34.
65. Arkin, H., L.X. Xu, and K.R. Holmes, *Recent developments in modeling heat transfer in blood perfused tissues*. *IEEE Trans Biomed Eng*, 1994. **41**(2): p. 97-107.
66. Wilmanski, K., *Porous Media at Finite Strains. The New Model with the Balance Equation of Porosity*. *Archives of Mechanics* 1996. **48**(4): p. 591-628.
67. Bowen, R.M. and A.C. Eringen, *Theory of Mixtures, Part I. Continuum Physics III.*, in *Theory of Mixtures*, A. Press, Editor. 1976: New York, USA.

68. Schutt, D.J. and D. Haemmerich, *Effects of variation in perfusion rates and of perfusion models in computational models of radio frequency tumor ablation*. Med Phys, 2008. **35**(8): p. 3462-70.
69. Gasselhuber, A., et al., *Mathematical spatio-temporal model of drug delivery from low temperature sensitive liposomes during radiofrequency tumour ablation*. Int J Hyperthermia, 2010. **26**(5): p. 499-513.
70. J. D. Cutnell and K.W. Johnson., *Physics, 4th Edition*, ed. 1. 1997: John Wiley & Sons Canada, Ltd.
71. Blake, A.S., G.W. Petley, and C.D. Deakin, *Effects of changes in packed cell volume on the specific heat capacity of blood: implications for studies measuring heat exchange in extracorporeal circuits*. Br J Anaesth, 2000. **84**(1): p. 28-32.
72. Faber, P. and L. Garby, *Fat content affects heat capacity: a study in mice*. Acta Physiol Scand, 1995. **153**(2): p. 185-7.
73. Brown, S.L., J.W. Hunt, and R.P. Hill, *Differential thermal sensitivity of tumour and normal tissue microvascular response during hyperthermia*. Int J Hyperthermia, 1992. **8**(4): p. 501-14.
74. dos Santos, I., et al., *Effect of variable heat transfer coefficient on tissue temperature next to a large vessel during radiofrequency tumor ablation*. BioMedical Engineering OnLine, 2008. **7**(1): p. 21.
75. Suto, M., et al., *Heat dissipation mechanism of magnetite nanoparticles in magnetic fluid hyperthermia*. Journal of Magnetism and Magnetic Materials, 2009. **321**(10): p. 1493-1496.
76. Kallumadil, M., et al., *Suitability of commercial colloids for magnetic hyperthermia*. Journal of Magnetism and Magnetic Materials, 2009. **321**(10): p. 1509-1513.
77. Jean-Paul Fortin, C.W., Jacques Servais, Christine Ménager, Jean Claude Bacri, and Florence Gazeau, *Size-Sorted Anionic Iron Oxide Nanomagnets as Colloidal Mediators for Magnetic Hyperthermia*. J. AM. CHEM. SOC, 2007. **129**(9).
78. Baker, I., et al., *Heat deposition in iron oxide and iron nanoparticles for localized hyperthermia*. Journal of Applied Physics, 2006. **99**(8): p. 08H106.
79. Beković, M. and A. Hamler, *Determination of the Heating Effect of Magnetic Fluid in Alternating Magnetic Field*. IEEE TRANSACTIONS ON MAGNETICS, 2010. **46**(2): p. 4.
80. Laurent, S., et al., *Magnetic fluid hyperthermia: focus on superparamagnetic iron oxide nanoparticles*. Advances in Colloid and Interface Science, 2011. **166**(1-2): p. 8-23.
81. Chen, S., C.-I. Chiang, and S. Hsieh, *Simulating physiological conditions to evaluate nanoparticles for magnetic fluid hyperthermia (MFH) therapy applications*. Journal of Magnetism and Magnetic Materials, 2010. **322**(2): p. 247-252.
82. Li, Z., et al., *Magnetite nanoparticles with high heating efficiencies for application in the hyperthermia of cancer*. Materials Science and Engineering: C, 2010. **30**(7): p. 990-996.

83. Dennis, C.L., et al., *The influence of magnetic and physiological behaviour on the effectiveness of iron oxide nanoparticles for hyperthermia*. Journal of Physics D: Applied Physics, 2008. **41**(13): p. 134020.
84. Cherukuri, P., E.S. Glazer, and S.A. Curley, *Targeted hyperthermia using metal nanoparticles*. Adv Drug Deliv Rev, 2010. **62**(3): p. 339-45.
85. Manthe, R.L., et al., *Tumor ablation and nanotechnology*. Molecular Pharmaceutics, 2010. **7**(6): p. 1880-98.
86. Huber, D.L., *Synthesis, properties, and applications of iron nanoparticles*. Small, 2005. **1**(5): p. 482-501.
87. Kumar, C.S. and F. Mohammad, *Magnetic nanomaterials for hyperthermia-based therapy and controlled drug delivery*. Adv Drug Deliv Rev, 2011. **63**(9): p. 789-808.
88. Suzuki, M., et al., *Anticancer effect and immune induction by hyperthermia of malignant melanoma using magnetite cationic liposomes*. Melanoma Res, 2003. **13**(2): p. 129-35.
89. Elsherbini, A.A.M., et al., *Magnetic nanoparticle-induced hyperthermia treatment under magnetic resonance imaging*. Magnetic Resonance Imaging, 2011. **29**(2): p. 272-280.
90. Dennis, C.L., et al., *Nearly complete regression of tumors via collective behavior of magnetic nanoparticles in hyperthermia*. Nanotechnology, 2009. **20**(39): p. 395103.
91. Lewinski, N., V. Colvin, and R. Drezek, *Cytotoxicity of nanoparticles*. Small, 2008. **4**(1): p. 26-49.
92. Lévy, M., et al., *Degradability of superparamagnetic nanoparticles in a model of intracellular environment: follow-up of magnetic, structural and chemical properties*. Nanotechnology, 2010. **21**(39): p. 395103.
93. Purushotham, S. and R.V. Ramanujan, *Modeling the performance of magnetic nanoparticles in multimodal cancer therapy*. Journal of Applied Physics, 2010. **107**(11): p. 114701.
94. Atkinson, W.J., I.A. Brezovich, and D.P. Chakraborty, *Usable frequencies in hyperthermia with thermal seeds*. IEEE Trans Biomed Eng, 1984. **31**(1): p. 70-5.
95. Crayton, S.H., et al., *ICP-MS analysis of lanthanide-doped nanoparticles as a non-radiative, multiplex approach to quantify biodistribution and blood clearance*. Biomaterials, 2012. **33**(5): p. 1509-1519.
96. Godin, B., et al., *Discoidal Porous Silicon Particles: Fabrication and Biodistribution in Breast Cancer Bearing Mice*. Advanced Functional Materials, 2012: p. 4225–4235.
97. van de Ven, A.L., et al., *Rapid tumoritropic accumulation of systemically injected plateloid particles and their biodistribution*. J Control Release, 2012. **158**(1): p. 148-55.
98. Heidsieck, A., et al., *Analysis of Trajectories for Targeting of Magnetic Nanoparticles in Blood Vessels*. Mol Pharm, 2012.

99. Chertok, B., et al., *Iron oxide nanoparticles as a drug delivery vehicle for MRI monitored magnetic targeting of brain tumors*. *Biomaterials*, 2008. **29**(4): p. 487-496.
100. Li, Y.F. and C. Chen, *Fate and toxicity of metallic and metal-containing nanoparticles for biomedical applications*. *Small*, 2011. **7**(21): p. 2965-80.
101. Klausner, R.D., T.A. Rouault, and J.B. Harford, *Regulating the fate of mRNA: the control of cellular iron metabolism*. *Cell*, 1993. **72**(1): p. 19-28.
102. Laurent, S., et al., *Magnetic iron oxide nanoparticles: synthesis, stabilization, vectorization, physicochemical characterizations, and biological applications*. *Chem Rev*, 2008. **108**(6): p. 2064-110.
103. Gupta, A.K. and M. Gupta, *Synthesis and surface engineering of iron oxide nanoparticles for biomedical applications*. *Biomaterials*, 2005. **26**(18): p. 3995-4021.
104. Haun, J.B., et al., *Magnetic nanoparticle biosensors*. *Wiley Interdiscip Rev Nanomed Nanobiotechnol*, 2010. **2**(3): p. 291-304.
105. Pittet, M.J., et al., *Labeling of immune cells for in vivo imaging using magnetofluorescent nanoparticles*. *Nature Protocols*, 2006. **1**(1): p. 73-79.
106. Lanza, G.M., et al., *Molecular imaging and targeted drug delivery with a novel, ligand-directed paramagnetic nanoparticle technology*. *Acad Radiol*, 2002. **9 Suppl 2**: p. S330-1.
107. Jun, Y.W., J.T. Jang, and J. Cheon, *Magnetic nanoparticle assisted molecular MR imaging*. *Adv Exp Med Biol*, 2007. **620**: p. 85-106.
108. Lartigue, L., et al., *Biodegradation of iron oxide nanocubes: high-resolution in situ monitoring*. *ACS Nano*, 2013. **7**(5): p. 3939-52.
109. Lee, C.M., et al., *Nonpolymeric surface-coated iron oxide nanoparticles for in vivo molecular imaging: biodegradation, biocompatibility, and multiplatform*. *J Nucl Med*, 2013. **54**(11): p. 1974-80.
110. Kunzmann, A., et al., *Toxicology of engineered nanomaterials: focus on biocompatibility, biodistribution and biodegradation*. *Biochim Biophys Acta*, 2011. **1810**(3): p. 361-73.
111. Hao, R., et al., *Synthesis, functionalization, and biomedical applications of multifunctional magnetic nanoparticles*. *Adv Mater*, 2010. **22**(25): p. 2729-42.
112. Gupta, A.K., et al., *Recent advances on surface engineering of magnetic iron oxide nanoparticles and their biomedical applications*. *Nanomedicine*, 2007. **2**(1): p. 23-39.
113. Dames, P., et al., *Targeted delivery of magnetic aerosol droplets to the lung*. *Nature Nanotechnology*, 2007. **2**(8): p. 495-499.
114. Polyak, B., et al., *High field gradient targeting of magnetic nanoparticle-loaded endothelial cells to the surfaces of steel stents*. *Proceedings of the National Academy of Sciences*, 2008. **105**(2): p. 698-703.
115. Paquet, C., et al., *Clusters of superparamagnetic iron oxide nanoparticles encapsulated in a hydrogel: a particle architecture*

- generating a synergistic enhancement of the T2 relaxation.* ACS Nano, 2011. **5**(4): p. 3104-12.
116. Roca, A.G., et al., *Effect of nanoparticle and aggregate size on the relaxometric properties of MR contrast agents based on high quality magnetite nanoparticles.* Journal of Physical Chemistry B, 2009. **113**(19): p. 7033-9.
117. Matsumoto, Y. and A. Jasanoff, *T2 relaxation induced by clusters of superparamagnetic nanoparticles: Monte Carlo simulations.* Magn Reson Imaging, 2008. **26**(7): p. 994-8.
118. Vuong, Q.L., P. Gillis, and Y. Gossuin, *Monte Carlo simulation and theory of proton NMR transverse relaxation induced by aggregation of magnetic particles used as MRI contrast agents.* J Magn Reson, 2011. **212**(1): p. 139-48.
119. Jun, Y.W., J.W. Seo, and A. Cheon, *Nanoscaling laws of magnetic nanoparticles and their applicabilities in biomedical sciences.* Accounts of Chemical Research, 2008. **41**(2): p. 179-189.
120. Smolensky, E.D., et al., *Scaling Laws at the Nano Size: The Effect of Particle Size and Shape on the Magnetism and Relaxivity of Iron Oxide Nanoparticle Contrast Agents.* J Mater Chem B Mater Biol Med, 2013. **1**(22): p. 2818-2828.
121. Tong, S., et al., *Coating optimization of superparamagnetic iron oxide nanoparticles for high T2 relaxivity.* Nano Lett, 2010. **10**(11): p. 4607-13.
122. Lee, N., et al., *Water-dispersible ferrimagnetic iron oxide nanocubes with extremely high r(2) relaxivity for highly sensitive in vivo MRI of tumors.* Nano Lett, 2012. **12**(6): p. 3127-31.
123. Bae, K.H., et al., *Chitosan oligosaccharide-stabilized ferrimagnetic iron oxide nanocubes for magnetically modulated cancer hyperthermia.* ACS Nano, 2012. **6**(6): p. 5266-73.
124. Wang, T., et al., *Shape-controlled synthesis of colloidal superparticles from nanocubes.* J Am Chem Soc, 2012. **134**(44): p. 18225-8.
125. Buonsanti, R., et al., *Architectural Control of Seeded-Grown Magnetic-Semiconductor Iron Oxide-TiO2 Nanorod Heterostructures: The Role of Seeds in Topology Selection.* Journal of the American Chemical Society, 2010. **132**(7): p. 2437-2464.
126. Palchoudhury, S., et al., *Controlled synthesis of iron oxide nanoplates and nanoflowers.* Chem Commun (Camb), 2012. **48**(85): p. 10499-501.
127. Kim, D., et al., *Synthesis of Uniform Ferrimagnetic Magnetite Nanocubes.* Journal of the American Chemical Society, 2009. **131**(2): p. 454-+.
128. Yu, W.W., et al., *Synthesis of monodisperse iron oxide nanocrystals by thermal decomposition of iron carboxylate salts.* Chemical Communications, 2004(20): p. 2306-2307.
129. Prakash, A., et al., *Bilayers as Phase Transfer Agents for Nanocrystals Prepared in Nonpolar Solvents.* Acs Nano, 2009. **3**(8): p. 2139-2146.

130. Key, J., et al., *Engineering discoidal polymeric nanoconstructs with enhanced magneto-optical properties for tumor imaging*. *Biomaterials*, 2013. **34**(21): p. 5402-10.
131. Lee, J.Y., et al., *Prolonged gene silencing by siRNA/chitosan-g-deoxycholic acid polyplexes loaded within biodegradable polymer nanoparticles*. *J Control Release*, 2012. **162**(2): p. 407-13.
132. Aryal, S., et al., *Engineered magnetic hybrid nanoparticles with enhanced relaxivity for tumor imaging*. *Biomaterials*, 2013. **34**(31): p. 7725-32.
133. Eto, Y., et al., *Control and Detection of the Larmor Precession of $F=2$ Rb-87 Bose-Einstein Condensates by Ramsey Interferometry and Spin-Echo*. *Applied Physics Express*, 2013. **6**(5).
134. Adriani, G., et al., *The preferential targeting of the diseased microvasculature by disk-like particles*. *Biomaterials*, 2012. **33**(22): p. 5504-13.
135. Lee, N., et al., *Water-dispersible ferrimagnetic iron oxide nanocubes with extremely high $r(2)$ relaxivity for highly sensitive in vivo MRI of tumors*. *Nano Letters*, 2012. **12**(6): p. 3127-31.
136. Tanaka, K., et al., *Heat immunotherapy using magnetic nanoparticles and dendritic cells for T-lymphoma*. *Journal of Bioscience and Bioengineering*, 2005. **100**(1): p. 112-115.
137. Motoyama, J., et al., *Hyperthermic treatment of DMBA-induced rat mammary cancer using magnetic nanoparticles*. *BioMagnetic Research and Technology*, 2008. **6**(1): p. 2.
138. Riedinger, A., et al., *Subnanometer Local Temperature Probing and Remotely Controlled Drug Release Based on Azo-Functionalized Iron Oxide Nanoparticles*. *Nano letters*, 2013.